Technische Universität München
Fakultät für Physik
Max-Planck-Institut für Plasmaphysik (IPP)

Linear Gyrokinetic Description of Fast Particle Effects on the MHD Stability in Tokamaks

Philipp Lauber

Vollständiger Abdruck der von der Fakultät für Physik
der Technischen Universität München
zur Erlangung des akademischen Grades eines
Doktors der Naturwissenschaften (Dr.rer.nat.)
genehmigten Dissertation.

Vorsitzender: Univ.-Prof. Dr. R. Gross

Prüfer der Dissertation: 1. Hon.-Prof. Dr. R. Wilhelm

2. Univ.-Prof. Dr. M. Lindner

Die Dissertation wurde am 3.9.2003 bei der
Technischen Universität München eingereicht und
durch die Fakultät für Physik am 17.11.2003 angenommen.

Contents

1 Abstract

In a plasma with a population of superthermal particles generated by heating or fusion processes, kinetic effects can lead to the additional destabilisation of MHD modes or even to additional (energetic particle) modes. In order to describe these modes, a new linear gyrokinetic MHD code has been developed and tested, LIGKA (Linear Gyrokinetic Shear Alfven Physics), based on the theoretical gyrokinetic MHD model [1]. This framework provides a set of linear equations derived from the general nonlinear gyrokinetic Lagrangian: the quasi neutrality equation, the gyrokinetic moment equation and the equation for the perturbed distribution function itself. A finite Larmor radius expansion together with the construction of some fluid moments and specification to the shear Alfvén regime results in a self-consistent, electromagnetic, non-perturbative model, that allows not only for growing or damped eigenvalues but also for a change in mode-structure of the magnetic perturbation due to the energetic particles.
Compared to previous implementations [1], this model is coded in a more general and comprehensive way. LIGKA uses a fourier decomposition in the poloidal coordinate and a finite element discretisation in the radial direction. Both analytical and numerical equilibria can be treated. Integration over the unperturbed particle orbits is performed with the drift-kinetic HAGIS code [40] which accurately describes the particles' trajectories. Furthermore, finite-banana-width effects are implemented in a rigorous way since the linear formulation of the model allows the exchange of the unperturbed orbit integration and the discretisation of the perturbed potentials in the radial direction. The resulting model is formulated as an eigenvalue problem and solved iteratively.
The code has been successfully benchmarked with other ideal MHD codes for the (1,1) internal kink mode and for TAE gap modes. For these modes kinetic modifications have also been investigated and benchmarks with KIN2DEM [1] have been carried out.

2 Introduction

The closer magnetic fusion experiments approach ignition the more interest and concern is attracted by super-thermal particles and their effect on stability and transport. In an ignited plasma the primary source of energetic particles will the product of nuclear fusion: If the temperature of a plasma - containing deuterium D and tritium T ions - becomes high enough (the optimum for an ignited plasma is $\sim 15keV$), the probability for the fusion reaction

$$ {}^3_1T + {}^2_1D \quad \rightarrow \quad ({}^4_2He + 3.5MeV) + (n + 14.1MeV) $$

increases sufficiently to generate a substantial number of energetic α-particles that keep the plasma in a burning state. To be able to reach this state, not only the temperatures must be high enough but also the energy confinement time τ_E (ratio of the total plasma energy to the heat loss rate) must satisfy the Lawson criterion [36]:

$$ n_F \tau_E > 1.5 \cdot 10^{20} m^{-3} s \tag{1} $$

Here n_F is the $D-T$ fuel density.
The total energy of $17.6MeV$ originating from the mass deficit is distributed as kinetic energy between the fusion products He and n according to their mass ratio 1/4. The neutrons do not interact with the plasma. The α-particles transfer their energy to the plasma through collisions or wave-particle interaction processes.
In order to reach such high temperatures beyond the ohmic heating limit, all devices today employ additional heating - e.g. neutral beam injection (NBI), ion and electron cyclotron resonance heating (ICRH, ECRH) etc. Consequently, this basic need of fusion research pushes technical improvements of the heating capabilites and entails an increasing population of energetic particles.
Since the pressure of fast particles in an ignited plasma will be $\sim 30\%$ of the background pressure (which can already be achieved by heating in today's experiments), substantial changes in the overall plasma behaviour are expected.
These changes can be mainly attributed to three different physical properties of fast ions:

- Firstly, the gyroradius for an energetic particle is larger than that of a thermal particle. Its absolute value for a particle of species i with mass m_i and charge $Z_i e$ in a magnetic field B is given by

  $$ |\varrho_i| = \frac{|v_{\perp i}|}{\omega_i} \qquad \text{with} \qquad \omega_i = \frac{Z_i e B}{m_i} \tag{2} $$

  For an upper limit, one assumes that all the kinetic energy is contained in the motion perpendicular to a magnetic field: an estimation (see figure 1) with a magnetic field

that is likely to fit the planned ITER experiment ($B = 5T$) shows that the difference of the gyroradii between a thermal D and fusion born α particles is almost one order of magnitude. However, a gyroradius of a few centimetres is still small compared to background plasma quantities with length scales of the minor plasma radius (for ITER 2m), but it can become equal to the length scales of MHD modes, which will be described below in more detail.

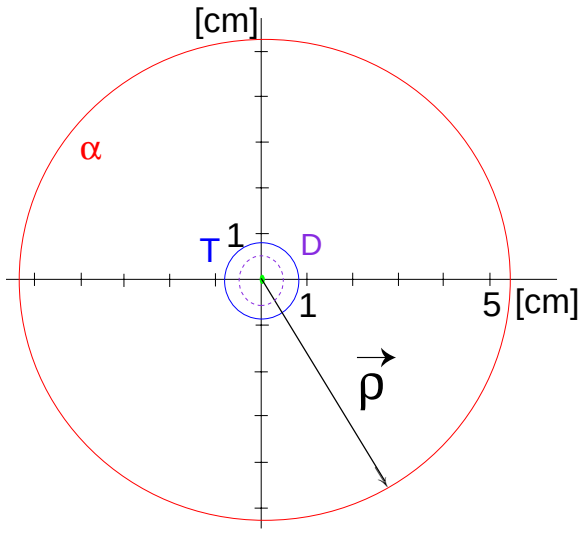

Figure 1: Gyroradii (B=5T) for electrons (0.1mm), deuterium (0.6cm), tritium (0.8cm) and helium (5.3cm) ions

- Secondly, compared to the simple slab or cylindrical case, tokamak geometry breaks the rotational symmetry of the poloidal coordinate and thus adds more intrinsic frequencies to the system, where an effective transfer of energy between plasma waves and particles can occur.
  Since this type of periodic motion is closely bound to the plasma's geometry, the tokamak concept is shortly introduced, which is the configuration that underlies all calculations in this work.
  As shown in figure 2, a tokamak consists of magnetic field coils wound around the torus poloidally to generate a toroidal field whose radial variation goes like $1/R$ (R stands for the major radius of the tokamak). A transformer coil in the centre of the torus induces a current within the plasma, that produces a poloidal magnetic field. It's spatial dependence is therefore determined by the current profile. Together, these two magnetic field components bend the field lines into a helical shape, that

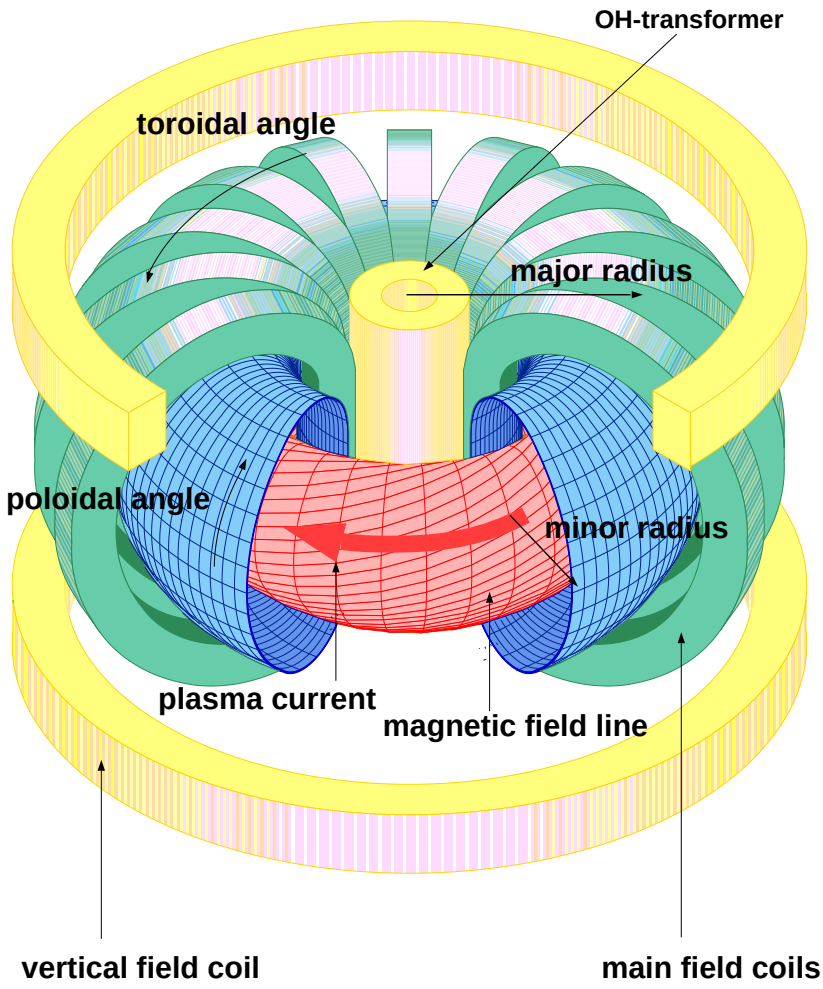

Figure 2: The Tokamak configuration

suppresses instabilities connected with a pure poloidal or pure toroidal field.

From these geometrical facts together with a current profile that balances the pressure gradient via the Lorentz force, an equilibrium magnetic field can be calculated. A typical spatial profile is shown in figure 3.
The periodicity in the poloidal angle immediately explains the 'new' frequencies mentioned above: in addition to the total kinetic energy of a particle, also the magnetic moment $\mu = mv_\perp^2/2B$ is an adiabatic invariant of the motion. Therefore it is required that $v_\parallel$ has to be smaller in regions where B becomes larger according to

$$const = E = \frac{1}{2}mv_\parallel^2 + \mu B. \tag{3}$$

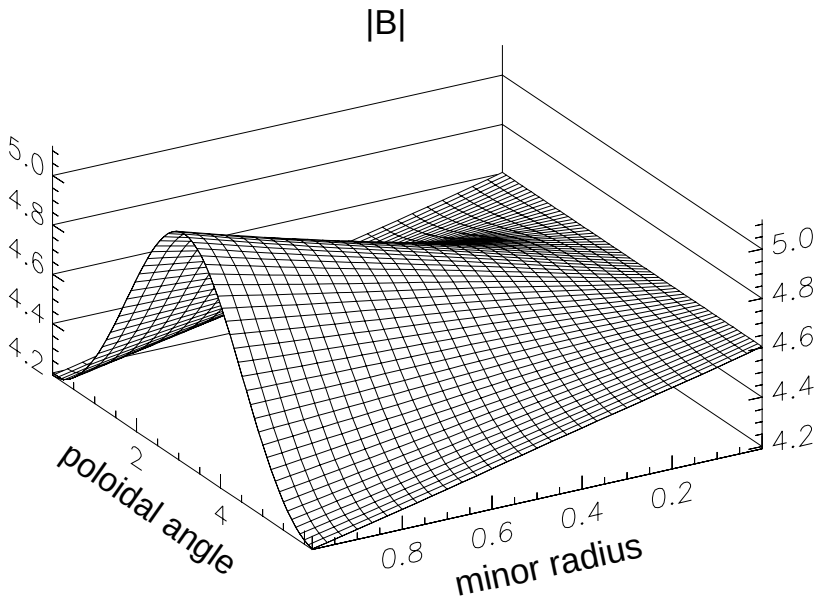

Figure 3: typical spatial dependence of the absolute value of the magnetic field in a tokamak

Consequently, there will be mainly two types of motions: a particle, whose parallel energy is high enough to keep its magnetic moment constant while travelling over the top of the magnetic hill, is called a 'passing' or 'transit' particle. In contrast, a particle with a too low parallel energy compared to its μ cannot cross the magnetic hill and is therefore trapped in the low B-field region.
Detailed calculation shows, that for thermal ions the bounce/passing frequencies are often too small to interact effectively with modes on the MHD time scale: for a typical set of ITER parameters ($B = 5$T, $R = 4$m), $\omega_A \equiv \sqrt{B^2/\mu_0 mn}/R_0 \approx 4 \cdot 10^6 s^{-1}$, wheras the transit resp. bounce frequency for thermal ions (15 keV) is about $4 \cdot 10^5 s^{-1}$ resp. $1.0 \cdot 10^5 s^{-1}$.
Of course, this situation changes when highly energetic particles are present, whose transit/bounce frequency in this example lies around $6 \cdot 10^6 s^{-1}$ resp. $1.5 \cdot 10^6 s^{-1}$ (for 660 keV α-particles).

Furthermore, the particles' orbits in a tokamak are also governed by ∇B and curvature drifts, that cause the particle to leave its field line both in the poloidal and the radial direction. Some typical drift orbits of passing and trapped energetic α particles are shown in figure 4. From this plot the conclusion can be drawn, that for energetic ions the radial excursions can become very large, dependent again on

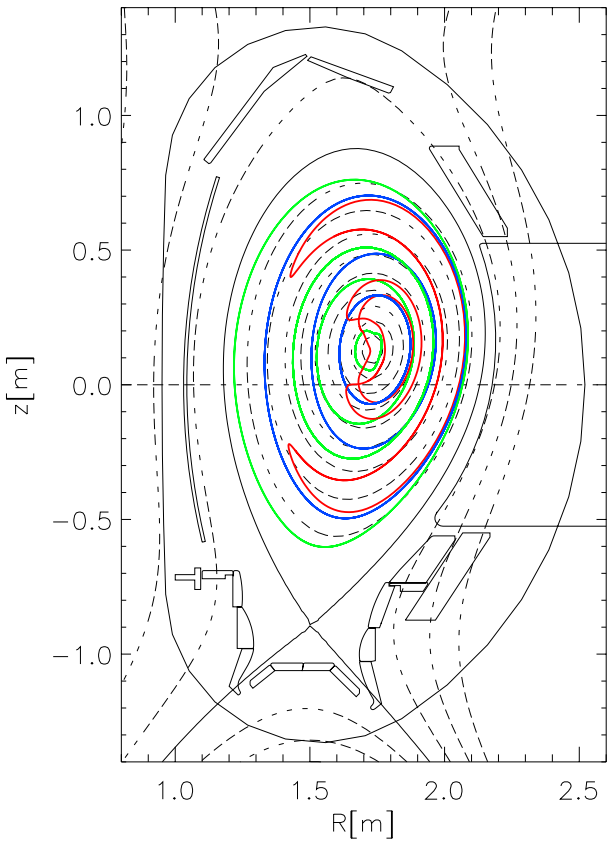

Figure 4: Poloidal projections of trapped (red), co-passing (blue) and counter-passing (green) $3.5MeV$ α-particles in realistic geometry, calculated with HAGIS [40] (more details in chapter 5.4)

the particle's energy. Therefore, the banana width turns out to be comparable to the spatial dimensions of large-scale MHD modes.

- As final point in this overview, differences in the velocity distribution functions are discussed. If the plasma is considered to rest in an thermal equilibrium state, the distribution function of the thermal particles in velocity space is assumed to be Maxwellian (for magnetically confined plasmas this can be true only an approximate and one-dimensional sense, see [59]). For any kind of fast particle population this is not true any more. Dependent on the source, there can be various forms of energy and pitch angle $\lambda = v_\parallel / v$ dependencies: for fusion born α-particles, usually a so called 'slowing down' function in the energy is applied, whose functional dependence is derived from the Fokker-Planck equation, accounting for the drag of the background ions due to collisions [39]. The pitch angle is assumed to be isotropic.

For fast ions produced by external heating there is no λ-isotropy. Each scheme possesses its own characteristics in λ and thus causes different physical interaction with MHD modes and background quantities.

After this survey over the physical properties of energetic particles, the features of MHD modes interacting with these particles are characterised.

The most dangerous modes for fusion devices are large scale MHD instabilities. Due to their global structure the equilibrium can be dramatically perturbed with disruptions as a possible consequence. These modes usually have frequencies in the range of the plasma's Alfvén frequency (for typical parameters $\sim 10^6/s$) i.e. well below the ion cyclotron frequency ($\sim 10^8/s$).
A large scale structure means that these perturbations have low m (poloidal) and low n (toroidal) mode numbers . Therefore they cannot be described locally or in the ballooning (i.e. high-n) approximation [29]. (Numerical codes based on this high-n treatment are the HINST [57] and the FULL [58] code.)
In this work, two MHD phenomena and their kinetic modifications are investigated:

- The internal kink mode is partially pressure, partially current driven. It consists of a shift of the central plasma part - within the $q = 1$ surface - against the surrounding plasma. A look at the MHD eigenfunction shows (figure 5), that this mode exhibits a 'multi-scale-structure', i.e. an overall global structure, but also a very localised behaviour at the resonant surface.
  Experimentally it has been found [67], that the injection of energetic beams can trigger periodic bursts, called 'fishbones', that are caused by resonances between the (m=1,n=1) kink and the fast ions [68]. As a consequence, the fast ions are effectively redistributed and thus lead to energy loss and decreasing confinement.

- When the properties of an ignited plasma are predicted, TAE modes (Toroidal Alfvén Eigenmodes) attract increasing interest: TAEs can be excited in 'gaps' that are caused by the break up of the continuous Alfvén spectrum due to toroidal coupling. In such a gap, there is no continuum damping present. This allows the existence of global modes that are driven to large amplitudes by passing or trapped energetic ions [53],[54] with dangerous consequences to confinement and stability.

In order to describe these phenomena theoretically and numerically, different plasma models and their range of validity have to be investigated.

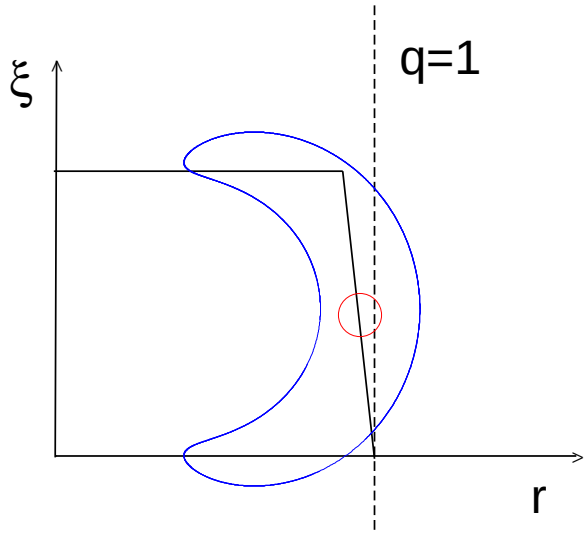

Figure 5: Eigenfunction of an internal kink mode; an α-particle's gyroradius and its banana width are comparable to the kink's scale length at the $q = 1$ surface

2.1 Challenge for Theoretical Models

As shown in figure 6, there are three theoretical frameworks that can be applied to the problem posed above.

For large scale plasma stability problems the MHD (magnetohydrodynamics) model is usually preferred [34]. It's governing equations are derived from Vlasov's equation by building moments over the velocity space resulting in a fluid formulation. The advantage of that procedure is obvious: the $6 + 1$-dimensional distribution function $f(\mathbf{x}, \mathbf{v}, t)$ is reduced to a lower dimensional variable which leads to a simplified problem. The resulting equations are hierarchical, i.e. the equation for a moment of order n depends on the moment of order $n + 1$. Thus a closure or truncation has to be found. Depending on the physics of the problem, different closures can be employed. For single fluid MHD, very high frequency ($\omega \ll \omega_{gyro}$) and short wave length ($\varrho \ll k_\perp$) phenomena are eliminated which is well satisfied when the macroscopic behaviour of fusion plasmas is investigated. The other crucial assumption is that the plasma is dominated by collisions: only then a 'fluid- element'-model is justified where an isotropic pressure - established by many randomising collisions - can be defined. However, this postulate is never fulfilled in fusion plasmas, since there is a strong anisotropy between the motion perpendicular and parallel to the magnetic field: although the Lorentz force 'squeezes' the particles together in the

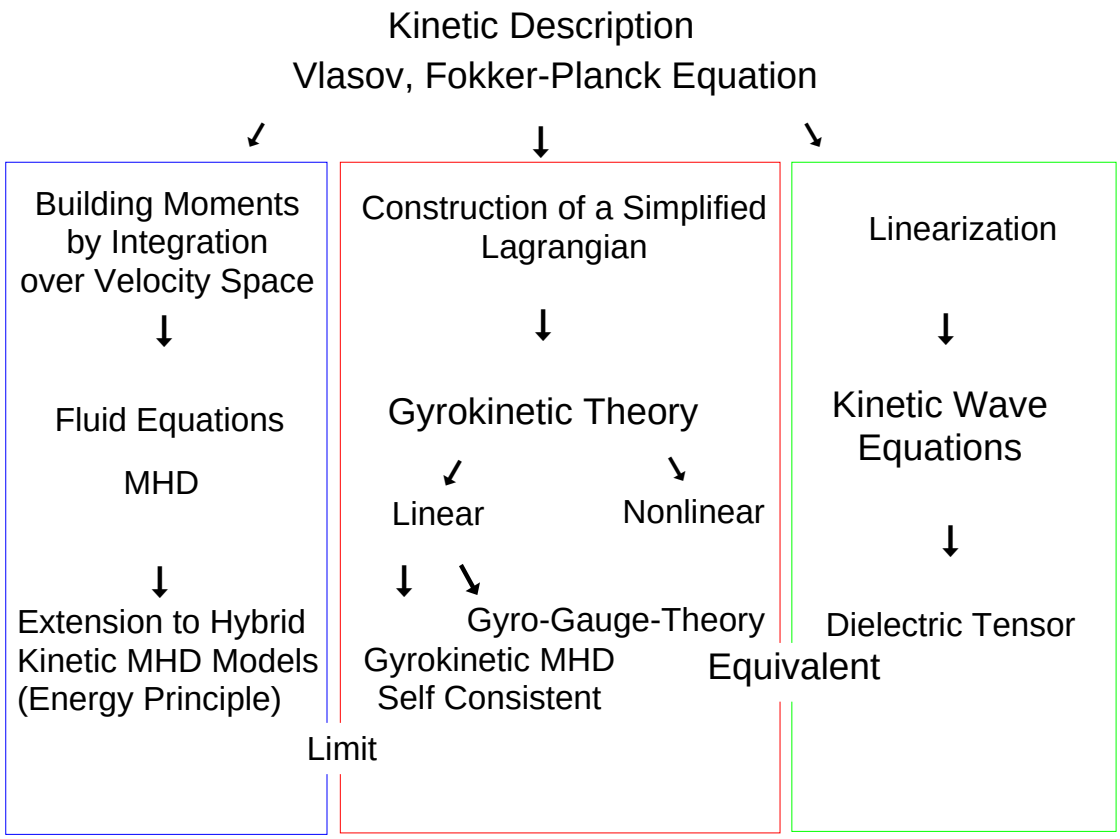

Figure 6: Survey over the three branches of kinetic plasma description

perpendicular direction which allows frequent collisions and therefore the concept of fluid elements, the particles are free streaming along the field lines since ideal MHD does not describe parallel correlations caused by kinetic resonances. Consequently, ideal MHD can only be used, when perpendicular dynamics is investigated. However, it can be shown [34], that for incompressible, parallel modes with no pressure or density fluctuations, ideal MHD can be a valid model, even in the collisionless regime.

To include kinetic effects due to hot particles, hybrid models were used extensively: the gradient ∇P term is replaced by $\nabla(P + P_{hot})$ derived from the kinetic equations. This leads to an extension of the energy principle. The new system is then generally solved in a non-self-consistent way, i.e. only the eigenvalue and not the eigenfunction is allowed to change. This perturbative treatment is only valid for small fast particle pressures.

The most important numerical codes based on this model are CASTOR-K [56] and NOVA-K [55], the extensions of the resistive MHD spectral stability codes CASTOR [48] resp. NOVA.

Although the basic problem of fast particle instabilities can be treated in a linear way, it is of substantial interest how the particles are redistributed by non-linear wave interaction. In order to investigate this problem, the drift-kinetic HAGIS code [40] has been developed. It uses an externally calculated MHD perturbation (supplied e.g. by CASTOR) but allows the fast particle distribution function to change in time. However, although phase and amplitude are allowed to evolve in time, the spatial structure of the mode is fixed.

In order to obtain more consistent equations one has to go back to the kinetic equations: to keep all kinetic effects, one would have to solve the complete Maxwell-Vlasov system - something that in toroidal symmetry is still not practicable because of the complexity of the problem. There are two possible ways of simplifying this system: the kinetic wave equations and the framework of gyrokinetic theory which was chosen in this work.
The kinetic wave equations are derived from the linearised version of Vlasov's equation and therefore describe the linear stability of waves with harmonic time dependence. This ansatz allows formal integration over time and velocity space and leads together with Maxwell's equations to a 'constitutive relation' (or a dielectric tensor) that describes the relation between current and electromagnetic fields. Historically, this method was (and still is) applied very successfully to high frequency (i.e. cyclotron frequency) phenomena, but in the last years it has also been extended to low frequency regions, including the shear Alfvén wave regime [23],[61],[25]. On the numerical side, there is the code PENN [66] which is based on the dielectric tensor derived in [61]. A low frequency version of the wave code TORIC [24] is in the development phase. Although these implementations can deal inter alia with kinetic shear and drift Alfvén wave phenomena, it is not clear that e.g. the internal kink mode can be investigated.

Modern gyrokinetic theory has been developed in the last 20 years starting with the works of Litteljohn and Cary [8]-[11]. It is based on a Lagrangian or Hamiltonian formulation. This is especially desirable when energy conservation considerations for nonlinear problems are investigated. Using near-identity Lie-transformations the gyromotion is decoupled in a formal and rigorous way from the rest of the dynamics. This mathematical treatment ensures that ordering and conservation laws are not violated.
Although gyrokinetic theory unfolds it's full power especially for non-linear problems, the linearised version also allows a systematic and elegant approach towards various stability considerations. Based on this linear gyrokinetic formulation, H. Qin has developed the framework of 'Gyrokinetic MHD' since 1999 [1]-[4] . This model consists of three equa-

tions: the quasi-neutrality equation (QN), the gyrokinetic moment equation (GKM) and the gyrokinetic equation (GKE) itself. The unknown variables are the electrostatic and electromagnetic potentials and the perturbed distribution function. In the non-kinetic, electrostatic limit, i.e. when parallel electromagnetic effects are neglected the QN equation is trivially satisfied and a finite Larmor radius expansion of the GKM equation allows one to establish contact with ideal MHD. Then also a parallel Ohm's law can be derived (what is missing in ideal MHD) and Spitzer's paradox that consists of the difference between the fluid and the guiding centre description of currents in inhomogeneous plasmas can be resolved.
Furthermore, when high-frequency terms are not neglected but only decoupled, the hot dielectric tensor as derived in the kinetic wave theory can be exactly recovered ('Gyro-Gauge-Theory' [4]).
The range of validity and the limits of the Gyrokinetic MHD model can be understood when its derivation is overviewed:

- As a first step the Vlasov's equation is transformed into the drift-kinetic equation applying a coordinate transform with the smallness parameter

$$\epsilon_B = \varrho / L_B \ll 1 \tag{4}$$

  (where ϱ is the gyroradius and $L_B = |\nabla B|/|B|$), that allows the existence of non-canonical phase space coordinates, called guiding centre coordinates.

- The next assumption is that the electromagnetic potentials can be split up in an equilibrium and a perturbation part:

$$\phi = \phi_0 + \Delta\phi_1. \tag{5}$$

  Δ represents the ratio of the amplitudes. If it is small, it can be employed as an expansion parameter for another near-identity- coordinate transformation: it removes the perturbation from the symplectic part of the Lagrangian. The resulting coordinates are called gyrocentre coordinates.

- When high frequency phenomena are are not needed

$$\omega \ll \omega_{gyro} \tag{6}$$

  (which was the original idea of gyrokinetic theory), then the terms containing the gyromotion - that were decoupled from the rest of the dynamics by the transformations above - are dropped. Gyro-Gauge theory keeps these terms.

- When one goes to the linear system, the parameter ϵ_B in combination with equilibrium quantites is ignored. Thus background finite Larmor radius effects (FLR) such as the variation of the gyroradius over the minor radius, are neglected.

- In contrast, FLR effects originating from the perturbed fields represented by $k_\perp \varrho$ are kept. Here $k_\perp$ is the perpendicular wave vector of the perturbation. For large scale MHD phenomena, $k_\perp \varrho$ is mostly well below 1 and can be used as an expansion parameter. In this work it is kept at least up to second order. To stay consistent, the condition $k_\perp \varrho < 1$ has to be verified a posteriori. (The difficulties connected with an higher order FLR-expansion is discussed in [21].) This expansion allows one to write parts of the equations in differential form, which makes contact to ideal MHD possible.

- In the gyrokinetic ordering, $\mathbf{E} \times \mathbf{B}$ flows are assumed to be of order ϵ_B. Thus gyrokinetics is not applicable to situations where large shear flows are present. So far, an extension for that case has only been derived in the ballooning limit [64],[65],[16],[6].

H. Qin also provided a numerical implementation of gyrokinetic MHD, called KIN2DEM. It is based on a trapped ion eigenvalue code developed by R. Marchand and G. Rewoldt [43],[44], that is extended for the kinetic MHD regime. It is bound to an analytical representation of the equilibrium (concentric circular tokamaks) and neglects the Shafranov shift. Analytical formulae for the particle orbit integrations and a Taylor expansion for the banana orbit width are employed.
Although this code is a valuable first step, a more comprehensive implementation is of great interest: non-circular and even non-up-down-symmetric equilibria with shifted flux surfaces not only change the properties of MHD modes, but also the particles' orbits. Furthermore, for large orbit widths the Taylor expansion becomes unreliable. Also non-Maxwellian distribution functions can cause considerable modifications [45]. In order to predict growth rates and eigenmodes sufficiently accurate these issues have to be taken into account. This has been done resulting in a new code called LIGKA (Linear Gyrokinetic Shear Alfvén Physics), which was developed as the principle part of this work.

2.2 Dissertation Outline

At the beginning, the main steps deriving the gyrokinetic system are given, following reference [5]. Starting with a Maxwell-Vlasov-Lagrangian formulation, the system is transformed in two steps to gyrocentre coordinates. In this coordinate system, the gyromotion

is decoupled from the rest of the dynamics, even when a perturbation of the field is present.
Then the linearisation of the equations is performed, resulting in the same equations as derived by Qin [1].
As the next step, the system is restricted to the shear Alfvén regime, neglecting the compressional Alfvén branch.
In chapter 4 toroidal geometry is assumed to perform further simplifications and expansions that lead to a form that is suited for numerical implementation. In addition to Qin's work, the gyro terms are also kept within the GKM kinetic integrals and also the case of a non-Maxwellian distribution function for the α-particle case is treated.
Another new issue is the description of trapped particle orbits in section 4.4.2: based on the fact that in a linear model the order of the discretisation in radial direction and the orbit integration can be exchanged, a more accurate version of the propagator integrals is derived.
Chapter 5 describes the new numerical implementation LIGKA that was developed based on the improved model described above. In contrast to KIN2DEM, it can deal with numerical equilibria and it uses the HAGIS code to describe the particles' trajectories accurately. Numerical details and basic convergence tests are given.
In the results section, various MHD-mode-calculations are carried out and benchmarked with analytical formulae and other MHD codes. The orbit integration results are compared with the analytical approximations to examine their range of validity. Finally, kinetic effects on the TAE modes and on the internal kink are examined. In the last chapter a summary is given together with an outlook to the numerous application possibilities of LIGKA.

3 Theoretical Model: Gyrokinetic Theory

Gyrokinetic description of plasma processes is broadly known and well established today. There are a number of different methods of deriving the gyrokinetic system of equations ([28],[14],[15],[17],[5]). The most complete and elegant methods were published by Bizard [17] and Sugama [5]. Here we follow mainly the latter reference, but also include important steps not mentioned there and add some physical interpretation.

3.1 Gyrokinetic Field Theory

3.1.1 The Classical Field Theory for Charged Particles in an Electromagnetic Field

To profit from its conservation properties, the variational principle is empolyed:

$$\delta I \equiv \delta \int_{t_1}^{t_2} L dt = 0, \tag{7}$$

with I the action integral, δ the variation and L the Lagrangian, that is for the Vlasov-Poisson- Ampère-system :

$$\begin{aligned} \mathit{L} \equiv \sum_a \int d^3\mathbf{x}_0 \int d^3\mathbf{v}_0 f_a(\mathbf{x}_0, \mathbf{v}_0, t_0) \\ L_a[\mathbf{x}_a(\mathbf{x}_0, \mathbf{v}_0, t_0; t), \mathbf{v}_a(\mathbf{x}_0, \mathbf{v}_0, t_0; t), \dot{\mathbf{x}}_a(\mathbf{x}_0, \mathbf{v}_0, t_0; t)] + L_f \end{aligned} \tag{8}$$

L_a is the single particle Lagrangian for species a. In an electromagnetic field, using the canonical variables $\mathbf{x}_a = \mathbf{q}$ and $m_a\mathbf{v}_a = \mathbf{p} - \frac{e_a}{c}\mathbf{A}(\mathbf{q}, t)$ [7] L_a is defined as:

$$L_a(\mathbf{x}_a, \mathbf{v}_a, \dot{\mathbf{x}}_a) \equiv \left(m_a\mathbf{v}_a + \frac{e_a}{c}\mathbf{A}(\mathbf{x}_a, t)\right) \cdot \dot{\mathbf{x}}_a - \left(\frac{1}{2}m_a|\mathbf{v}_a|^2 + e_a\phi(\mathbf{x}_a, t)\right) \equiv \mathbf{p}_a \cdot \dot{\mathbf{x}}_a - H_a \tag{9}$$

In this relation both $\mathbf{v}_a$ and $\dot{\mathbf{x}}_a$ appear, although when deriving the equations of motion we will obtain $\dot{\mathbf{x}}_a = \mathbf{v}_a$. This distinction is made because the variational principle selects that trajectory that makes the the action integral stationary. Although $\dot{\mathbf{x}}_a = \mathbf{v}_a$ is true for the physical motion, it is not true for all possible trajectories in phase space.[8].
$f_a(\mathbf{x}_0, \mathbf{v}_0, t_0)$ is the distribution function at time point t_0; $\mathbf{x}_a(\mathbf{x}_0, \mathbf{v}_0, t_0; t)$ and
$\mathbf{v}_a(\mathbf{x}_0, \mathbf{v}_0, t_0; t)$ are position and velocity of the particle at time t with the initial conditions:

$$\mathbf{x}_a(\mathbf{x}_0, \mathbf{v}_0, t_0; t_0) = \mathbf{x}_0; \qquad \mathbf{v}_a(\mathbf{x}_0, \mathbf{v}_0, t_0; t_0) = \mathbf{v}_0$$

The field part of the Lagrangian consists of an integral over the electric field tensor plus a term that establishes the Coulomb gauge $\nabla \cdot \mathbf{A} = 0$:

$$L_f \equiv \int_V d^3\mathbf{x}\mathcal{L}_f \equiv \frac{1}{8\pi}\int_V d^3\mathbf{x}\Big(|\nabla\phi(\mathbf{x}, t)|^2 - |\nabla \times \mathbf{A}(\mathbf{x}, t)|^2 + \frac{2}{c}\lambda(\mathbf{x}, t)\nabla \cdot \mathbf{A}(\mathbf{x}, t)\Big) \tag{10}$$

λ is a Lagrange undetermined multiplier. Light waves are excluded with this choice, since the $\partial\mathbf{A}/\partial t$ term is left out.
The reason for including not only the single particle contribution but also the field part in the Lagrangian is that energy conservation for the total system can be proven in an easy and obvious way.
Carrying out the variation according to the extended rule of [5], written in the most compact form, gives:

$$\delta I = 0 = \sum_\alpha \int_{t_1}^{t_2} dt \int d^{l_\alpha}\mathbf{y}_\alpha \Big[\frac{\partial \mathcal{L}_\alpha}{\partial \eta_\alpha} - \frac{d}{dt}\Big(\frac{\partial \mathcal{L}_\alpha}{\partial \dot{\eta}_\alpha}\Big) - \nabla_\alpha\Big(\frac{\partial \mathcal{L}_\alpha}{\partial \nabla_\alpha \eta_\alpha}\Big) - \nabla_\alpha \times \Big(\frac{\partial \mathcal{L}_\alpha}{\partial \nabla_\alpha \times \eta_\alpha}\Big)\Big] \quad (11)$$

η_α are the field variables, that are functions of $(\mathbf{y}_\alpha, t)$; α specifies the fields and y_α is a l_α-dimensional vector variable: $l_\alpha = 0$ means, the variable only depends on t. For $\mathbf{A}(\mathbf{x}_a, t)$, $l_\alpha = 3$ and for $\mathbf{x}_a(\mathbf{x}_0, \mathbf{v}_0, t_0; t)$ it is 6.)

Variation with respect to $\mathbf{v}_a$ results in:

$$\frac{\delta I}{\delta \mathbf{v}_a} = 0 \qquad \Rightarrow \qquad m_a \mathbf{v}_a = m_a \dot{\mathbf{x}}_a$$

Variation with respect to $\mathbf{x}_a$ gives the equation of motion:

$$\begin{aligned}
\frac{\delta I}{\delta \mathbf{x}_a} &= 0 \\
&= \frac{e_a}{c}(\nabla \mathbf{A})\dot{\mathbf{x}}_a - e_a \nabla\phi - \frac{d}{dt}\Big[m\mathbf{v}_a + \frac{e_a}{c}\mathbf{A}(\mathbf{x}_a, t)\Big] \\
&= -m_a \dot{\mathbf{v}}_a + e_a(-\nabla\phi - \frac{1}{c}\frac{\partial \mathbf{A}}{\partial t}) + \frac{e_a}{c}\Big[(\nabla \mathbf{A})\dot{\mathbf{x}} - \dot{\mathbf{x}}(\nabla \mathbf{A})\Big] \\
&= -m_a \dot{\mathbf{v}}_a + e_a\Big[\mathbf{E}(\mathbf{x}_a, t) + \frac{1}{c}\mathbf{v}_a \times \mathbf{B}(\mathbf{x}_a, t)\Big]
\end{aligned}$$

The distribution function at time point t is:

$$\begin{aligned}
f_a(\mathbf{x}, \mathbf{v}, t) = \int d^3\mathbf{x}_0 \int d^3\mathbf{v}_0 f_a(\mathbf{x}_0, \mathbf{v}_0, t_0) \\
\delta^3\Big(\mathbf{x} - \mathbf{x}_a(\mathbf{x}_0, \mathbf{v}_0, t_0; t)\Big)\delta^3\Big(\mathbf{v} - \mathbf{v}_a(\mathbf{x}_0, \mathbf{v}_0, t_0; t)\Big)
\end{aligned} \quad (12)$$

Its temporal evolution is governed by the Vlasov equation:

$$\Big[\frac{\partial}{\partial t} + \mathbf{v}\cdot\nabla + \frac{e_a}{m_a}\Big(\mathbf{E}(\mathbf{x}, t) + \frac{1}{c}\mathbf{v} \times \mathbf{B}(\mathbf{x}, t)\Big) \cdot \frac{\partial}{\partial \mathbf{v}}\Big] f_a(\mathbf{x}, \mathbf{v}, t) = 0 \quad (13)$$

How to derive the Vlasov equation starting from the equations of motion, proceeding to the Klimontovich equations, Liouville's equation and BBGKY-hierarchy, is given in

Appendix 8.1.
If one varies with respect to λ one obtains the Coulomb gauge:

$$\nabla \cdot \mathbf{A} = 0$$

Variation with respect to ϕ gives Poisson's equation:

$$\mathcal{L}_\phi = \frac{1}{8\pi}|\nabla\phi(\mathbf{x},t)|^2 - e_a \int d^3\mathbf{x}_0 \int d^3\mathbf{v}_0 f_a(\mathbf{x}_0,\mathbf{v}_0,t_0)\phi(\mathbf{x},t)\delta^3(\mathbf{x}-\mathbf{x_0}) \tag{14}$$

Consequently:

$$\begin{aligned} \frac{\delta I}{\delta\phi} &= 0 \\ &= -\frac{1}{4\pi}\nabla\cdot\nabla\phi(\mathbf{x},t) - \sum_a e_a \int d^3\mathbf{v} f_a(\mathbf{x},\mathbf{v},t) \\ \Rightarrow \quad & \nabla^2\phi(\mathbf{x},t) = -4\pi\sum_a e_a n_a \end{aligned} \tag{15}$$

Variation with respect to $\mathbf{A}$ gives Ampère's law:

$$\nabla^2\mathbf{A}(\mathbf{x},t) - \frac{\nabla}{c}\lambda(\mathbf{x},t) = -\frac{4\pi}{c}\sum_a e_a \int f_a(\mathbf{x},\mathbf{v},t)\mathbf{v}d^3\mathbf{v} = -\frac{4\pi}{c}\mathbf{j} \tag{16}$$

Here $\nabla\times\nabla\times\mathbf{A} = -\nabla^2\mathbf{A}$ was used. The current can be split up in a longitudinal and a transverse component [12]:

$$\nabla^2\mathbf{A} = \frac{-4\pi}{c}\mathbf{j}_T \tag{17}$$

Combining the longitudinal part with Vlasov's and Poisson's equation gives: $\nabla\lambda = 4\pi\mathbf{j}_L = -\partial\mathbf{E}/\partial t = \nabla\partial\phi/\partial t$, which shows that λ is not needed to determine the fields. Consequently equations (13),(15) and (17) are taken as the full Vlasov-Poisson- Ampère system. Energy conservation can be proven ([5]), applying Noether's theorem to the following total energy:

$$\begin{aligned} E_{tot} &= \sum_a \int d^3\mathbf{x} \int d^3\mathbf{v} f_a(\mathbf{x},\mathbf{v},t)\frac{1}{2}m_a|v|^2 \\ + \quad & \frac{1}{8\pi}\int d^3\mathbf{x}(|\nabla\phi(\mathbf{x},t)|^2 - |\nabla\times\mathbf{A}(\mathbf{x},t)|^2) \end{aligned} \tag{18}$$

3.1.2 Transformation to Guiding-Centre-Coordinates

In the presence of a strong magnetic field, the motion of a charged particle is anisotropic: it gyrates around the field line wheras it is free to move along the field line. Since the parallel motion and the drifts caused by inhomogeneity and curvature in tokamak devices

are much slower than the gyromotion, it is plausible to separate the gyromotion from the rest of the particle dynamics. In order to do so, we apply a coordinate transform to this system of equations:

$$\mathbf{z}_a = (\mathbf{x}_a, v_{a\parallel}, \mu_{a0}, \theta_a) \quad \rightarrow \mathbf{Z}_a = (\mathbf{X}_a, U_a, \mu_a, \xi_a) \tag{19}$$

Furthermore we introduce

$$\epsilon_B = \frac{|\varrho|}{L_B} \quad \text{with} \quad L_B \equiv \frac{|\nabla B|}{B}$$

as the perturbation expansion parameter, where ϱ is the absolute value of the gyroradius. The most systematic approach for carrying out this transformation to all orders, would be the Lie transform technique ([11],[9]). A short introduction to this method is given in Appendix 8.5. In Appendix 8.6 a different, more physical approach following references ([14]) and ([20]) is summarised.
The resulting Lagrangian is given by:

$$L_a = \epsilon_B^{-1} \frac{e_a}{c} \mathbf{A}_a^*(\mathbf{X}_a, U_a, \mu_a) \cdot \dot{\mathbf{X}}_a + \epsilon_B \frac{m_a c}{e_a} \mu_a \dot{\xi}_a - H_{a0}(\mathbf{X}_a, U_a, \mu_a) \tag{20}$$

with

$$\mathbf{A}_a^*(\mathbf{X}_a, U_a, \mu_a) = \mathbf{A}_0(\mathbf{X}_a) + \epsilon_B \frac{m_a c}{e_a} U_a \mathbf{b}(\mathbf{X}_a) - \epsilon_B^2 \frac{m_a c^2}{e_a^2} \mu_a \mathbf{W}(\mathbf{X}_a), \tag{21}$$

$$H_{a0}(\mathbf{X}_a, U_a, \mu_a) = \frac{1}{2} m_a U_a^2 + \mu_a B_0(\mathbf{X}_a) \tag{22}$$

and

$$\mathbf{W}(\mathbf{X}_a) = [\nabla \mathbf{e}_1(\mathbf{X}_a)] \cdot \mathbf{e}_2(\mathbf{X}_a) + \frac{1}{2} \mathbf{b}(\mathbf{X}_a) \mathbf{b}(\mathbf{X}_a) \cdot [\nabla \times \mathbf{b}(\mathbf{X}_a)] \tag{23}$$

Here $\mathbf{b}$ is the unit vector along the magnetic field and $\mathbf{e}_1$ and $\mathbf{e}_2$ represent two unit vectors perpendicular to $\mathbf{b}$.
Clearly, all quantities have now to be evaluated at the guiding centre position:

$$\mathbf{X}_a = \mathbf{x}_a - \epsilon_B \frac{\mathbf{b} \times \mathbf{v}_{a0}}{\Omega_a} - \mathcal{O}(\epsilon_B^2); \tag{24}$$

For simplicity, the higher order coordinate transforms contributions are not given up to second order, since they are not explicitly needed for the following steps. Here only the first order terms for $\mathbf{X}$ (since it is multiplied with a quantity of order ϵ_B^{-1}) and the zeroth order terms for the other coordinates are given:

$$U_a = v_{a0\parallel} + \mathcal{O}(\epsilon_B); \qquad \mu_a = \mu_{a0} + \mathcal{O}(\epsilon_B); \qquad \xi_a = \theta_a + \mathcal{O}(\epsilon_B) \tag{25}$$

Calculating the Poisson brackets using the following formula ([10])

$$\begin{aligned}\Big\{F,G\Big\} &= \frac{e}{mc}\Big(\frac{\partial F}{\partial \xi}\frac{\partial G}{\partial \mu}-\frac{\partial G}{\partial \xi}\frac{\partial F}{\partial \mu}\Big)\\ &- \frac{c\mathbf{b}}{eB^*_\parallel}\Big[\Big(\nabla F+\mathbf{W}\frac{\partial F}{\partial \xi}\Big)\times\Big(\nabla G+\mathbf{W}\frac{\partial G}{\partial \xi}\Big)\Big]\\ &+ \frac{\mathbf{B}^*}{mB^*_\parallel}\Big[\Big(\nabla F+\mathbf{W}\frac{\partial F}{\partial \xi}\Big)\frac{\partial G}{\partial U}-\Big(\nabla G+\mathbf{W}\frac{\partial G}{\partial \xi}\Big)\frac{\partial F}{\partial U}\Big]\end{aligned}$$

shows, that indeed the Poisson brackets are now independent of the gyrophase i.e. the gyromotion is completely decoupled from the rest of the particle motion:

$$\Big\{\mathbf{X}_a,\mathbf{X}_a\Big\} = \epsilon_B\frac{c}{e_aB^*_{a\parallel}}\mathbf{b}\times\mathbf{I};\qquad \Big\{\mathbf{X}_a,U_a\Big\}=\frac{\mathbf{B}^*_a}{m_aB^*_{a\parallel}}; \tag{26}$$

$$\Big\{\mathbf{X}_a,\xi_a\Big\} = \epsilon_B\frac{c}{e_aB^*_{a\parallel}}\mathbf{b}\times\mathbf{W};\qquad \Big\{U_a,\xi_a\Big\}=-\frac{\mathbf{B}^*_a\cdot\mathbf{W}}{m_aB^*_{a\parallel}}; \tag{27}$$

$$\Big\{\xi_a,\mu_a\Big\} = \epsilon_B^{-1}\frac{e_a}{m_ac} \tag{28}$$

where $\mathbf{I}$ is unit dyadic and

$$\mathbf{B}^*_a\equiv\nabla\times\mathbf{A}^*_a\quad\text{and}\quad B^*_{a\parallel}\equiv\mathbf{B}^*_a\cdot\mathbf{b}. \tag{29}$$

It is important to emphasise, that the Lagrangian above still contains the full particle dynamics up to second order in ϵ_B, including the gyromotion. But since L_a does not contain ξ_a any more, μ_a is a constant of motion. Using the variational principle on this guiding centre Lagrangian would result in the well known drift kinetic equation.

3.1.3 Perturbation of the Lagrangian

In our model we want to keep FLR effects originating from terms $\sim k_\perp\varrho$. That means that a particle on its gyro-orbit must be able to feel the variation of the fields due to a certain mode (that is treated as a perturbation to the equilibrium system). When the system is perturbed by a small wave field, the guiding centre coordinates derived above are no good coordinates any longer in the sense that the gyromotion is no longer decoupled. In this section, we first introduce a new ordering parameter connected with the perturbation and then switch to gyrocentre coordinates.
Gyrokinetic ordering implies, that fields and potentials can be separated into an equilibrium and a perturbation part:

$$\mathbf{E}=\mathbf{E}_0(\mathbf{x})+\Delta\mathbf{E}_1(\mathbf{x},t)$$

$$\mathbf{B} = \mathbf{B}_0(\mathbf{x}) + \Delta\mathbf{B}_1(\mathbf{x}, t)$$
$$\mathbf{A} = \mathbf{A}_0(\mathbf{x}) + \Delta\mathbf{A}_1(\mathbf{x}, t)$$
$$\phi = \phi_0(\mathbf{x}) + \Delta\phi_1(\mathbf{x}, t)$$

where Δ is the ordering parameter for the amplitude ratios of perturbed and unperturbed quantities.
It is useful to define a new canonical momentum:

$$\mathbf{p}_a \equiv m_a\mathbf{v}_a + \frac{e_a}{c}(\mathbf{A}_0 + \mathbf{A}_1) \equiv m_a\mathbf{v}_{a0} + \frac{e_a}{c}\mathbf{A}_0; \;\; \Rightarrow \quad \mathbf{v}_{a0} \equiv \frac{1}{m_a}(\mathbf{p}_a - \frac{e_a}{c}\mathbf{A}_0) \tag{30}$$

To use v_{a0} as a variable of 0-th order has the advantage that only the Hamiltonian contains perturbed quantities, and not the symplectic part $\mathbf{p} \cdot \dot{\mathbf{q}}$. Furthermore $\mathbf{E}_0 = 0$ is assumed. $\mathbf{E}_1$ includes not only the fluctuation part but also the $\mathcal{O}(\epsilon_B)$ contribution of the $\mathbf{E} \times \mathbf{B}$-drifts.
Now the Lagrangian is expanded up to second order:

$$L_a = L_{a0} + L_{a1} + L_{a2} \tag{31}$$

with

$$L_{a0} = \left(m_a\mathbf{v}_{a0} + \frac{e_a}{c}\mathbf{A}_0\right) \cdot \dot{\mathbf{x}} - \frac{1}{2}m_a|\mathbf{v}_{a0}|^2 \equiv \mathbf{p}_a \cdot \dot{\mathbf{x}} - H_{a0} \tag{32}$$

$$L_{a1} = -e_a\left(\phi_1 - \frac{1}{c}\mathbf{v}_{a0} \cdot \mathbf{A}_1\right) \equiv -e_a\psi_a \equiv -H_{a1} \tag{33}$$

$$L_{a2} = -\frac{-e_a^2}{2m_ac^2}|\mathbf{A}_1|^2 \equiv -H_{a2} \tag{34}$$

3.1.4 Gyrocentre-Transformation

Since the perturbed fields destroy the Lagrangian's independence of the gyrophase, another coordinate transformation is employed. A detailed mathematical treatment is found in [9]. Since $\mathbf{v}_{a0}$ is chosen according to equation (30), L_{a0} and consequently also the Poisson brackets are already in the gyrophase independent form. Only the Hamiltonian part is perturbed (see equations 32-34). This method is called 'Gyrokinetic Hamilton Formalism' in contrast to the 'Gyrokinetic Phase Space Lagrange Formalism', where also the symplectic part is perturbed.)
Consequently, the generating functions of the transformation are chosen in a way that leaves the symplectic part undisturbed for all orders, i.e. that this part of the Lagrangian has to vanish for the higher orders.

$$\mathbf{Z}_a = (\mathbf{X}_a, U_a, \mu_a, \xi_a) \quad \rightarrow \bar{\mathbf{Z}}_a = (\bar{\mathbf{X}}_a, \bar{U}_a, \bar{\mu}_a, \bar{\xi}_a) \tag{35}$$

In 0-th order the guiding centre coordinates can be simply replaced by the new gyrocentre coordinates. For the 1-st and 2-nd order an appropriate choice of the gauge function S_1 results in an Hamiltonian that only contains gyrophase averaged expressions. Here just the final result is given. A short derivation sketching the main steps can be found in appendix 8.6.

$$\begin{aligned} L_a = & \epsilon_B^{-1} \frac{e_a}{c} \mathbf{A}_a^*(\bar{\mathbf{X}}_a, \bar{U}_a, \bar{\mu}_a) \cdot \dot{\bar{\mathbf{X}}}_a + \epsilon_B \frac{m_a c}{e_a} \bar{\mu}_a \dot{\bar{\xi}}_a \\ & - \bar{H}_{a0}(\bar{\mathbf{X}}_a, \bar{U}_a, \bar{\mu}_a) - \bar{H}_{a1}(\bar{\mathbf{X}}_a, \bar{U}_a, \bar{\mu}_a, t) - \bar{H}_{a2}(\bar{\mathbf{X}}_a, \bar{U}_a, \bar{\mu}_a, t) \end{aligned} \tag{36}$$

with

$$\bar{H}_{a1}(\bar{\mathbf{X}}_a, \bar{U}_a, \bar{\mu}_a, t) = e_a \langle \psi_a(\bar{\mathbf{Z}}, t) \rangle_{\bar{\xi}_a} \tag{37}$$

$$\begin{aligned} \bar{H}_{a2}(\bar{\mathbf{X}}_a, \bar{U}_a, \bar{\mu}_a, t) = & \frac{e_a^2}{2 m_a c^2} \langle |\mathbf{A}_1(\bar{\mathbf{X}}_a + \epsilon_B \bar{\varrho}_a, t)|^2 \rangle_{\bar{\xi}_a} \\ & - \frac{e_a}{2} \langle \{ \tilde{S}_{a1}(\bar{\mathbf{Z}}_a, t), \tilde{\psi}_a(\bar{\mathbf{Z}}_a, t), \} \rangle_{\bar{\xi}_a} \end{aligned} \tag{38}$$

$\langle ... \rangle$ indicates, that these terms are gyroaveraged. Thus the Hamiltionian is gyrophase independent. The fields have to be taken on the gyrocentre position:

$$\begin{aligned} \tilde{\phi}_1(\bar{\mathbf{X}}_a + \epsilon_B \bar{\boldsymbol{\varrho}}_a, t) &= \phi_1(\bar{\mathbf{X}}_a + \epsilon_B \bar{\boldsymbol{\varrho}}_a, t) - \langle \phi_1(\bar{\mathbf{X}}_a + \epsilon_B \bar{\boldsymbol{\varrho}}_a, t) \rangle \\ \widetilde{\bar{\mathbf{v}}_{a0} \cdot} \mathbf{A}_1(\bar{\mathbf{X}}_a + \epsilon_B \bar{\boldsymbol{\varrho}}_a, t) &= \bar{\mathbf{v}}_{a0} \cdot \mathbf{A}_1(\bar{\mathbf{X}}_a + \epsilon_B \bar{\boldsymbol{\varrho}}_a, t) - \langle \bar{\mathbf{v}}_{a0} \cdot \mathbf{A}_1(\bar{\mathbf{X}}_a + \epsilon_B \bar{\boldsymbol{\varrho}}_a, t) \rangle \\ \tilde{\psi}_a(\bar{\mathbf{Z}}_a, t) &= e_a \tilde{\phi}_1(\bar{\mathbf{X}}_a + \epsilon_B \bar{\boldsymbol{\varrho}}_a, t) - \frac{e_a}{c} \widetilde{\bar{\mathbf{v}}_{a0} \cdot} \mathbf{A}_1(\bar{\mathbf{X}}_a + \epsilon_B \bar{\boldsymbol{\varrho}}_a, t) \end{aligned}$$

with

$$\bar{\mathbf{X}}_a = \mathbf{X}_a + \Delta \{ S_1(\mathbf{X}_a), \mathbf{X}_a \} + \mathcal{O}(\Delta)^2 \tag{39}$$

$$\bar{\boldsymbol{\varrho}}_a = \bar{\boldsymbol{\varrho}}_{a0}(\bar{\mathbf{Z}}_a) = \mathbf{b}(\bar{\mathbf{X}}_a) \times \bar{\mathbf{v}}_{a0} / \Omega_a(\bar{\mathbf{X}}_a) \tag{40}$$

and an equation for the gauge function S_1 that contains the gyrophase terms:

$$\begin{aligned} & \epsilon_B^{-1} \Omega_a \frac{\partial S_1}{\partial \xi_a} + \frac{\partial S_1}{\partial t} + \\ & \quad \epsilon_B \left(\frac{\bar{U}_a}{m_a} \mathbf{b}^* \cdot \frac{\partial S_1}{\partial \bar{\mathbf{X}}_a} - [\frac{c}{e B_\parallel^*} \mathbf{b} \times \frac{\partial S_1}{\partial \bar{\mathbf{X}}_a} + \frac{\mathbf{B}^*}{m_a B_\parallel^*} \frac{\partial S_1}{\partial U_a}] \cdot \frac{\partial H_{a0}}{\partial \bar{\mathbf{X}}_a} \right) \\ & \quad = \tilde{\psi}_a(\bar{\mathbf{Z}}_a, t) \end{aligned} \tag{41}$$

3.1.5 Low Frequencies

The usual gyrokinetic ordering assumes low frequency perturbations (compared to the gyrofrequency): $\Omega_a^{-1} \partial / \partial t \sim \mathcal{O}(\epsilon_B)$. In zeroth order equation (41) becomes:

$$\Omega_a \frac{\partial S_1}{\partial \xi_a} = e_a \tilde{\phi}_1(\bar{\mathbf{X}}_a + \boldsymbol{\varrho}_{a0}, t) - \frac{e_a}{c} \widetilde{\bar{\mathbf{v}}_{a0} \cdot} \mathbf{A}_1(\bar{\mathbf{X}}_a + \boldsymbol{\varrho}_{a0}, t), \tag{42}$$

what can be integrated:

$$S_1 = \frac{e_a}{\Omega_a} \int d\bar{\xi}_a \tilde{\psi}_a(\bar{\mathbf{Z}}_a, t) \tag{43}$$

Using this expression for S_1, the coordinate transforms become:

$$\bar{\mathbf{X}}_a = \mathbf{X}_a + \mathcal{O}(\epsilon_B^2) + \mathcal{O}(\epsilon_B \Delta); \quad \rightarrow \quad \mathbf{x}_a = \bar{\mathbf{X}}_a + \epsilon_B \bar{\boldsymbol{\varrho}}_a. \tag{44}$$

In case of arbitrary high frequencies the time derivative in line (41) is not negligible any more. That means that S_1 is not any more given by an ξ-averaged $\tilde{\psi}$ at a certain time point t, but by an integral over t.
To include also S_1 in the Lagrangian one treats S_1 as an independent scalar field and uses the method of undetermined Lagrange multipliers (details in [5]) so that variation of I with respect to this new multiplier in return, results in equation (41).

3.1.6 Maxwell-Vlasov-System

The total Lagrangian is finally:

$$\begin{aligned} L \equiv & \sum_a \int d^6\bar{\mathbf{Z}}_0 J_a(\bar{\mathbf{Z}}_0) F_a(\bar{\mathbf{Z}}_0, t_0) L_a[\bar{\mathbf{Z}}_a(\mathbf{Z}_0, t_0; t), \dot{\bar{\mathbf{Z}}}_a(\bar{\mathbf{Z}}_0, t_0; t), t)] \\ & \frac{1}{8\pi} \int_V d^3\mathbf{x} \Big(|\nabla\phi(\mathbf{x}, t)|^2 - |\nabla \times [\mathbf{A}_0(\mathbf{x}) + \mathbf{A}_1(\mathbf{x}, t)]|^2 + \frac{2}{c} \lambda(\mathbf{x}, t) \nabla \cdot \mathbf{A}_1(\mathbf{x}, t) \end{aligned} \tag{45}$$

with

$$J_a(\bar{\mathbf{Z}}_0) = B^*_{a\|}(\bar{\mathbf{Z}}_0)/m_a; \qquad \bar{\mathbf{Z}}_0 = \bar{\mathbf{Z}}_a(\bar{\mathbf{Z}}_0, t_0; t) \tag{46}$$

As above the distribution function at time point t is given by

$$J_a(\mathbf{Z}) F_a(\mathbf{Z}, t) = \int d^6\mathbf{Z}_0 J_a(\mathbf{Z}_0) F_a(\mathbf{Z}_0, t_0) \cdot \delta^6 \Big(\bar{\mathbf{Z}} - \bar{\mathbf{Z}}_a(\bar{\mathbf{Z}}_0, t_0; t) \Big). \tag{47}$$

Variation of the Lagrangian gives the equations of motion in gyrocentre coordinates:

$$\frac{d\bar{\mathbf{Z}}_a}{dt} = \{\bar{\mathbf{Z}}_a, \bar{H}_a(\bar{\mathbf{Z}}_0, t)\} \tag{48}$$

or written in components (26):

$$\frac{d\bar{\mathbf{X}}_a}{dt} = \frac{1}{B^*_{a\|}} \Big[\Big(\bar{U}_a + \frac{\partial \bar{H}_{a2}}{m_a \partial \bar{U}_a} \Big) \mathbf{B}^*_a + \frac{c}{e_a} \mathbf{b} \times \Big(\bar{\mu}_a \nabla B_0 + \nabla \bar{H}_{a2} \Big) \Big] \tag{49}$$

$$\frac{d\bar{U}_a}{dt} = -\frac{\mathbf{B}^*_a}{m_a B^*_{a\|}} \cdot [\bar{\mu}_a \nabla B_0 + \nabla \bar{H}_{a2}] \tag{50}$$

$$\frac{d\bar{\mu}_a}{dt} = 0 \tag{51}$$

$$\frac{d\bar{\xi}_a}{dt} = \Omega_a + \mathbf{W} \cdot \frac{d\bar{\mathbf{X}}_a}{dt} + \frac{e_a}{m_a c} \frac{\partial \bar{H}_{a2}}{\partial \bar{\mu}_a} \tag{52}$$

Clearly, $\bar{\mathbf{X}}_a$, $\bar{U}_a$, $\bar{\mu}_a$ and J_a are independent of $\bar{\xi}_a$ and also $\bar{\xi}_0$. Now it can be concluded that without loss of generality also F_a is gyrophase independent. As a consequence the gyrokinetic equation can be written as:

$$\left[\frac{\partial}{\partial t} + \{\bar{\mathbf{Z}}, \bar{H}_a(\bar{\mathbf{Z}}, t)\} \cdot \frac{\partial}{\partial \bar{\mathbf{Z}}}\right] F_a(\bar{\mathbf{Z}}, t) = 0 \tag{53}$$

Poisson's equation is derived as

$$\begin{aligned} \Delta\nabla^2\phi_1(\mathbf{x}, t) &= -4\pi \sum_a e_a \int d^6\bar{\mathbf{Z}} J_a(\bar{\mathbf{Z}}) \\ &\cdot \quad \delta[\bar{\mathbf{X}} + \bar{\boldsymbol{\varrho}}_{a0}(\bar{\mathbf{Z}}) - \mathbf{x}] \cdot \Big(F_a(\bar{\mathbf{Z}}, t) + \Delta\{S_{a1}(\bar{\mathbf{Z}}, t), F_a(\bar{\mathbf{Z}}, t)\}\Big) \end{aligned} \tag{54}$$

and Ampère's law as

$$\Delta\nabla^2\mathbf{A}_1(\mathbf{x}, t) = -\frac{4\pi}{c}\Big((\mathbf{j})_T(\mathbf{x}, t) - \mathbf{j}_0(\mathbf{x}, t)\Big) \tag{55}$$

with

$$\mathbf{j}_0(\mathbf{x}, t) = -\frac{c}{4\pi}\nabla^2\mathbf{A}_0 \tag{56}$$

and $(\mathbf{j})_T$ as the transversal part of

$$\begin{aligned} \mathbf{j}(\mathbf{x}, t) &= \sum_a e_a \int d^6\bar{\mathbf{Z}} J_a(\bar{\mathbf{Z}}) \cdot \delta[\bar{\mathbf{X}} + \bar{\boldsymbol{\varrho}}_{a0}(\bar{\mathbf{Z}}) - \mathbf{x}] \\ &\cdot \quad \left(\Big[\mathbf{v}_{a0}(\bar{\mathbf{Z}}) - \Delta\frac{e_a}{m_a c}\mathbf{A}_1(\bar{\mathbf{X}} + \bar{\boldsymbol{\varrho}}_{a0}(\bar{\mathbf{Z}}), t)\Big] F_a(\bar{\mathbf{Z}}t) + \Delta\mathbf{v}_{a0}(\bar{\mathbf{Z}})\{S_1(\bar{\mathbf{Z}}, t), F_a(\bar{\mathbf{Z}}, t)\}\right) \end{aligned} \tag{57}$$

Again it is straightforward to calculate the total energy of the system and show energy conservation [5].

3.2 Linearised Equations

Following reference [1], we restrict these fully non linear equations to the linear case by splitting up the total distribution function into an equilibrium and a perturbed part:

$$F_a = F_{a0} + f_a. \tag{58}$$

Here, we keep terms in Δ up to first order. For all the physical problems investigated in this work, background FLR effects are not important. Consequently the small parameter ϵ_B is only taken into account in lowest order. But on the other hand physical effects, where the gyroradius and the perturbed mode size can be comparable are kept. Introducing

$$\epsilon_\Delta \equiv |k\varrho| \qquad \text{with} \qquad k = \frac{\nabla B_1}{B_1},$$

we now take into account terms up to second order in ϵ_Δ.
Equation (53) is expanded in:

$$\left[\{\bar{\mathbf{Z}}, \bar{H}_1(\bar{\mathbf{Z}}, t)\} \cdot \frac{\partial}{\partial \bar{\mathbf{Z}}}\right] F_{a0}(\bar{\mathbf{Z}}) + \left[\frac{\partial}{\partial t} + \{\bar{\mathbf{Z}}, \bar{H}_0(\bar{\mathbf{Z}})\} \cdot \frac{\partial}{\partial \bar{\mathbf{Z}}}\right] f_a(\bar{\mathbf{Z}}, t) = 0 \tag{59}$$

Leaving out the higher order terms as described above we obtain [1]:

$$\frac{\partial f}{\partial t} + (\bar{U}\mathbf{b} + \mathbf{v}_d) \cdot \nabla f - \frac{\mathbf{b}}{m} \cdot \nabla H_0 \frac{\partial f}{\partial \bar{U}} = \frac{c\mathbf{b}}{eB} \cdot (\nabla F_0 \times H_1) - \frac{\mathbf{b}}{m} \cdot (\nabla F_0 \frac{\partial H_1}{\partial \bar{U}} - \nabla H_1 \frac{\partial F_0}{\partial \bar{U}}) \tag{60}$$

with

$$\{\bar{\mathbf{Z}}, H_0\} = \bar{U}\mathbf{b} + \mathbf{v}_d \tag{61}$$

It is useful to write this equation also in a different set of coordinates:

$$\bar{\mathbf{Z}} = (\bar{\mathbf{X}}, H_0 = E, \bar{\mu}, \bar{\xi}) \tag{62}$$

Using the modified Poisson brackets given in equation (200) one derives:

$$\frac{\partial f}{\partial t} + (\bar{U}\mathbf{b} + \mathbf{v}_d) \cdot \nabla f = \frac{c\mathbf{b}}{eB} \cdot (\nabla F_0 \times \nabla H_1) + \frac{\partial F_0}{\partial E} (\bar{U}\mathbf{b} + \mathbf{v}_d) \cdot \nabla H_1 \tag{63}$$

Here a closer look to the different contributions of the drift terms is helpful [19]: the curvature drift term is contained in $\mathbf{B}^*$ (defined in equation 29) whereas the ∇B-drift obviously appears in a separate term:

$$\{\bar{\mathbf{Z}}, H_0\} = -\frac{c\mathbf{b}}{eB} \times (\bar{\mu}\nabla B) + \frac{(\mathbf{B} + \nabla \times \frac{mc}{e}\bar{U}\mathbf{b})\bar{U}}{B} = -\frac{c\mathbf{b}}{eB} \times (\bar{\mu}\nabla B) + \bar{U}\mathbf{b} + \mathbf{V}_d \tag{64}$$

$$\mathbf{V}_d \equiv \frac{cmU}{eB} \nabla \times U\mathbf{b} \tag{65}$$

Using

$$\nabla \times \mathbf{b} = -\mathbf{b} \times (\mathbf{b} \times (\nabla \times \mathbf{b})) = -\mathbf{b} \times \Big((\mathbf{b} \cdot \nabla)\mathbf{b}\Big) \tag{66}$$

which is correct in the order considered here, we obtain the usual expression for $\mathbf{v}_d$:

$$\mathbf{v}_d = -\frac{c\mathbf{b}}{eB} \times \Big(m\bar{U}^2(\mathbf{b} \cdot \nabla)\mathbf{b} + \bar{\mu}\nabla B\Big) \tag{67}$$

We emphasise that the linearised GKE together with the equation for the gauge function S_1 still contain the physics for all types of linearly describable waves with arbitrary frequencies. For example, it is shown in reference [3] how to specify the system to Bernstein and compressional Alfvén waves. Furthermore, the dielectric tensor derived in the framework of kinetic wave theory (in slab geometry) is recovered (see [3]). Of course also fluid equations and consequently MHD theory can be derived by building appropriate moments of the equations given above [1]. But much more important, it provides a clear and rigorous way how to extend MHD into a self consistent kinetic MHD model, that can be used to describe the interaction of MHD modes with kinetic effects.

3.3 Restriction to Shear Alfvén Physics in Tokamaks

Now the system of equations is restricted to shear Alfvén physics. In an homogenous plasma the solution of the dispersion relation (derived from the ideal MHD model) with $\omega^2 = k_\parallel^2 v_A^2 = k_\parallel^2 B^2/\mu_0 m n_0$ is called shear Alfvén wave. This incompressible wave propagates parallel to the magnetic field. The force balance is given between field line tension and plasma mass inertia. In terms of energies this translates into an oscillation between magnetic field energy and kinetic energy of the plasma. There are no perturbations of density, pressure, parallel magnetic field and perpendicular vector potential. Moreover, it is decoupled from the other MHD waves, namely the compressional Alfvén wave and the sound wave, independent of the plasma $\beta = 2\mu_0 P/B^2$.
For inhomogeneous plasmas this is not true any more. Nevertheless, the decoupling assumption for standard tokamak parameters is justified because the characteristic frequencies of the inhomogeneities (namely the diamagnetic drift frequency $\omega_* \sim 10^4$ and gradient drift $\omega_d \sim 10^5$) which are responsible for coupling, are too far apart from $\omega_A = v_A/R \sim 10^6$ to establish effective mode interaction. Furthermore, we are interested in relatively low-β plasmas (typically a few percent) with moderate aspect ratios ($\epsilon \equiv a/R \leq 0.3$). Therefore, the restricition

$$\mathbf{A}_1 = A_\parallel \mathbf{b} \quad \text{or} \quad \mathbf{A}_\perp = 0 \tag{68}$$

is consistent with the definition of the shear Alfvén wave in slab geometry, since it implies $B_{1\parallel} \ll B_{1\perp}$ and a small incompressibility. In case of a low β also small pressure pertubations can be assumed.
For all relevant sets of parameters in fusion research, ω_A is small compared to the gyro frequency, i.e we use equation (42) for S_1.

3.3.1 Poisson's Equation

Then Poisson's equation becomes:

$$0 \;=\; -4\pi \sum_a e_a \int d^6\bar{\mathbf{Z}} J_a(\bar{\mathbf{Z}}) \cdot \delta[\bar{\mathbf{X}} + \bar{\boldsymbol{\varrho}}_{a0}(\bar{\mathbf{Z}}) - \mathbf{x}] \cdot \Big(F_a(\bar{\mathbf{Z}}, t) + \Delta \frac{e}{B} \tilde{\psi}_a \frac{\partial F_a(\bar{\mathbf{Z}}, t)}{\partial \mu} \Big)$$

0-th order gives: $-4\pi \sum_a e_a n_{a0}(\mathbf{x}) = 0$. Dropping the indices for $\boldsymbol{\varrho}_{a0}$ and writing the untruncated Taylor expansion of all functions of the form $G(\bar{\mathbf{X}} + \bar{\boldsymbol{\varrho}}_{a0}(\bar{\mathbf{Z}}) - \mathbf{x})$ as $e^{\boldsymbol{\varrho}\cdot\nabla} G(\bar{\mathbf{X}} - \mathbf{x})$, we obtain for the first order terms:

$$\begin{aligned} n_{a1}(\mathbf{x}) \;&=\; \int d^3\bar{\mathbf{v}} e^{-\boldsymbol{\varrho}\cdot\nabla} f + \int d^3\bar{\mathbf{v}} d^3\bar{\mathbf{X}} e^{\boldsymbol{\varrho}\cdot\nabla} \delta(\bar{\mathbf{X}} - \mathbf{x}) \\ &\cdot\; \frac{e_a}{B} \Big[(e^{\boldsymbol{\varrho}\cdot\nabla} - \langle e^{\boldsymbol{\varrho}\cdot\nabla} \rangle) \phi(\bar{\mathbf{X}} - \mathbf{x}) - \frac{1}{c} (e^{\boldsymbol{\varrho}\cdot\nabla} - \langle e^{\boldsymbol{\varrho}\cdot\nabla} \rangle) \bar{U} A_\parallel(\bar{\mathbf{X}} - \mathbf{x}) \Big] \frac{\partial F_{a0}(\bar{\mathbf{Z}}, t)}{\partial \bar{\mu}} \end{aligned}$$

with $d^3\bar{\mathbf{v}} = (B/m)\, d\bar{\xi} d\bar{\mu} d\bar{U}$. We now use the relations

$$e^{\boldsymbol{\varrho}\cdot\nabla}\delta(\bar{\mathbf{X}} - \mathbf{x}) = \delta(\bar{\mathbf{X}} - \mathbf{x})e^{-\boldsymbol{\varrho}\cdot\nabla}$$
$$e^{-\boldsymbol{\varrho}\cdot\nabla}(h \cdot g) = h(e^{-\boldsymbol{\varrho}\cdot\nabla} - 1)g + ge^{-\boldsymbol{\varrho}\cdot\nabla}h$$

and carry out the integration over $\bar{\mathbf{X}}$. Employing the definition for the Bessel function of 0-th order (see figure 7):

$$\frac{1}{2\pi}\int d\bar{\xi} e^{\pm\boldsymbol{\varrho}\cdot\nabla} = \frac{1}{2\pi}\int d\bar{\xi} e^{\pm\varrho\nabla_\perp\cos\bar{\xi}} = J_0\Big(\frac{\varrho\nabla_\perp}{i}\Big), \tag{69}$$

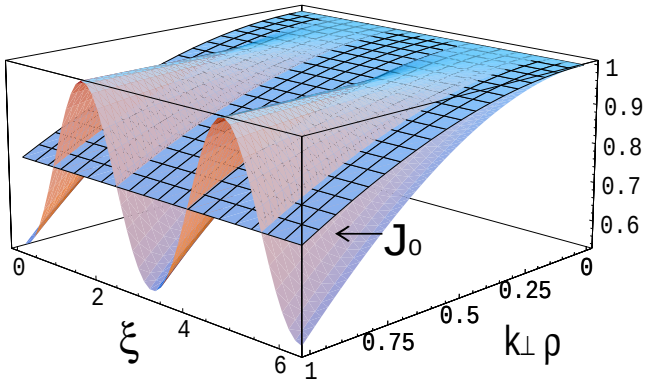

Figure 7: gyroangle averaging: $e^{\varrho k\cos\xi}$ is replaced by ξ-independent Bessel function

we partially perform the $\bar{\xi}$- integration to result in:

$$\begin{aligned} n_{a1}(\mathbf{x}) &= \int d^2\mathbf{v} J_0 f + \int d^2\bar{\mathbf{v}} \frac{e_a}{B}\frac{\partial F_{a0}(\mathbf{x},t)}{\partial\bar{\mu}}(1 - J_0^2)\Big[\phi(\mathbf{x}) - \frac{1}{c}\bar{U}A_\parallel(\mathbf{x})\Big] \\ &+ \int d^3\bar{\mathbf{v}}(e^{\boldsymbol{\varrho}\cdot\nabla} - \langle e^{\boldsymbol{\varrho}\cdot\nabla}\rangle)\Big[\phi(\mathbf{x}) - \frac{1}{c}\bar{U}A_\parallel(\mathbf{x})\Big](e^{-\boldsymbol{\varrho}\cdot\nabla} - 1)\frac{e_a}{B}\frac{\partial F_{a0}(\mathbf{x},t)}{\partial\bar{\mu}} \end{aligned}$$

with $d^2\mathbf{v} = 2\pi(B/m)d\bar{\mu}d\bar{U}$. For the second line the result of the $\bar{\xi}$- integration can not be written in a closed form. But if we now expand all terms dependent on $\varrho\nabla_\perp \sim \varrho k \sim$ up to forth order using the expansion formulae given in Appendix 8.7 and take into account that integrals of the form

$$\int \bar{U}\frac{\partial F_{a0}(\bar{\mathbf{x}},t)}{\partial\bar{\mu}}d\bar{U}$$

are small compared to the other contributions to the perturbed density (since they represent the anisotropy of the equilibrium distribution function; if $F_{a0}(\bar{\mathbf{x}},t)$ is Maxwellian, they are exactly 0), we finally derive [1]:

$$0 = \sum_a \Big[\int d^2\mathbf{v} J_0 f + \frac{e_a}{m_a}\nabla_\perp\frac{n_{a0}}{B^2}\nabla_\perp\phi(\mathbf{x}) + \frac{3e_a v_{th,a}^2 n_{a0}}{8m_a\Omega_a^4}\nabla_\perp^4\phi(\mathbf{x})\Big] \tag{70}$$

To carry out the integration in $\bar{\mu}$ over the 4-th order term, $F_0 \sim e^{-\bar{\mu}B/v_{th}^2}$ was assumed. However, for the second order term no assumption for F_0 is necessary, because a partial integration $\int d\mu\ \mu\partial F/\partial\mu = -\int d\mu F$ can be used.

3.3.2 Ampère's Law

Similar manipulations have to be performed to derive the shear Alfvén version of Ampère's law starting with equation (57). Nevertheless there is one important point that should be mentioned: originating from the addend

$$\Big[\bar{U} - \Delta\frac{e_a}{m_a c}\mathbf{A}_1(\bar{\mathbf{X}} + \bar{\boldsymbol{\varrho}}_{a0}(\bar{\mathbf{Z}}), t)\Big]F_{a0}(\bar{\mathbf{Z}}, t)$$

and using $\int F_{a0}d\bar{U} = -\int \bar{U}\partial F_{a0}/\partial\bar{U}\ d\bar{U}$ a term of 0-th order in ϵ_Δ describing the anisotropy of F_{a0} remains (contrary to the Poisson's equation, where anisotropy terms always showed up in combination with some power of ϱk). This term is kept and singled out later, while deriving the gyrokinetic moment equation [1]. The final result is:

$$[\nabla\times\nabla\times\mathbf{A}_1(\mathbf{x})]_\parallel = \frac{4\pi}{c}\sum_a e_a\left[\int J_0\bar{U}f d^2\mathbf{v} + \int\frac{e}{mc}\frac{\partial F_{a0}}{\partial\bar{U}}\bar{U}A_\parallel d^3\mathbf{v} + \frac{e_a^2 n_{a0}v_{th,a}^2}{2m_a c\Omega_a^2}\nabla_\perp^2 A_\parallel\right] \quad (71)$$

Here the system of linearised equations consisting of (60),(70) and (71) is complete.

3.3.3 The Gyrokinetic Moment Equation

The gyrokinetic moment equation (GKM) is the 0-th order moment of the gyrokinetic equation (60). In the process of deriving [1], Poisson's equation and Ampère's law as given above are used to replace some of the moments. A straightforward but lengthy calculation results in:

$$\begin{aligned} - &\frac{\partial}{\partial t}\frac{e}{m}\nabla_\perp\frac{n_0}{B^2}\nabla_\perp\phi + \nabla A_\parallel\times\mathbf{b}\cdot\nabla(\frac{\nabla\times\mathbf{B}}{B}) + (\mathbf{B}\cdot\nabla)\frac{(\nabla\times\nabla\times\mathbf{A})\cdot\mathbf{B}}{B^2} \\ = &-\sum_a e_a\int\frac{4\pi}{c}\mathbf{v}_d\cdot\nabla J_0 f_a d^3\mathbf{v} + \frac{c}{v_{A0}^2}\frac{3v_{th,a}^2}{4\Omega_a^2}\nabla_\perp^4\frac{\partial\phi(\mathbf{x})}{\partial t} \\ &+\mathbf{B}\cdot\nabla\Big(\frac{4\pi e_a^2 n_{a0}v_{th,a}^2}{2Bm_a c^2\Omega_a^2}\nabla_\perp^2 A_\parallel\Big) + \mathbf{b}\times\nabla(\frac{2\pi e_a n_{0a}v_{th,a}^2}{B\Omega_a})\cdot\nabla\nabla^2\phi \end{aligned} \quad (72)$$

4 Solution in General Tokamak Geometry

Due to the symmetry of a Tokamak (see section 5.1), we introduce the following ansatz for the solution of our system:

$$\phi = \sum_m \phi_m(r) e^{-i\omega t - im\theta + in\varphi} \tag{73}$$

The same ansatz is also made for ψ which is connected to $\mathbf{A}$ as follows:

$$A_\parallel = \frac{c}{i\omega}(\nabla\psi_\parallel)_\parallel$$

Firstly, this ansatz implies that we choose an eigenvalue formulation and not an initial value formulation. Secondly, toroidal modes are completely decoupled because of toroidal symmetry. Finally, coupling due to poloidal inhomogeneities is taken into account by keeping the summation over the poloidal mode number m. As a result we obtain a system of coupled differential equations in radial direction for ϕ, ψ with the complex eigenvalue ω. This set of equations is solved with a finite element method described in section 5.3.

4.1 Splitting off Adiabatic Terms

In this paragraph the adiabatic and non- adiabatic contributions to the velocity space integrals are separated. To proceed further analytically and to carry out the integration, one has to assume a specific form of the equilibrium distribution function. Otherwise, e.g. if F_0 is given only numerically on a grid, no further analytical treatment is possible. On the other hand, if F_0 is Maxwellian, the integration can be carried out completely analytical which is presented in this section. Furthermore, since we are interested also in α-particle physics, where we have a distribution isotropic in the pitch angle and non-isotropic in energy, the results after performing just the pitch-angle-integration are useful. These results will be given in section 4.3.
We start with the following substitution [1]:

$$f = h + H_1 \frac{\partial F_0}{\partial E} - [e\frac{\partial F_0}{\partial E} - \frac{c\nabla F_0}{i\omega B} \cdot (\mathbf{b} \times \nabla)] J_0 \psi \tag{74}$$

This transforms the gyrokinetic equation (60) into:

$$\frac{\partial h}{\partial t} + (U\mathbf{b} + \mathbf{v}_d) \cdot \nabla h = [\frac{c\mathbf{b}}{eB} \times \nabla F_0 \cdot \nabla - \frac{\partial F_0}{\partial E}\frac{\partial}{\partial t}] J_0 [\phi - (1 - \frac{\omega_d}{\omega}\psi)] \tag{75}$$

Here ω_d defined by

$$\omega_d = \frac{\mathbf{v}_d}{i} \cdot \nabla \tag{76}$$

and an exchange of order of the operators $(U\mathbf{b}+\mathbf{v}_d)\cdot\nabla$ and $e_a\partial F_0/\partial E - c/(i\omega B)\nabla F_0\cdot(\mathbf{b}\times\nabla)$ is performed. In this step terms of the order $\epsilon^2=(a/R_0)^2$ are neglected. Here, a stands for the small radius and R_0 for the big radius of a tokamak.
Now the integrals over the velocity space are written more explicitly:

$$\int J_0 f d^3\mathbf{v} = \int J_0 h^3\mathbf{v} + \int J_0[(eJ_0\phi - J_0 U\frac{(\nabla\psi)_\parallel}{i\omega})\frac{\partial F_0}{\partial E} - e\frac{\partial F_0}{\partial E} + \frac{c\nabla F_0}{i\omega B}\cdot(\mathbf{b}\times\nabla)]J_0\psi$$
$$= \int J_0 h^3\mathbf{v} + \int\Big[eJ_0^2\frac{\partial F_0}{\partial E}\phi - eJ_0^2\frac{\partial F_0}{\partial E}\psi - eJ_0^2\frac{\partial F_0}{\partial E}U\frac{(\nabla\psi)_\parallel}{i\omega} - J_0^2\frac{c\mathbf{b}\times\nabla F_0}{i\omega B}\cdot\nabla\psi\Big]d^3\mathbf{v}$$

If F_0 is Maxwellian then we can continue to integrate analytically and derive for the QN-equation [1]:

$$\sum_j e\Big[\int J_0 h d^3\mathbf{v} + \frac{en_0}{T}e^{-\chi}I_0(\chi)\Big[\psi-\phi-\Big(1+\eta G_0(\chi)\Big)\frac{\omega_*}{\omega}\psi\Big]\Big] = 0 \tag{77}$$

with

$$\omega_* \equiv [\frac{cT\mathbf{b}}{ieB}\times\frac{\nabla n}{n}\cdot\nabla]; \qquad \eta\equiv\frac{\nabla T}{T}/\frac{\nabla n}{n} \tag{78}$$

$$\chi\equiv\frac{v_{th}^2k_\perp^2}{2\Omega^2}; \qquad G_0(\chi) = -\chi+\chi I_1(\chi)/I_0(\chi) \tag{79}$$

In contrast to the original derivation by Qin, here the FLR terms in the GKM integrals are kept for consistency. This term can be rewritten as:

$$\begin{aligned}\int e\frac{\mathbf{v}_d}{\omega}\cdot\nabla J_0 f d^3\mathbf{v} &= \int e\frac{\mathbf{v}_d}{\omega}\cdot\nabla J_0 h d^3\mathbf{v} \\ &+ \int e\frac{\mathbf{v}_d}{\omega}\cdot\nabla J_0\Big\{e\frac{\partial F_0}{\partial E}J_0(\phi-\psi) + [c\frac{\nabla F_0}{i\omega B}\cdot(\mathbf{b}\times\nabla) - eU\frac{\partial F_0}{\partial E}\nabla]J_0\psi\Big\}\end{aligned} \tag{80}$$

Using

$$\mathbf{v}_d = -\frac{\mathbf{b}}{eB}\times[mU^2(\mathbf{b}\cdot\nabla)\mathbf{b}+\mu\nabla B],$$

the first term in the curly brackets becomes:

$$\Big\{[\frac{\mathbf{b}}{\omega B}\times(\mathbf{b}\cdot\nabla)\mathbf{b}]\cdot\nabla\int mU^2J_0^2\frac{\partial F_0}{\partial E}d^3\mathbf{v} + [\frac{\mathbf{b}}{\omega B}\times\nabla B]\cdot\nabla\int\mu J_0^2\frac{\partial F_0}{\partial E}d^3\mathbf{v}\Big\}e(\phi-\psi)$$

Assuming a Maxwellian F_0 results in:

$$\frac{\mathbf{b}}{\omega B}\times\Big[(\mathbf{b}\cdot\nabla)\mathbf{b}+(1+G_0)\frac{\nabla B}{B}\Big]\cdot\nabla en_0e^{-\chi}I_0(\chi)(\psi-\phi)$$

Here, $(\mathbf{b}\times\nabla B)\cdot\nabla(1/B) = (\mathbf{b}\times\nabla B)\cdot(-\nabla B/B^2) = 0$ is used. The second term in curly brackets of equation (80) is treated similarly to become:

$$\begin{aligned}-[\frac{\mathbf{b}}{\omega B}\times(\mathbf{b}\cdot\nabla)\mathbf{b}]\cdot\nabla\Big\{\frac{c}{i\omega B}\int mU^2J_0^2\nabla F_0 d^3\mathbf{v}\cdot(\mathbf{b}\times\nabla) - e\int mU^3J_0^2\frac{\partial F_0}{\partial E}d^3\mathbf{v}\Big\}\psi \\ -[\frac{\mathbf{b}}{\omega B}\times\nabla B]\cdot\nabla\Big\{\frac{c}{i\omega B}\int\mu J_0^2\nabla F_0 d^3\mathbf{v}\cdot(\mathbf{b}\times\nabla) - e\int\mu UJ_0^2\frac{\partial F_0}{\partial E}d^3\mathbf{v}\Big\}\psi\end{aligned}$$

Using again a Maxwellian F_0 gives :

$$
\begin{aligned}
- \quad & [\frac{\mathbf{b}}{\omega B} \times (\mathbf{b}\cdot\nabla)\mathbf{b}] \cdot \nabla\Big\{e_a n_0(r) e^{-\chi} I_0([1+\eta+\eta G_0)]\frac{\omega_*}{\omega}\psi\Big\} \\
- \quad & [\frac{\mathbf{b}}{\omega B} \times \frac{\nabla B}{B}] \cdot \nabla\Big\{e_a n_0(r) e^{-\chi} I_0[(1+\eta)(1+G_0) + 2\eta(G_1 - G_0)]\frac{\omega_*}{\omega}\psi\Big\}
\end{aligned}
$$

with $G_1 = -2\chi + 2\chi I_1/3I_0 + \chi^2 - \chi^2 I_1/I_0$. Combining these two results gives:

$$
\begin{aligned}
& [\frac{\mathbf{b}}{\omega B} \times (\mathbf{b}\cdot\nabla)\mathbf{b}] \cdot \nabla e_a n_0(r) e^{-\chi} I_0\Big[\psi - \phi - (1+\eta+\eta G_0)\frac{\omega_*}{\omega}\psi\Big] \qquad (81) \\
+ \quad & [\frac{\mathbf{b}}{\omega B} \times (1+G_0)\frac{\nabla B}{B}] \cdot \nabla e_a n_0(r) e^{-\chi} I_0\Big[\psi - \phi - (1+\eta+\frac{2\eta(G_1-G_0)}{1+G_0}]\frac{\omega_*}{\omega}\psi\Big\}
\end{aligned}
$$

When FLR terms are left out, these equations can be simplified to recover Qin's result [1]. (This will be also discussed in the next section.)

4.2 Ideal MHD Limit

In case of ideal MHD the QN and GKM equation can be simplified [1]: all the kinetic integrals containing h are left out and FLR-effects are neglected by taking the $\chi \propto \varrho k_\perp \to 0$ limit:

$$
e^{-\chi} I_0 \to 1 \quad \text{and} \quad G_0, G_1 \to 0 \quad \text{for} \quad \chi \to 0 \qquad (82)
$$

In this limit together with $\omega_* \ll \omega_{A0} = v_{A0}/R = \sqrt{B_0^2/\mu_0 n_0 m}/R$ the QN equation (77) immediately reduces to

$$
\psi - \phi = 0
$$

This is consistent with the fact that there is no parallel dynamics contained in the ideal MHD model:

$$
E_{1\parallel} = -\nabla\phi - \frac{\partial A_{1\parallel}}{\partial t} = 0 \qquad (83)
$$

With $A_{1\parallel} = \nabla_\parallel \psi / i\omega$, one deduces again:

$$
\psi = \phi \qquad (84)
$$

For the GKM equation, we first simplify line (81): removing all gyro-terms according to the rules (82) gives back Qin's result. Then we use $\psi - \phi = 0$ and apply a relation based on the definition of ω_* (78):

$$
-e n_0(r)[1+\eta]\frac{\omega_*}{\omega} = c\Big[\frac{T\nabla n + n\nabla T}{i\omega B} \times \mathbf{b}\Big] \cdot \nabla = \frac{c\nabla[P(r)]}{i\omega B} \cdot (\mathbf{b} \times \nabla),
$$

The result is put in (72) to obtain the final MHD version of the GKM equation (now in SI units):

$$-\frac{\omega^2}{\omega_{A0}^2}\nabla_\perp\frac{\hat{n}B_0^2}{\mathbf{B}^2}\nabla_\perp\psi \quad + \quad \nabla(\nabla_\parallel\psi)\times\mathbf{b}\cdot\nabla(\frac{\nabla\times\mathbf{B}_0}{B}) + (\mathbf{B}\cdot\nabla)\frac{(\nabla\times\nabla\times\nabla_\parallel\psi)\cdot\mathbf{B}}{B^2} +$$
$$+ \quad \mu_0 P_0\frac{\mathbf{b}}{B}\times\left[(\mathbf{b}\cdot\nabla)\mathbf{b}+\frac{\nabla B}{B}\right]\cdot\nabla\left[\frac{\nabla\hat{P}}{B}(\mathbf{b}\times\nabla)\psi\right] = 0 \qquad (85)$$

with $\hat{P}$ and $\hat{n}$ are the normalised pressure resp. density. To compare with the equation for shear Alfvén modes derived from the standard MHD model, one identifies $\frac{\nabla P}{i\omega B}(\mathbf{b}\times\nabla)\psi$ with the perturbed pressure and uses the vector identity (66). Then one obtains for the pressure term (4-th addend):

$$\mu_0\nabla P_1\cdot\nabla\times\frac{\mathbf{B}}{B^2}$$

From the ideal MHD side, line (85) can be derived using $\nabla\mathbf{j}_1 = 0$, the linearised force balance and ideal Ohm's law [1]. Therefore all ideal MHD results can be recovered from the GKM equation.

4.3 α-Particles

Due to their high energies compared to the background, fusion born α-particles are not Maxwellian. Instead, one usually chooses the following distribution function:

$$F_0 = C_\psi F_{0\psi}\cdot\frac{C_E}{E^{3/2}+E_c^{3/2}}\mathrm{Erfc}[\frac{E-E_0}{\Delta E}] \qquad (86)$$

This expression is called 'slowing-down' (see figure 8), because it describes the drag of the background electrons and ions on the fusion born α's, derived from the Fokker-Planck equation under the assumptions that D and T have the same energy T_i and the energy spectrum is approximately Gaussian [39].
For $F_{0\psi}$ one often uses $1/(exp[(\psi-\psi_0)/\Delta\psi]+1)$ or also $(1-s^2)^3$ with $s\propto\sqrt{\psi}$. Parameters that are likely to fit the ITER experiment [40] are:

$$\Delta E = 335.2\mathrm{keV},\ \ E_0 = 3520\mathrm{keV},\ \ E_c = 329.6\mathrm{keV},\ \ \psi_0 = 0.2,\ \ \Delta\psi = 1/14$$

Since this distribution is given in terms of E, a coordinate change from U,μ to E,Λ is advantageous:

$$\begin{aligned} d^2\mathbf{v} &= 2\pi\int_0^\infty dU\int_{-\infty}^\infty v_\perp dv_\perp = 2\pi\int_0^\infty\frac{dE}{m^2}\int_0^{E/B}\sum_\sigma\frac{Bd\mu}{\sqrt{2(E-\mu B)/m}} \\ &= 2\pi\int_0^\infty\frac{dE\sqrt{E}}{m^2}\int_0^b\sum_\sigma\frac{d\Lambda}{b\sqrt{2(1-\Lambda/b)/m}} \end{aligned} \qquad (87)$$

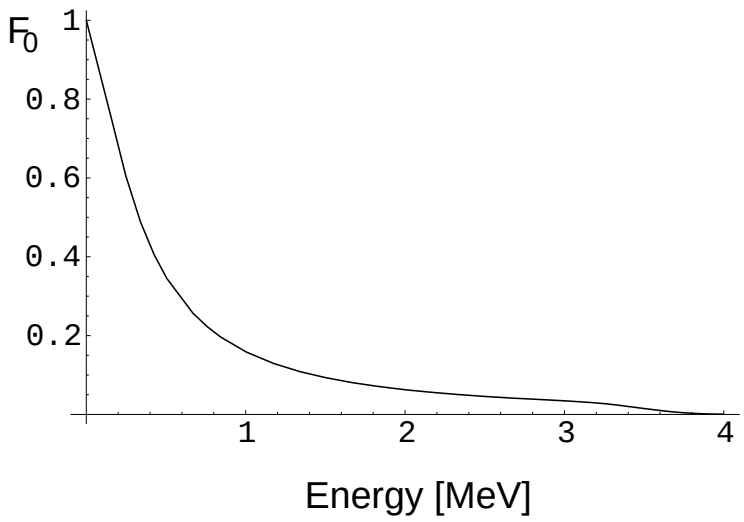

Figure 8: Energy dependence of a slowing down distribution function with ITER parameters

Here

$$b = \frac{B_0}{B}, \qquad \Lambda = \frac{\mu B_0}{E},$$

The summation over σ is due to positive and negative direction of U. Partial derivatives expressed in the new coordinates are:

$$\frac{\partial F_0}{\partial \mu} = B\frac{\partial F_0}{\partial E}, \qquad \frac{\partial F_0}{\partial U} = mU\frac{\partial F_0}{\partial E}$$

Integration over Λ can be carried out analytically:

$$\int_0^b \frac{d\Lambda}{b\sqrt{1-\Lambda/b}} = 2, \quad \int_0^b \frac{d\Lambda\mu B}{b\sqrt{1-\Lambda/b}} = \frac{4E}{3}$$

$$\int_0^b \frac{d\Lambda J_0(\frac{k}{\Omega}\sqrt{\frac{2E\Lambda}{mb}})^2}{b\sqrt{1-\Lambda/b}} = 2\,{}_1F_2[\frac{1}{2};1,\frac{3}{2};-\frac{2k^2E}{m\Omega^2}]$$

$$\int_0^b \frac{d\Lambda\mu B J_0(\frac{k}{\Omega}\sqrt{\frac{2E\Lambda}{mb}})^2}{b\sqrt{1-\Lambda/b}} = \frac{4E}{3}\Big\{{}_1F_2[\frac{1}{2};1,\frac{5}{2};-\frac{2k^2E}{m\Omega^2}] - \frac{2Ek^2}{5m\Omega^2}\,{}_1F_2[\frac{1}{2};2,\frac{7}{2};-\frac{2k^2E}{m\Omega^2}]\Big\}$$

Here generalised hypergeometric functions ${}_pF_q(a_1,...,a_p;b_1,...,b_q,z)$ are used. Furthermore integrals with an odd power of U vanish due to the fact, that $F_{\alpha 0}$ is symmetric in U, for example:

$$\sum_\sigma \int dE \frac{\partial F_0}{\partial E} U = \sum_\sigma \int dE \frac{\partial F_0}{\partial E} \sigma \sqrt{\frac{2E}{m}(1-\Lambda/b)} = 0$$

(For heating schemes with an asymmetic distribution in U this simplification is not valid any more.)
Straightforward calculation shows that the pressure is isotropic:

$$\frac{P_\perp}{P_\parallel} = \frac{\int d^3\mathbf{v}\mu B F_0}{\int d^3\mathbf{v} m U^2 F_0} = 1 \tag{88}$$

For the values given above, the energy integrals can be computed numerically to obtain the normalisation factors:

$$1 = \int d^3v F_0 \quad \Rightarrow$$

$$\int_0^\infty dE\sqrt{E}\frac{1}{E^{3/2}+E_c^{3/2}}\mathrm{Erfc}[\frac{E-E_0}{\Delta E}] \equiv Y_0 = 4.7709, \quad \rightarrow \quad C_E = \frac{m^{3/2}}{Y_0 4\sqrt{2}\pi}$$

The constant C_ψ can be determined, if we prescribe e.g. a $\beta_{\alpha 0}$ on the magnetic axis:

$$\beta_{\alpha 0} = \frac{2\mu_0 P}{B_0^2} = \frac{2\mu_0 P_\parallel}{B_0^2}; \quad \rightarrow \quad C_\psi = \frac{\beta_{\alpha 0} B_0^2}{2\mu_0}\frac{3Y_0}{4Y_1}F_{\psi 0}(\psi = 0)$$

with

$$Y_1 = \int_0^\infty dE \frac{E^{3/2}}{E^{3/2}+E_c^{3/2}}\mathrm{Erfc}[\frac{E-E_0}{\Delta E}] = 5.84703\mathrm{MeV}$$

The QN and the GKM stay in the same form as for a Maxwellian F_0, but the energy integrals now have to be carried out numerically: $-n/T$ has to be replaced by $\int d\mathbf{v}^2 \partial F_0/\partial E$. For the parameters given above, this integral can be carried out when FLR effects are dropped:

$$\int d\mathbf{v}^2 \partial F_0/\partial E = \frac{n(\psi)}{0.667\mathrm{MeV}} \tag{89}$$

With the J_0 operator present, no closed form of the integral can be found. An evaluation is only possible at runtime, when a guess for $k_\perp$ is available. In LIGKA so far the following appoximation is implemented: together with the replacement rule (89) the same gyro-corrections as in formulae (77) and (81) are used with $2v_{th}^2/m$ replaced by the 'α-temperature' 0.667MeV. The non-Maxwallian F_0 is also taken into account in the integral terms $\int d^3\mathbf{v} J_0 h$ and $\int e\frac{\mathbf{v}_d}{\omega}\cdot\nabla J_0 h d^3\mathbf{v}$ through $\frac{\partial F_0}{\partial E}$. Additional terms of order $\mathcal{O}(\epsilon^2)$ and $\mathcal{O}(\epsilon\cdot\epsilon_B)$ are neglected during the process of splitting off the adiabatic pressure part.

4.4 Kinetic Integrals

In order to complete the QN and GKM equation, a solution for the non-adiabatic part h has to be found. This solution is inserted in the integrals $\int d^3\mathbf{v} J_0 h$ and $\int e\frac{\mathbf{v}_d}{\omega}\cdot\nabla J_0 h d^3\mathbf{v}$.

Then only two unknown variables remain: the electrostatic (ϕ) and parallel electromagnetic (ψ) potential .

The expression for h is a nonlocal relation: i.e. the current position of the particle in phase space depends on the field seen by the particle along its previous path. Starting from equation (75), the formal solution for h (now in SI units)[43],[1] reads:

$$\begin{aligned} h &= \int_{-\infty}^{t} dt' \Big[\frac{\mathbf{b}}{eB(\mathbf{x}')} \times \nabla F_0(r') \cdot \nabla - \frac{\partial F_0(r')}{\partial E} \frac{\partial}{\partial t'} \Big] e_a J_0 \Big[\phi(\mathbf{x}', t') - (1 - \frac{\omega_d(\mathbf{x}')}{\omega} \psi(\mathbf{x}', t')) \Big]] \\ &= ie_a \int_{-\infty}^{t} dt' \frac{\partial F_0(r')}{\partial E} \Big[\omega - \hat{\omega}_*(\mathbf{x}) \Big] J_0 \Big[\phi(\mathbf{x}', t') - (1 - \frac{\omega_d(\mathbf{x}')}{\omega} \psi(\mathbf{x}', t')) \Big] \end{aligned} \tag{90}$$

with a generalised $\hat{\omega}_*$:

$$\hat{\omega}_* = -\frac{\mathbf{b} \times \nabla F_0}{ieB \frac{\partial F_0}{\partial E}} \cdot \nabla \tag{91}$$

which simplifies to $\omega_*[1 + \eta(E/T - 3/2)]$ if a Maxwellian F_0 is chosen and the integration over velocity space is carried out. Physically, the term proportional to ω_* describes the free energy that is available to the system through the spatial gradients of the distribution function.

The dashes in (90) indicate, that the quantities have to be evaluated on the position of the particle, i.e along the unperturbed particle orbits.

Since our model is linear, we pull out ϕ and ψ and integrate over the unperturbed orbits. This pull out procedure for the θ'-dependence of ϕ and ψ is performed by an expansion of the propagator in bounce harmonics. For the radial dependence, it is advantageous to distinguish between particle orbits with large and small radial drifts: electrons and circulating ions are considered to have no r'-dependence. For trapped ions, this approximation is not valid. (A detailed discussion of these assumptions will be given in section 6.2.) Therefore for trapped ions, Qin [1] employed a Taylor expansion up to second order in the banana width. However, this approximation becomes inaccurate, when particles with large excursions are considered: as shown in section 5.4 and 6.2, the orbit width Δ_b for energetic ions near the trapped/passing boundary can be more than 50% of the minor radius a. Obviously in that case the expansion parameter Δ_b/Δ_m (with Δ_m as typical radial mode width) is not small any more, even for large scale MHD modes such as internal kinks (here Δ_m depends on the $q = 1$ surface, typically $\sim 0.4a$) or TAE modes ($\Delta_m \sim 0.2 - 0.4$).

Following a suggestion from A. Koenies, here for the first time a more accurate method is used: the orbit integral is discretised radially in the same way as the unknown potentials. The time and phase information needed for this process is supplied by the numerical particle orbit integration (see 5.4.2).

Now the steps summed up above are carried out. Applying ansatz (73) and expanding

$$h = \hat{h} e^{in\phi - i\omega t}$$

gives:

$$\begin{aligned} \hat{h} &= ieF_0 \sum_m \int_{-\infty}^{t} dt' e^{i[n(\varphi'-\varphi)-m(\theta'-\theta)-\omega(t'-t)]} e^{-im\theta} \\ & \frac{\partial F_0}{\partial E} \left[\omega - \hat{\omega}_*\right] J_0 \left[\phi_m(r') - (1 - \frac{\omega_d(r',\theta')}{\omega})\psi_m(r')\right] \end{aligned} \tag{92}$$

The phase factor

$$e^{i[n(\varphi'-\varphi)-m(\theta'-\theta)-\omega(t'-t)]} \tag{93}$$

is rewritten in a more convenient way using the following definitions [43]:

$$n(\varphi'-\varphi) - m(\theta'-\theta) = \int_t^{t'} dt''(n\frac{d\varphi}{dt''} - m\frac{d\theta}{dt''}) \tag{94}$$

$$\omega_D = \frac{d\varphi}{dt} - q(r^0)\frac{d\theta}{dt} \tag{95}$$

r^0 is the orbit averaged radial position of a particle.

$$\omega_D^0 = \frac{1}{\tau_{b,t}} \int dt \omega_D; \qquad S_m(r^0) = nq(r^0) - m \tag{96}$$

$$W = W(t) = \int_0^t dt'' \Delta\omega_D; \qquad W' = W(t') = \int_0^{t'} dt'' \Delta\omega_D; \qquad \Delta\omega_D = \omega_D - \omega_D^0 \tag{97}$$

Since the particle motion is periodic -for both trapped and circulating particles - expression (93) is now expanded in 'bounce' harmonics :

$$\begin{aligned} & e^{i\left[\omega_D^0(t'-t) - W + W' + S_m^0(\theta'-\theta) + H\sigma S_m^0 \omega_t(t'-t) - H\sigma S_m^0 \omega_t(t'-t) - \omega(t'-t)\right]} = \\ & e^{-i\left[\omega - \omega_D^0 - H\sigma S_m^0 \omega_t\right](t'-t)} \cdot \underbrace{e^{i\left[S_m^0(\theta'-\theta) - H\sigma S_m^0 \omega_t(t'-t) + W' - W\right]}}_{=\alpha = \sum_k a_{km} e^{ik\omega_{b,t}(t'-t)}} \end{aligned} \tag{98}$$

$$\begin{aligned} \alpha &= e^{i\left[S_m^0 \theta' - H\sigma S_m^0 \omega_t(t'-t_0) + W'\right]} \cdot e^{-i\left[S_m^0 \theta - H\sigma S_m^0 \omega_t(t-t_0) + W\right]} \\ &= \sum_k \hat{a}_{km} e^{-i\left[S_m^0 \theta - H\sigma S_m^0 \omega_t \hat{t} + W\right]} e^{ik\omega_{b,t}(t-t_0)} e^{ik\omega_{b,t}(t'-t)} \\ &= \sum_k a_{km} e^{ik\omega_{b,t}(t'-t)} \end{aligned} \tag{99}$$

with

$$\begin{aligned}\hat{a}_{km} &= \frac{1}{\tau_{b,t}}\int_{-\tau_{b,t}/2}^{\tau_{b,t}/2} dt' e^{i\left[S_m^0\theta' - H\sigma S_m^0\omega_t(t'-t_0)+W'\right]} e^{ik\omega_{b,t}(t'-t_0)} \\ &= \frac{1}{\tau_{b,t}}\int_{-\tau_{b,t}/2}^{\tau_{b,t}/2} d\hat{t}' e^{i\left[S_m^0\theta' - H\sigma S_m^0\omega_t\hat{t}'+W'\right]} e^{ik\omega_{b,t}\hat{t}'} \end{aligned} \tag{100}$$

Here, $\hat{t} = t - t_0$, $\hat{t}' = t' - t_0$; note that $dt' = d\hat{t}'$.
Similarly,

$$\hat{a}_{km}^G = \frac{1}{\tau_{b,t}}\int_{-\tau_{b,t}/2}^{\tau_{b,t}/2} d\hat{t}' \frac{\omega_d(r',\theta')}{\bar{\omega}_d(r)} e^{i\left[S_m^0\theta' - H\sigma S_m^0\omega_t\hat{t}'+W'\right]} e^{ik\omega_{b,t}\hat{t}'} \tag{101}$$

H represents the Heavy-side function and indicates that $H\sigma S_m^0\omega_t\hat{t}'$ is 0 for trapped particles and $\sigma S_m^0\omega_t\hat{t}'$ for circulating particles. With the expansion above, the perturbed distribution function h becomes :

$$\begin{aligned} h &= ie\sum_m\sum_k \int_{-\infty}^{t} dt' e^{-i(\omega-\omega_D^0 - H\sigma S_m^0\omega_t - k\omega_{b,t})(t'-t)} e^{-im\theta} \\ &\quad \frac{\partial F_0}{\partial E}\left[\omega - \hat{\omega}_*\right] J_0\left[a_{km}\phi_m(r') - (a_{km} - \frac{a_{km}^G\bar{\omega}_d(r)}{\omega})\psi_m(r')\right] \end{aligned} \tag{102}$$

In the zero orbit width approximation the integration over t' can be performed and one yields :

$$h = -e_a\sum_m\sum_k \underbrace{\frac{\frac{\partial F_0}{\partial E}(\omega-\hat{\omega}_*)e^{-im\theta}J_0}{(\omega - \omega_D^0 - H\sigma S_m^0\omega_t - k\omega_{b,t})}}_{=\mathcal{R}_{m,k}}\left[a_{km}\phi_m(r) - (a_{km} - \frac{a_{km}^G\bar{\omega}_d(r)}{\omega})\psi_m(r)\right] \tag{103}$$

Here it is assumed that the perturbation vanishes at $t' \to -\infty$.
Here the term responsible for Landau damping shows up for the first time: the denominator $\omega - \omega_D^0 - H\sigma S_m^0\omega_t - k\omega_{b,t}$ can become very small (for complex ω) or even zero (for a pure real ω). In that case the particle is resonant with the wave and an energy exchange is possible.
For trapped particles with wide orbits, of course, approximation (103) is not sufficient. Thus the trapped particle case is treated separately (see below).
Nevertheless the formal integration over the velocity space can be carried out for all particles together. Using the following relations and definitions (similar to section 4.3) we change again to the(E,Λ) coordinate system:

$$\lambda = \frac{v_\parallel}{v}; \qquad \Lambda = \frac{\mu B_0}{E}; \qquad b(r,\theta) = \frac{B_0}{B(r,\theta)}; \qquad Y = \frac{E}{T} \tag{104}$$

$$v_\parallel = \pm\sqrt{\frac{2}{m}[E - \mu B(r,\theta)]} = \pm v\sqrt{1 - \frac{\Lambda}{b(r,\theta)}}; \qquad v_\perp dv_\perp = \frac{dE}{m} \tag{105}$$

thus,

$$\lambda = \pm\sqrt{1-\frac{\Lambda}{b(r,\theta)}} \qquad \text{and} \qquad \frac{d\lambda}{d\Lambda} = \frac{\mp 1}{2b(r,\theta)\sqrt{1-\frac{\Lambda}{b(r,\theta)}}} \quad , \tag{106}$$

Now we integrate over energy and pitch angle:

$$\begin{aligned}
\int h d^3\mathbf{v} &= 2\pi \int_0^\infty v_\perp dv_\perp \int_{-\infty}^\infty dv_\parallel h \\
&= 2\pi \int_0^\infty \frac{dE}{m} \int_{-1}^1 v d\lambda \; h \\
&= \pi (\frac{2T}{m})^{\frac{3}{2}} \int_0^\infty dY \sqrt{Y} \int_{-1}^1 d\lambda \; h \\
&= \frac{\pi}{2} (\frac{2T}{m})^{\frac{3}{2}} \int_0^\infty dY \sqrt{Y} \sum_\sigma \int_0^{b(r,\theta)} \frac{d\Lambda \; h}{b(r,\theta)\sqrt{1-\frac{\Lambda}{b(r,\theta)}}}
\end{aligned} \tag{107}$$

In the process of solving for h in terms of ϕ and ψ we project the sum over m into a system of coupled differential equations in radial direction. In order to do so, we apply the projection operator $\int_{-\pi}^{\pi} \frac{d\theta}{2\pi} e^{ip\theta}$ to our equations. To exchange the integration order of θ and Λ, the relation

$$\begin{aligned}
\int_{-\pi}^{\pi} \frac{d\theta}{2\pi} \int_0^{b(r,\theta)} d\Lambda &= \int_{-\pi}^{\pi} \frac{d\theta}{2\pi} \int_0^{b_{min}(r)} d\Lambda + \int_{-\pi}^{\pi} \frac{d\theta}{2\pi} \int_{b_{min}(r)}^{b(\theta)} d\Lambda \\
&= \int_0^{b_{min}(r)} d\Lambda \int_{-\pi}^{\pi} \frac{d\theta}{2\pi} + \int_{b_{min}(r)}^{b_{max}(r)} d\Lambda \int_{\theta^-}^{\theta^+} \frac{d\theta}{2\pi}
\end{aligned} \tag{108}$$

has to be considered. b_{min} and b_{max} are the minimal resp. maximal values of $b(r,\theta)$ on a given flux surface.
This again suggests to treat trapped and circulating particles separately:

4.4.1 Circulating Particles

For circulating particles the radial excursion of the particle orbit is small (at least a factor of 2 smaller than trapped orbits). Thus ω_D^0 and the W resp. W' dependence of the integrals $K_{m,p,k}$ and $a_{m,k}$ can be neglected. Furthermore, all the equilibrium and perturbed quantities are taken at radial position r^0, i.e. they are considered to be constant along the particle orbit. These simplifications also imply, that there is no distinction between co- and counter-passing particles. Then the summation over σ can be performed: using $\frac{1}{a-b}+\frac{1}{a+b} = \frac{2a}{a^2-b^2}$, applying symmetry properties for $\hat{t}$ and changing the dummy summation

index k to $-k$, one derives as the circulating particle contribution:

$$\left(\int_{-\pi}^{\pi}\frac{d\theta}{2\pi}e^{ip\theta}\int J_0 h d^3\mathbf{v}\right)^{circ} = -\pi e_a v_{th}^3 \sum_m \int_0^{b_{min}(r^0)} d\Lambda \int_0^{\infty} dY\sqrt{Y}\cdot$$
$$\sum_k \frac{\partial F_0}{\partial E}\frac{(\omega-\hat{\omega}_*)\omega}{\omega^2-(S_m^0+k)^2\omega_t^2}K_{m,p,k}\cdot J_0^2\left[\hat{a}_{km}\phi_m(r^0)-(\hat{a}_{km}-\frac{\hat{a}_{km}^G\bar{\omega}_d(r^0)}{\omega})\psi_m(r^0)\right] \quad (109)$$

with

$$K_{m,p,k} = \frac{1}{2\pi}\int_{-\pi}^{\pi}\frac{d\theta}{b(r,\theta)\sqrt{1-\frac{\Lambda}{b(r,\theta)}}}e^{-i\left[S_p^0\theta-(k+S_m^0)\omega_t\hat{t}(\theta)\right]}, \quad (110)$$

$$\hat{a}_{m,k} = \frac{1}{\tau_t}\int_{-\tau_t/2}^{\tau_t/2} d\hat{t}' e^{i\left[S_m^0\theta'-(k+S_m^0)\omega_t\hat{t}'\right]} \quad (111)$$

and

$$S_p^0 = nq(r^0)-p$$

If ω_* and $J_0(k_\perp\varrho)$ are considered to be independent of the poloidal angle (KIN2DEM), only K_{mpk} and a_{mk} are responsible for poloidal coupling within the kinetic integrals. Here it is also examined how to include coupling terms caused by the operators ω_* and $J_0(k_\perp\varrho)$. Starting with the abbreviation

$$C^c(r^0,\theta) = \frac{\left(\omega-\hat{\omega}_*(r^0,\theta)\right)\omega}{\omega^2-(S_m^0+k)^2\omega_t^2}\cdot J_0^2\left(k_\perp(r^0,\theta)\varrho\right)$$

and its poloidal expansion

$$C^c(r^0,\theta) = \sum_{\nu=-\infty}^{\infty} C_\nu^c(r^0)e^{i\nu\theta}$$

the θ-integration becomes:

$$\sum_k \frac{\partial F_0}{\partial E}\frac{1}{2\pi}\int_{-\pi}^{\pi}\frac{d\theta\sum_\nu C_\nu^c(r^0)e^{i\nu\theta}e^{-i\left[S_p^0\theta-(k+S_m^0)\omega_t\hat{t}(\theta)\right]}}{b(r,\theta)\sqrt{1-\frac{\Lambda}{b(r,\theta)}}} = \quad (112)$$

$$\sum_k\sum_\nu C_\nu^c(r^0)\frac{\partial F_0}{\partial E}\frac{1}{2\pi}\int_{-\pi}^{\pi}\frac{d\theta e^{-i\left[(nq-p-\nu)\theta-(k+S_m^0)\omega_t\hat{t}(\theta)\right]}}{b(r,\theta)\sqrt{1-\frac{\Lambda}{b(r,\theta)}}} = \quad (113)$$

$$\sum_k\sum_\nu C_\nu^c(r^0)\frac{\partial F_0}{\partial E}K_{m,p,k,\nu} \quad (114)$$

At first sight this complicates the problem considerably because the orbit integral K now depends also on ν. But since the relation

$$K_{m,p,k,\nu} = K_{m,p+\nu,k}$$

holds and ν is in the range of $[-2;2]$ (because only poloidal coupling up to the second order is taken into account) for all applications in this work, no extra effort is needed when $K_{m,p,k}$ is calculated.
Another issue are the radial derivatives caused by the operator $J_0(k_\perp \varrho)$. There are three different ways of handling this problem:

- If the mode structure permits, they are completely neglected and only the θ- dependent terms are taken into account. This is how e.g. KIN2DEM is set up. For an internal kink, this causes considerable errors since $k_\perp \varrho$ near the $q = 1$-surface is dominated by the radial contribution due to a large ratio ϕ'/ϕ (up to ~ 20).

- As a fast and simple workaround, the pure MHD structure of the mode can be used to calculate $k_\perp$. Strictly speaking, this breaks self consistency, but since in a lot of cases the MHD eigenfunction is already a reasonable guess for the final mode structure, and it enters the system only through J_0^2, this procedure is sufficient for many application cases.

- The operator can be expanded up to second order and the result is added to the contributions of the first and second order derivative coefficients from the MHD part.

To compare with the results of R.Marchand in [43] and Qin [1], we simplify the system by applying the large aspect ratio approximation for tokamaks with circular flux surfaces:

$$d\hat{t}' = \frac{dt}{dl}\frac{dl}{d\theta}d\theta = \frac{\sqrt{g_{22}}\sqrt{1+\frac{B_\phi^2}{B_\theta^2}}d\theta}{v_\parallel} = \frac{\sqrt{g_{22}}Bd\theta}{B_\theta v_\parallel} = \frac{qR_0 d\theta}{\sqrt{\frac{2E}{m}}b(r,\theta)\sqrt{1-\frac{\Lambda}{b(r,\theta)}}} \tag{115}$$

$$\Rightarrow \quad \tau_t a_{m,k} \approx \frac{q_0 R_0}{\sqrt{\frac{2E}{m}}}\int_{-\pi}^{\pi}\frac{d\theta}{b(r,\theta)\sqrt{1-\frac{\Lambda}{b(r,\theta)}}}\cos\left[S_m^0\theta - (k+S_m^0)\omega_t\hat{t}\right] = \frac{2\pi q_0 R_0}{\sqrt{\frac{2E}{m}}}K_{m,m,k} \tag{116}$$

Introducing the bounce resp. transit length L_t:

$$L_t = \frac{1}{2\pi}\int_{-\pi}^{\pi}\frac{d\theta}{b(r,\theta)\sqrt{1-\frac{\Lambda}{b(r,\theta)}}} \approx \frac{\sqrt{\frac{2E}{m}}}{2\pi q R_0}\tau_t \tag{117}$$

one can write:

$$a_{m,k} = \frac{K_{m,m,k}}{L_t} \tag{118}$$

This is the simplified version derived by R.Marchand used by Qin for KIN2DEM.

4.4.2 Trapped Particles

To take into account a finite banana width, which is important especially for trapped particles, one should note that in a linear description, where the orbit integrals are performed over unperturbed orbits it is possible to change the order of time integration and the discretisation of the perturbed potentials in radial direction [51]. Thus, the time integral can be written as a sum of integrals:

$$\int_{-\infty}^{t} dt' = \int_{t_1}^{t_2} dt' + \int_{t_2}^{t_3} dt' + ... = \sum_{j'} \int_{t_{j'}}^{t_{j'+1}} dt' \tag{119}$$

The index j' counts the finite element partitions in the radial coordinate: the particle spends the time $t_{j'+1} - t_{j'}$ in the radial bin with number j' (see figure 9).

The time integration has to be started at $t' \to -\infty$. Taking into consideration that the orbit motion is periodic, one obtains:

$$\begin{aligned}
&\int_{-\infty}^{t} dt' e^{-i(\omega-\omega_D^0-k\omega_b)(t'-t)}\psi(r') = \\
= &\sum_{\kappa=0}^{\infty} \int_{t-(\kappa+1)\tau_b}^{t-\kappa\tau_b} dt' e^{-i(\omega-\omega_D^0-k\omega_b)(t'-t)}\psi(r') = \\
= &\sum_{\kappa=0}^{\infty} \sum_{j=0}^{N-1} \int_{t-\kappa\tau_b-t_{j+1}}^{t-\kappa\tau_b-t_j} dt' e^{-i(\omega-\omega_D^0-k\omega_b)(t'-t)}\psi(r_j) = \\
= &\sum_{\kappa=0}^{\infty} \sum_{j=0}^{N-1} \frac{\left[e^{-i(\omega-\omega_D^0-k\omega_b)(-\kappa\tau_b-t_j)} - e^{-i(\omega-\omega_D^0-k\omega_b)(-\kappa\tau_b-t_{j+1})}\right]}{-i(\omega-\omega_D^0-k\omega_b)}\psi(r_j) = \\
= &\sum_{j=0}^{N-1} \frac{e^{i(\omega-\omega_D^0-k\omega_b)t_j}[1-e^{i(\omega-\omega_D^0-k\omega_b)(t_{j+1}-t_j)}]}{-i(\omega-\omega_D^0-k\omega_b)[1-e^{i(\omega-\omega_D^0-k\omega_b)\tau_b}]}\psi(r_j)
\end{aligned} \tag{120}$$

where the relation

$$\sum_{\kappa=0}^{\infty} e^{ix\kappa} = \frac{1}{1-e^{ix}}$$

was used.

It can be easily verified that for $N = 1$, $t_j = 0$ and $t_{j+1} = \tau_b$, expression (120) simplifies to the zero-orbit-width result: $-1/i(\omega - \omega_D^0 - k\omega_b)$. Now we can integrate h over the velocity space and over θ, like above for circulating particles .
The final expression for trapped particles after performing the σ summation is:

$$\left(\int_{-\pi}^{\pi} \frac{d\theta}{2\pi} e^{ip\theta} \int J_0 h d^3\mathbf{v}\right)^{trap} = -\pi e_a v_{th}^3 \sum_m \sum_j \int_{b_{min}(r)}^{b_{max}(r)} d\Lambda \int_0^{\infty} dY \sqrt{Y} \frac{\partial F_0}{\partial E} \sum_k \sum_\nu$$

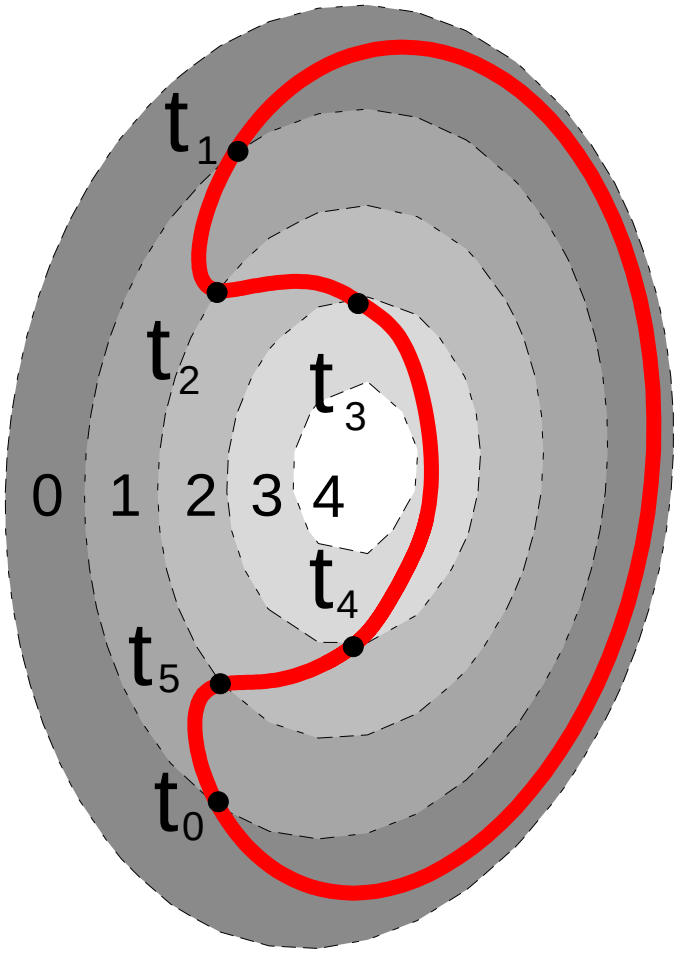

Figure 9: The orbit for trapped particles is split up in pieces corresponding to the finite element discretisation

$$\cdot \mathcal{R}_{kj} \cdot K_{kp\nu} \cdot C^t_\nu(r^0) \cdot \left[\hat{a}_{km}\phi_m(r_j) - \left(\hat{a}_{km} - \frac{\hat{a}^G_{km}\bar{\omega}_d(r)}{\omega} \right) \psi_m(r_j) \right]$$

with

$$\mathcal{R}_{kj} = \sum_{j=0}^{N-1} \frac{e^{i(\omega-\omega_D^0-k\omega_b)t_j}\left[1-e^{i(\omega-\omega_D^0-k\omega_b)(t_{j+1}-t_j)}\right]}{1-e^{i(\omega-\omega_D^0-k\omega_b)\tau_b}} \tag{121}$$

$$C^t(r^0,\theta) = \frac{\omega-\hat{\omega}_*}{\omega-\omega_D^0-k\omega_b} J_0^2 = \sum_\nu C^t_\nu r^0 e^{i\nu\theta} \tag{122}$$

$$K_{kp\nu} = \frac{1}{2\pi}\int_{\theta^-}^{\theta^+} \frac{d\theta}{b(r,\theta)\sqrt{1-\frac{\Lambda}{b(r,\theta)}}} e^{-i\left[(nq(r^0)-p-\nu)\theta+W-k\omega_b\hat{t}\right]} \tag{123}$$

$$\hat{a}_{km} = \frac{1}{\tau_b} \int_{-\tau_b/2}^{\tau_b/2} d\hat{t}' e^{i\left[S_m^0 \theta' + W' + k\omega_b \hat{t}'\right]} \tag{124}$$

It should be noted that contrary to the perturbed potentials ϕ and ψ, the gyro-expression J_0 and the equilibrium quantities F_0, $\bar{\omega}_d$ and $\hat{\omega}_*$ are assumed to stay constant in the radial coordinate along a particle orbit.

4.4.3 Drifts in the GKM equation

In the GKM equation, an integral of the form

$$\int ie \frac{\mathbf{v}_d}{\omega} \cdot \nabla J_0 h d^3\mathbf{v} \tag{125}$$

has to be performed.
Also in the expression for h there is a term proportional to $\omega_d(r) \equiv \mathbf{v}_d / i \cdot \nabla$:

$$\left[\hat{a}_{km} \phi_m(r_j) - \left(\hat{a}_{km} - \frac{\hat{a}_{km}^G \bar{\omega}_d(r)}{\omega} \right) \psi_m(r_j) \right] \tag{126}$$

Of course, the drift operator entails radial derivatives of ψ and ϕ. In principle, these derivatives could be included is the system using a similar procedure as sketched in chapter 4.4.1 for J_0. But due to the smallness of $\dot{r}$ (one order of $\epsilon = a/R_0$ smaller) compared to $\dot{\theta}$ and $\dot{\varphi}$, ω_d is replaced by $\omega_D^0 = \dot{\varphi} - q(r^0)\dot{\theta}$. Finally, line (125) can be rewritten as:

$$\left(\int_{-\pi}^{\pi} \frac{d\theta}{2\pi} e^{ip\theta} \int ie_a \frac{\mathbf{v}_d}{\omega} \cdot \nabla J_0 h d^3\mathbf{v} \right)^{trap} = -\pi e_a^2 v_{th}^3 \sum_m \sum_j \int_{b_{min}(r)}^{b_{max}(r)} d\Lambda \int_0^\infty dY \sqrt{Y} \frac{\partial F_0}{\partial E} \sum_k \sum_\nu$$
$$\cdot \mathcal{R}_{kj} \cdot K_{kp\nu}^G \cdot C_\nu^t(r^0) \cdot \left[\hat{a}_{km} \phi_m(r_j) - \left(\hat{a}_{km} - \frac{\hat{a}_{km}^G \bar{\omega}_d(r)}{\omega} \right) \psi_m(r_j) \right] \tag{127}$$

$$\left(\int_{-\pi}^{\pi} \frac{d\theta}{2\pi} e^{ip\theta} \int ie_a \frac{\mathbf{v}_d}{\omega} \cdot \nabla J_0 h d^3\mathbf{v} \right)^{circ} = -\pi e_a^2 v_{th}^3 \sum_m \int_0^{b_{min}(r)} d\Lambda \int_0^\infty dY \sqrt{Y} \frac{\partial F_0}{\partial E} \sum_k \sum_\nu$$
$$\cdot K_{mkp\nu}^G \cdot C_\nu^c(r^0) \cdot \left[\hat{a}_{km} \phi_m(r) - \left(\hat{a}_{km} - \frac{\hat{a}_{km}^G \bar{\omega}_d(r)}{\omega} \right) \psi_m(r) \right] \tag{128}$$

Now our system of equations is complete consisting of the QN (77) and the GKM (81) equations together with the integrals (109), (121), (127) and (128).

5 Numerical Implementation

In this section we describe the structure of the numerical implementation and details of the methods involved.
For consistency, all FLR-effects at least up to second order are kept. In the GKM equation (72) the differential terms of fourth order in $k_\perp \varrho$ are dropped for simplicity. Their role has to be investigated in a later version of LIGKA.
As sketched in figure 10, we start from an equilibrium given analytically or numerically. At present, there exists an interface for the equilibrium code HELENA [48]. Also HAGIS [40],[41],a Monte-Carlo code in a guiding centre Hamiltonian formulation, usually applied for non-linear wave-particle interaction, can use HELENA equilibria as input. Before we start to run LIGKA itself we compute the integrals over the unperturbed particle orbits with HAGIS based on a certain equilibrium, i.e. we calculate for each m, p, k, r, Y and Λ the integrals a_{km}, K_{mpk}, K_{pk} and the corresponding a^G_{km}, K^G_{mpk}, K^G_{pk}. To be able to choose the points in velocity space in an advantageous way, i.e.more points near the trapped-passing boundary, a little piece of code is run, that calls HAGIS iteratively and thus provides a grid in velocity space on which the required integrals are calculated in a separate step.
The structure of LIGKA itself is the following one:

- Step 1: reading in or generating an equilibrium (5.1)
- Step 2: computing the coefficients originating from the differential operators of the GKM equation (5.2)
- Step 3: using Galerkin's method to set up algebraic equations (5.3)
- Step 4: reading in the kinetic data (5.4)
- Step 5: guessing an eigenvalue, evaluating the velocity space integrals and adding the result to the coefficients of the differential operators. (5.5)
- Step 6: solving for the eigenvalues of the total matrix (5.6)
- iterating step 5 and 6 till a converged solution is found

When kinetic effects are not needed, step 4 and 5 are skipped, which leads to a linear dependence on the eigenvalue. In this case, a simple matrix inversion delivers the complete spectrum.
Now the steps given above are documented in further detail:

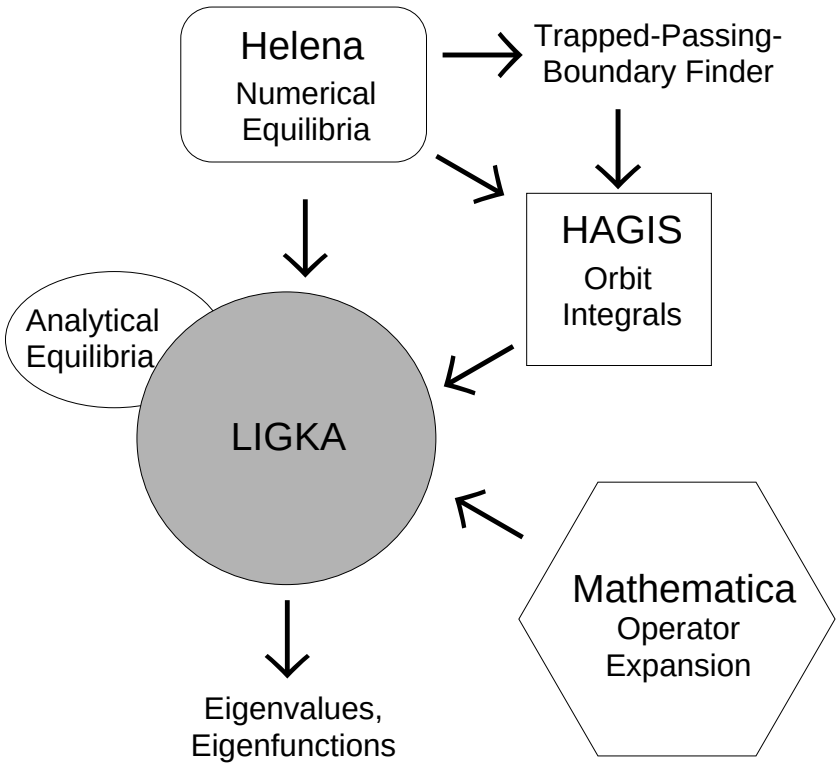

Figure 10: Survey of different codes involved

5.1 Equilibrium

In appendix 8.8 a short review is given about the underlying concept of MHD equilibria and the theoretical framework in the ideal MHD picture. Starting with the balance equation between pressure and Lorentz force and using Ampere's law, the Grad-Shafranov equation is derived. To profit from the existence of nested flux surfaces, as radial coordinate a flux label is chosen. The other two coordinates are chosen such that the field lines are straight and the toroidal coordinate coincides with the toroidal angle.
The equilibrium code HELENA [48] is employed to solve the Grad-Shafranov equation numerically and to write out the required profiles and coefficients. This information is then read in by LIGKA.
In order to provide an analytical description of plasma equilibria like in Qin's work, we examine the relation between general 2d geometries in flux coordinate representation and simpler configurations, namely straight circular Tokamak geometry and concentric circular Tokamak geometry.

5.2 Expansion of Differential Operators with Mathematica

To expand the complicated differential operators from the gyrokinetic moment equation (72) in the geometries from last section, we use an extension package for Mathematica (GeneralVectorAnalysis), developed by H. Qin ([1], Appendix). This package is a more general and efficient extension of the standard VectorAnalysis - package supplied by Wolfram Research. It uses a differential form representation of vector calculus and allows for completely general (user-defined) coordinate systems. Also small-parameter-expansions in the metric coefficients are possible.
Via this computer based analytical tool, all operators are expanded in different geometries. The results can be long and complicated, especially when the metric tensor is given in the most (for partially orthogonal coordinates) general form (244). However, the lengthy results can be easily converted to Fortran 90 code by some Unix script. After an optimised compilation, the read-in and evaluation time for these operators is completely negligible compared to other program steps.

5.3 Finite Element Method

After applying the projection operator $1/2\pi \int_0^{2\pi} e^{ip\theta}$, the system of coupled differential equations of second order in radial direction is written in the following form:

$$\begin{pmatrix} A_{pm}^{Q\phi} & A_{pm}^{Q\phi} \\ A_{pm}^{J\psi} & A_{pm}^{J\psi} \end{pmatrix} \begin{pmatrix} \phi_m'' \\ \psi_m'' \end{pmatrix} + \begin{pmatrix} B_{pm}^{Q\phi} & B_{pm}^{Q\phi} \\ B_{pm}^{J\psi} & B_{pm}^{J\psi} \end{pmatrix} \begin{pmatrix} \phi_m' \\ \psi_m' \end{pmatrix} + \begin{pmatrix} C_{pm}^{Q\phi} & C_{pm}^{Q\phi} \\ C_{pm}^{J\psi} & C_{pm}^{J\psi} \end{pmatrix} \begin{pmatrix} \phi_m \\ \psi_m \end{pmatrix} = 0 \tag{129}$$

To transform this system into an algebraic form, we expand $\phi_m(r)$ and $\psi_m(r)$ in finite elements. This method is commonly used and for example described in [46],[47]. As first step we introduce a partition in radial direction, consisting of $N+1$ points, including start and end points. This partition in general can be non-equidistant, but in the present version of LIGKA only an equidistant mesh is implemented. Consequently, for $N+1$ points, we have N finite elements. In each element the unknown function is approximated by cubic Hermite polynomials, whose coefficients are determined by four values: the value of the function itself and its first derivative on both sides of the finite element. If we set up a vector consisting of these four values and multiply with the Hermite basis functions

$$\{1 - \frac{3x^2}{l^2} + \frac{2x^3}{l^3}, x - \frac{2x^2}{l} + \frac{x^3}{l^2}, \frac{3x^2}{l^2} - \frac{2x^3}{l^3}, \frac{x^3}{l^2} - \frac{x^2}{l}\}, \tag{130}$$

we obtain the solution in form of third order polynomial on a chosen finite element of length l. We postulate the function and its first derivative to be continuous: thus we end

up with $4N - 2(N-1) = 2N + 2$ unknowns. For the unique solution of a second order differential equation one has to choose two constants that in our case are given through the boundary conditions at the plasma centre and the plasma edge. So the number of unknowns reduces to $2N$. For the whole system with two equations and M poloidal harmonics, we obtain a $2N \cdot 2 \cdot M \times 2N \cdot 2 \cdot M$ matrix. To set up this matrix, we choose Galerkin's method: we approximate the solution by

$$\phi_m(r) = \sum_{j=1}^{N} \phi_{mj}\varphi_j(x), \quad \psi_m(r) = \sum_{j=1}^{N} \psi_{mj}\varphi_j(x), \tag{131}$$

put this expansion into the differential equation and minimise the residual R weighted with the same expansion functions, i.e. Hermite polynomials (here given just for ϕ):

$$\int_{plasma} dx R(x)\varphi_k(x) = 0 \tag{132}$$

with

$$R = A_{pm}[\sum_{j=1}^{N} \phi_{mj}\varphi_j(x)]'' + B_{pm}[\sum_{j=1}^{N} \phi_{mj}\varphi_j(x)]' + C_{pm}\sum_{j=1}^{N} \phi_{mj}\varphi_j(x). \tag{133}$$

Note the difference between ϕ_m and ϕ_{mj}: the first one stands for the potential itself, the latter for the expansion coefficients in the chosen basis. This expansion leads to a banded structure of the matrix, as indicated in figure 11.

Since also the coefficients A_{pm}, B_{pm} and C_{pm} depend on x, one could think of expanding them in the same way as ϕ_m and ψ_m. Then the integrations in equation (132) can be carried out completely analytical, because only third order polynomials have to be integrated. However, this approach requires that the derivatives of A_{pm}, B_{pm} and C_{pm} are known sufficiently accurate. In practise, where the coefficients are given non-analytically (on a grid), and the derivatives have to be calculated with some numerical method, this leads to poor convergence (see figure 12).

Instead, we carry out the integrals numerically: cubic splines are employed for the interpolation of A_{pm}, B_{pm}, C_{pm}, and a Gauss-21-point rule (nag_quad_1d_gen) for integration. This procedure results in a convergence rate $\propto l^4 - l^5$ (see figure 13), which was e.g. also found in [48].

As boundary conditions we impose that the perturbed potentials for all poloidal harmonics vanish at the the plasma centre and at the outermost flux surface. This is introduced in the system by deleting the first column and the first row as well as the last-but-one column and row for each m-block (see figure 11).

The finite element implementation is tested for a pure MHD case (chapter 6.1.2): since

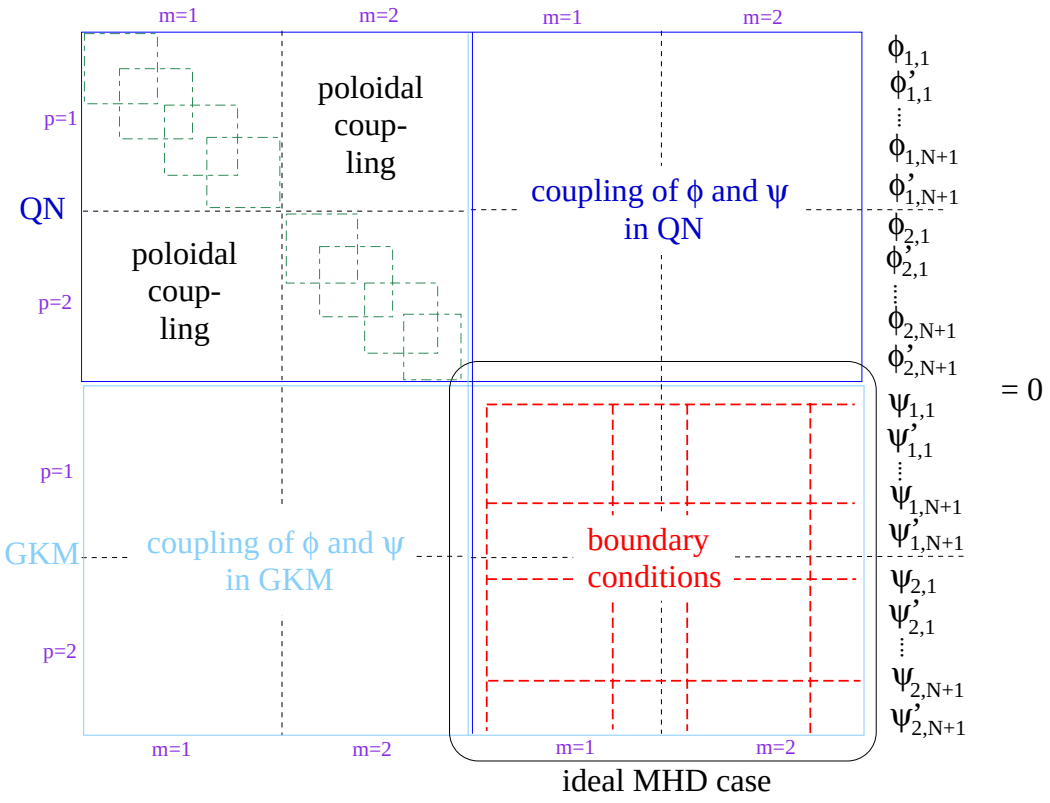

Figure 11: graphical representation of the complete system for two coupled poloidal modes

there $\phi = \psi$, only one equation for one unknown potential has to be solved. Furthermore, this equation is then linear in the eigenvalue:

$$M\phi_{mj} + \lambda M_\lambda \phi_{m,j} = 0 \quad \rightarrow \quad M_\lambda^{-1} M\phi_{mj} + \lambda I \phi_{mj} = 0 \tag{134}$$

We use a standard NAG routine (nag_nsym_eig_all) to solve for the eigenvalues and eigenfunctions. For 100 finite elements and one poloidal mode (straight tokamak case) the total time for setting up the matrix and solving it is approx. 10 seconds on a single processor of a 600 MHz Linux machine.

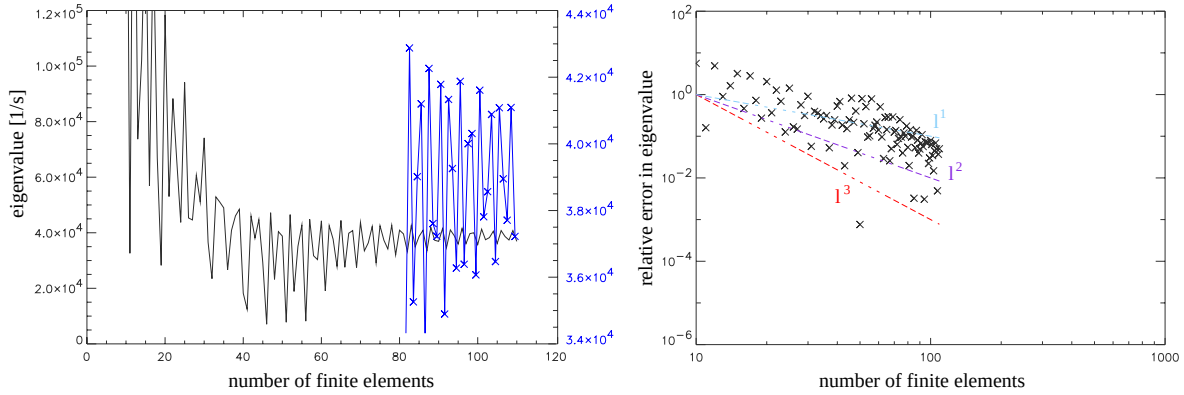

Figure 12: Convergence rates of the growth rate and its relative error for an unstable internal kink mode: here the coefficients A_{pm}, B_{pm} and C_{pm} are also expanded in Hermite polynomials and the finite element integration is carried out analytically. The poor convergence is due to the error of the first derivatives of the coefficients calculated with a Nag spline routine.

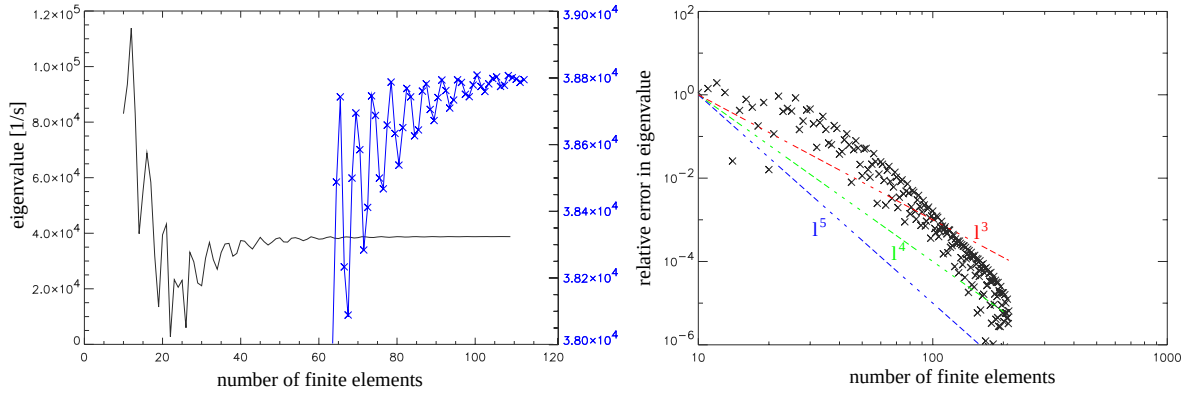

Figure 13: Numerical integration of the finite element integrals leads to much better convergence. The slower convergence for low N- numbers is due to the structure of the mode, i.e. the step-function-like behaviour at the $q = 1$ surface.

5.4 Calculating Kinetic Data

Due to various drift effects caused by curvature and inhomogeneity of the equilibrium magnetic field the particle orbits can be classified into two main types:

- Trapped particles lack a sufficient high parallel energy to penetrate into the high field region and are consequently caught on the outer side of a tokamak. They experience two reflections per orbit and the bounce-time between these mirror points becomes infinitely long when a particle just hits the tapped-passing boundary.

- Passing particles have enough parallel energy to follow the helical field lines. Since the drift for particles travelling in the direction of the current is the same as for particles with opposite orientation, one has to distinguish between co- and counter passing particles.

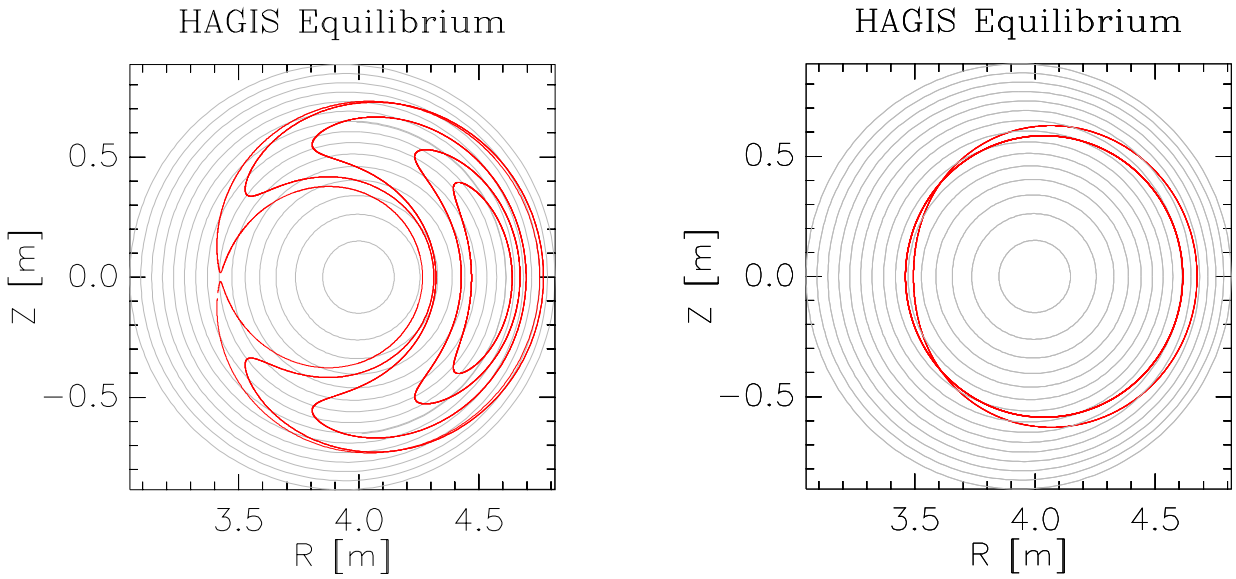

Figure 14: Poloidal projections of different orbits for a 3.5 MeV α-particle with an average radial position $s = 0.7$: on the left a selection of trapped orbits, on the right the two most extreme (i.e. $\lambda = 1$ and $\lambda \approx \lambda_c$) passing orbits, generated by HAGIS and the TPB-Finder (chapter 5.4.1)

Besides these standard particle orbits, as shown in figure 14, there are also more exotic orbits like pinch (when an electrical field is added) or potato orbits (figure 15) that can play an important role, especially for α-particles. A detailed overview of these different regimes is given in [56] or [40].

Although there are useful analytical approximations for particle orbits, general equilibrium geometry and broad banana orbits require a numerical treatment. For this task, we use a code developed by S.D. Pinches, called HAGIS [40], [41]. HAGIS employs a Hamiltonian guiding centre description for the particle motion in an electromagnetic field, that is represented by superposition of a background axisymmetric magnetic equilibrium field (supplied by a various equilibrium codes including also HELENA) and an electromagnetic perturbation, calculated by an MHD stability code. It evolves the particle distribution in time and accounts for nonlinear particle-wave interaction.

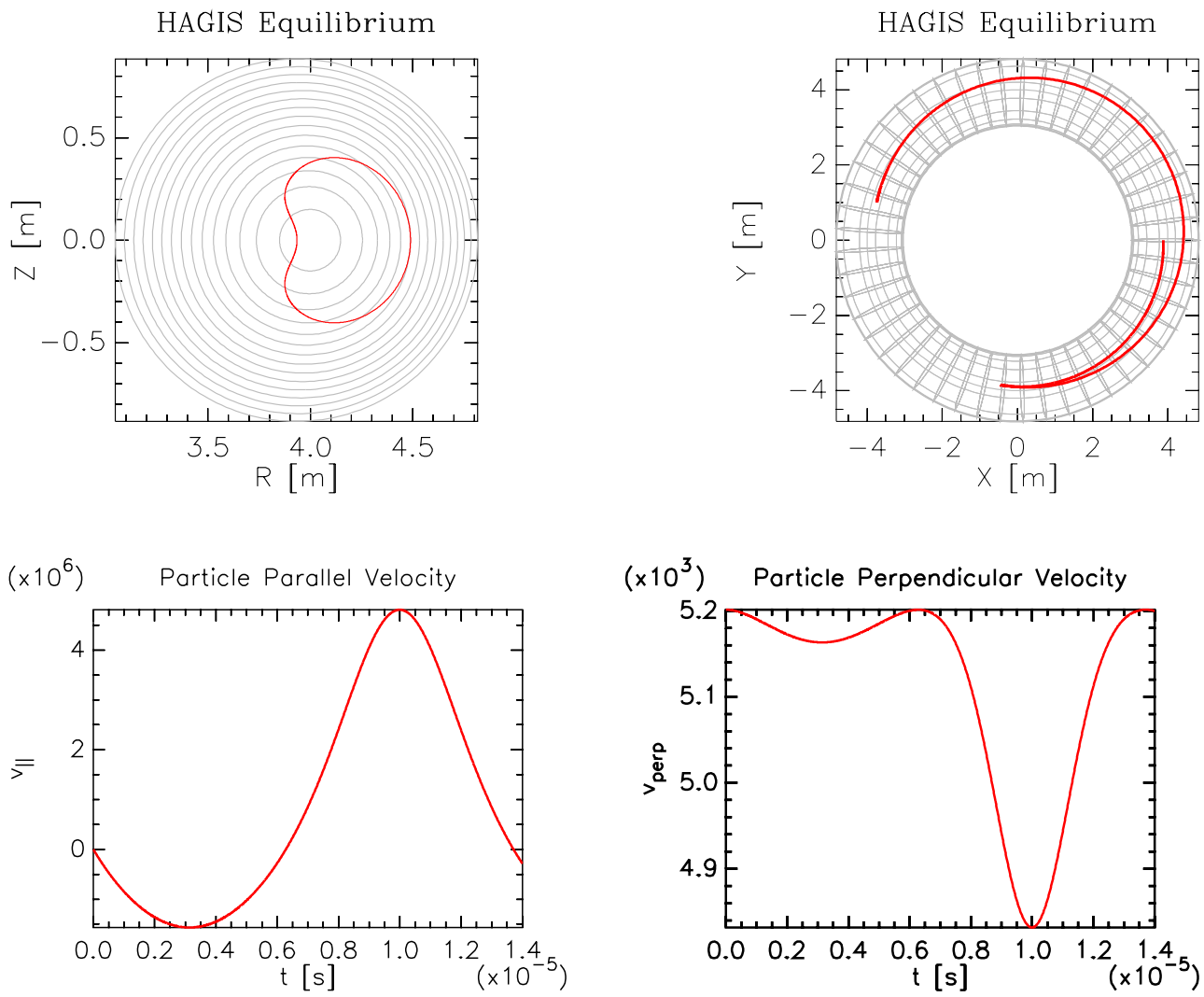

Figure 15: At high energies, the drifts are so large that particles close to the axis travel on potato-like orbits - here for a 3.5 MeV particle with an average orbit of $s = 0.4$ and $\Lambda = 0.96938$. Although the poloidal projection of the orbit (up left) looks like a passing one, $v_{\|}$ changes sign. Thus the particle is toroidally trapped.

For our purposes, i.e. for finding the trapped-passing boundary and for calculating orbit integrals along the unperturbed path, the wave interaction part is turned off.

5.4.1 Trapped-Passing-Boundary Finder (TPB-Finder)

As can be seen in figure 16, there is a discontinuity λ_c in the in the pitch angle - energy plane, that has to be resolved in an adequate way. For this purpose a little code was

developed that determines the trapped- passing boundary: starting from an analytical guess, 10 particles with a constant energy are iteratively loaded into the Λ-discontinuity. Clearly, this improves the resolution by one order of magnitude at each step.
This simple scheme is complicated by the following requirement: to import kinetic data into LIGKA, it has to be given on the same radial grid as used in LIGKA. I.e., for a certain grid point r_i we have to find all that particles, whose radial position averaged over its orbit is r_i. Only then it is guaranteed that the calculated quantities are smooth enough to be used in the velocity space integration.

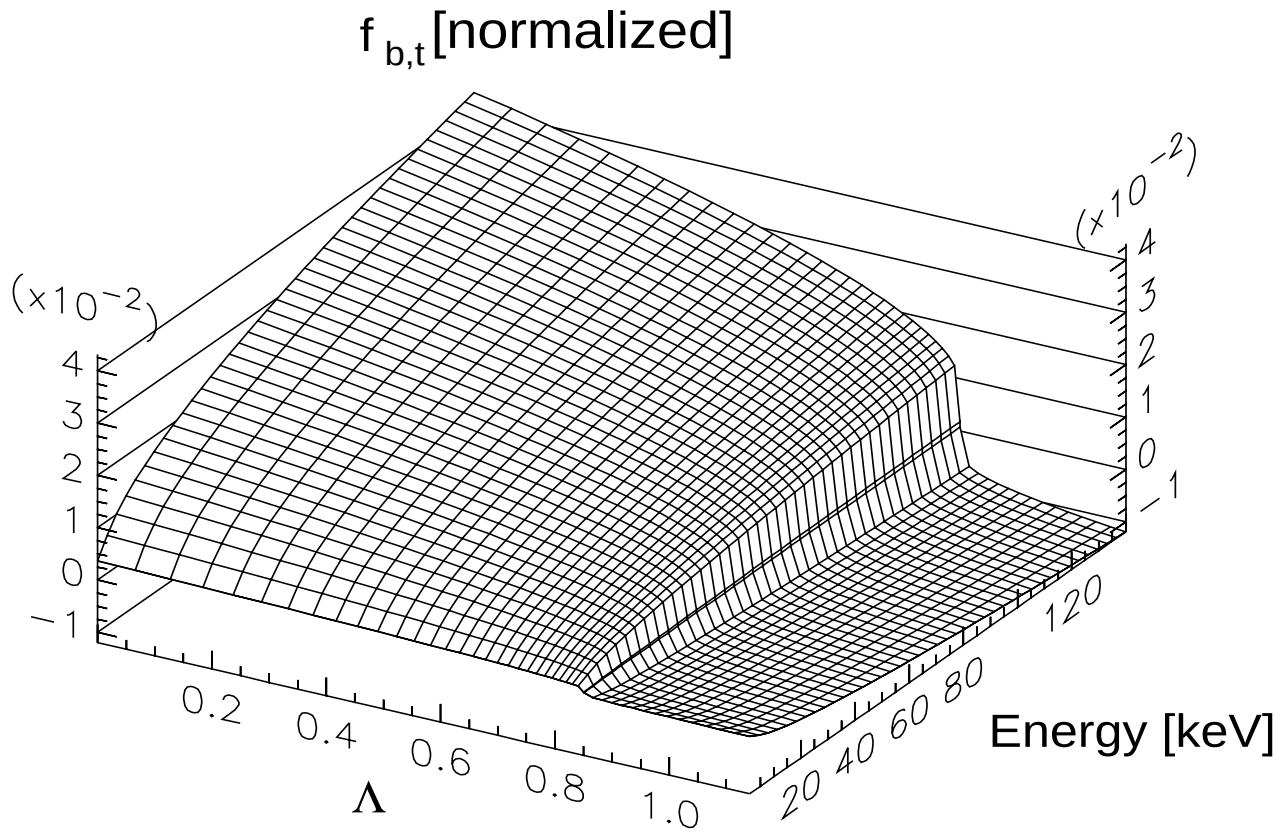

Figure 16: $f_{b,t}$ for hydrogen ions, normalised to the Alfvén frequency. The trapped frequencies were given a negative sign to ensure smooth splines

Consequently there has to be performed an 'optimisation' resp. 'refinement' for two quantities: pitch angle and averaged radial orbit position. Fortunately, there is one fact that helps to create appropriate 'shifting'-rules: if a trapped particle is moved in positive radial direction, i.e. in the lower field region, and its pitch angle and energy are kept constant, it will not change into a passing particle, since the maximum magnetic field on the shifted

path is certainly higher. The opposite rule is true for circulating particles.
Trapped particles are launched at their mirror points, i.e. at the tip of the banana [42]. This trick speeds up the radial optimisation considerably, because the particle spends most of the bounce time near the mirror points whose radial position consequently is usually close to the particle's average radial position. Of course, this procedure fails whenever non standard orbits are involved. That's why for particles with high energy near the axis different rules and procedures have to be used.
Another issue would be particle losses. But since the inclusion of this phenomenon would complicate the problem substantially, it is not taken into account in this work.

For a prescribed accuracy of $\lambda_{\text{trapped}} - \lambda_{\text{passing}} < 0.002$ and $r_0 - \langle r \rangle < 0.01$ approximately 15 iterations are required.
After the discontinuity is well known, the final grid on which the integrations are performed is set up where the λ-grid-points are accumulated exponentially around λ_c. Usually 20 points in λ and 15 points in energy are sufficient, to ensure smooth splines in LIGKA. As an example, $f_{b,t}$, calculated by the methods described above, is shown in figure 16.

5.4.2 Particle Orbit Integrals

Once the grid is set up, the quantities a_{km}, K_{mpk} , K_{pk} and the corresponding a^G_{km}, K^G_{mpk}, K^G_{pk} are computed. The particle is followed twice around its orbit: on the first orbit, the average quantities $\omega_{b,t}$ and ω^0_D needed for the propagator are determined. On the second orbit the integration is carried out, using a trapezoidal rule. The time step is chosen such that the relative error is less then 10^{-3}, which can easily be checked by integrating simple functions like constants or $\sin(\theta)$. The results will be discussed in chapter 6.2.
To be able to implement the trapped-particle-integration scheme derived in section 4.4.2, the time point when a particle changes from one radial bin in the neighbouring one has to be known. This information is also written out on the second orbit.

5.5 Velocity Space Integrals

After the orbit integral information is calculated with HAGIS and read in by LIGKA, the integration over the velocity space can be carried out. Since all the 'input' quantities exhibit a smooth behaviour (see 2d plots in the result section), they can be splined without numerical dangers allowing in principle an arbitrary number of integrations points.
Clearly, the resonance denominator makes the energy-pitch-angle-integration difficult:

$$\frac{1}{\omega - \omega_D - k\omega_b} \quad \text{resp.} \quad \frac{1}{\omega^2 - (S_m^0 + k)^2\omega_t^2} \tag{135}$$

If ω is pure real then the denominator can become exactly zero. In that case the principal value integral is calculated with a numerical library routine from the CERNLIB [62]. This routine also calculates the imaginary residual, which is then the source of the kinetic damping in the system.

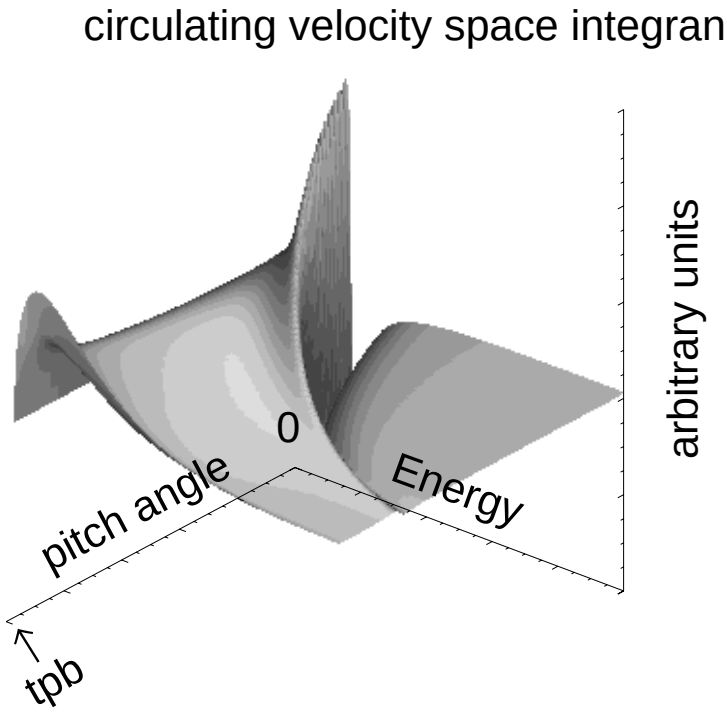

Figure 17: An example for the circulating part of the velocity space integrand for $\omega_r/\gamma \sim 150$ which is a typical ratio for an unstable TAE mode, $m = p = 3$, $k = 0$

For complex ω, real and imaginary parts are integrated separately. One has to make sure that for smaller Im[ω], a bigger number of integration points has to be chosen. Ideal for this kind of problem would be an adaptive-grid-integration method (as used for a similar problem in [56]). Here, so far, only a standard-Gauss-technique is applied, which should be changed in the future. To check the validity of the present scheme, a convergence test has been carried out: with k ranging from -5 to 5, the kinetic contribution to the the electromagnetic part of the GKM moment equation is calculated with different resolutions

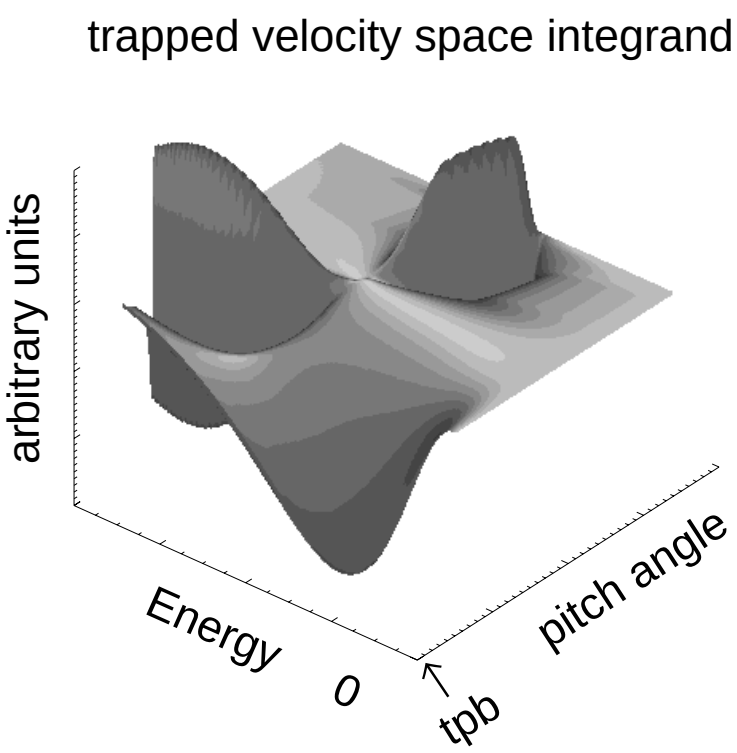

Figure 18: An example for the trapped part of the velocity space integrand for $\omega_r/\gamma \sim 150$ which is a typical ratio for an unstable TAE mode; here ω_D separates the resonance region into two parts, $m = p = 3$, $k = 1$

in the Λ-energy-plane (figure 19). There are two 'extreme' cases considered: if there is one dominant contribution for a single k-value, which often means that the resonance lies in the 'flat' region of the integrand i.e. not near or in the TP-boundary (as shown in figures 17, 18), then the requirements on the resolution are moderate: already a 40×40 grid gives an error less than 5%. In contrast, when there are many small contributions including resonances near the TP-boundary (what happens quite often, since there $\omega_{b,t}$ becomes very small and ω_D-resonances can occur), the effort has to be more than doubled to stay under the 5% margin. This problem has also been pointed out in [50]. But since the contributions from this second case are usually one order of magnitude smaller than those from the first case, a bigger error can be accepted. Nevertheless, a detailed investigation (benchmarking with CAS3d-K) of this problem is planned in the next future.
As a compromise - justified by figure 19 - in this work usually $(50 - 70)^2$-grid points are chosen.
To estimate the CPU time needed, one has to count the number of integrals that have to

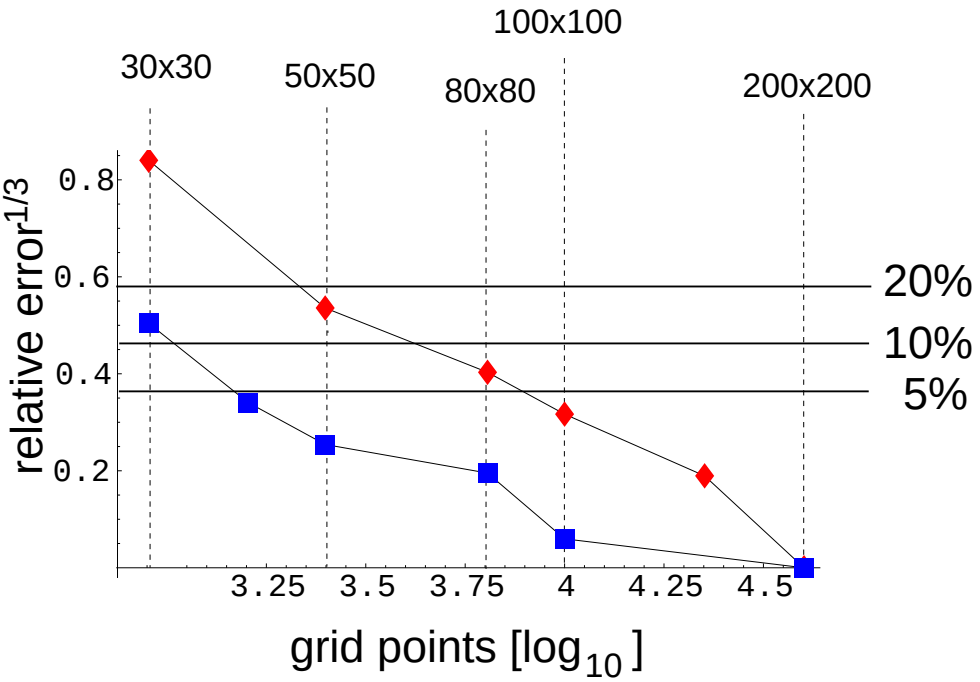

Figure 19: relative error as function of the number of grid points (logarithmic) in the Λ-energy plane : the blue dots refer to a simpler integrand, the red dots to more complicated one (details in the text)

be performed for each guess of ω: for 100 radial grid points, 5 harmonics ($p \times m = 25$), two equations (QN+GKM), two variables (ϕ and ψ), 2×2 (complex, circulating-trapped) and 3 species, 120000 integrations have to be carried out. For a 50×50 grid, a typical $\sim$ 1GHz machine can achieve $\sim$ 25 integrations per second. On a 20 node cluster this translates into a total integration time of 4 minutes.

5.6 Eigenvalue Solver

Due to the presence of the eigenvalue within the kinetic integrals, the total problem is now no longer linear in the eigenvalue. That means, that matrix inversion techniques can no longer be applied to determine ω. Instead, one has to look for the roots of the characteristic polynomial:

$$\mathcal{P}(\omega) = \mathrm{Det}|M| \tag{136}$$

Since $\mathcal{P}(\omega)$ depends on ω in very complicated way, it turns out to be too hard to find the roots of $\mathcal{P}(\omega)$ directly. Therefore a more efficient algorithm [63] was implemented: according to its definition, $\mathcal{P}(\omega)$ can be written a product of the eigenvalues $e_i(\omega)$ of

M. Clearly, if an ω is found for which $e_i(\omega) = 0$, then also $\mathcal{P}(\omega) = 0$. Using this idea we start with an initial guess, determine the eigenvalues of the matrix and minimise the smallest $e_i(\omega)$ iteratively, applying Newton's method. Depending on the initial guess (often obtained from a pure MHD calculation), about 10-20 steps are required. The eigenvalues are determined with the NAG routine (nag_nsym_eig_all). For a matrix with the dimensions $(5 \times 100 \times 2 \times 2 = 2000)^2$ this takes about 8 minutes of CPU time on a $\sim$ 1GHz machine.

6 Results

6.1 MHD Test Cases

6.1.1 Cylinder Geometry

The shear Alfvén mode is one possible solution, $\omega^2 = k_\parallel^2 v_A^2$, of the dispersion relation which, for a homogenous plasma, is given by:

$$(\omega^2 - k_\parallel^2 v_A^2)[\omega^4 - (v_s^2 + v_A^2)k^2\omega^2 + (kk_\parallel v_s v_A)^2] = 0 \tag{137}$$

where $v_A = \sqrt{B_0^2/\mu_0 n_0 m}$ is the Alfvén speed and $v_s = \sqrt{\gamma P/n_0 m}$ the sound speed. Some of its physical properties were discussed in chapter 3.3. As a first simple test for LIGKA, various Alfvén spectra in cylindrical geometry were reproduced:

- For a homogenous plasma without currents, the spectrum is infinitely degenerate [33] and the eigenvalue only depends on the parameter $k_\parallel = -n/R_0$ (with n the 'toroidal' mode number and R_0 the length of the plasma column). For $k_\parallel = -0.5$, $\omega^2/v_A^2 = 0.25$ is reproduced.

- For an inhomogeneous plasma with a density that drops to 0 at the boundary, the spectrum changes into a continuous one with the range from k to infinity. Of course, the number of eigenmodes calculated numerically is restricted to the number of finite elements. Changing this number shows that the results fulfil the requirements for continuous modes represented by discrete numerics, as defined in ([33], p. 71)

- For an inhomogeneous plasma with a density that drops to a nonzero value at the boundary, the continuum is bounded by an upper value. For example, choosing the density profile $n(r) = n(0) \cdot (1 - \epsilon r^2), \quad \epsilon > 0$, the spectrum is bounded by $k_\parallel^2 \geq \omega^2 \geq k_\parallel^2/(1-\epsilon)$. Figure 20 shows the results for $B_z = 1, \quad \epsilon = 0.25, \quad k_\parallel = -0.5, \quad \Rightarrow \quad 0.25 \geq \omega^2 \geq 0.33$

- Adding a current along the symmetry axis can cause unstable modes: if the total current is not too high - to avoid external kink modes - and its radial profile is chosen properly, the weak internal kink mode appears: using the energy principle, one can show that for $m = 1$ the mode is unstable to $\mathcal{O}(\epsilon^2)$ if $q_0 < 1/n$. The ideal MHD growth rate can be calculated analytically with the well known formula ([35],[37]), derived from the energy principle:

$$\gamma \approx \frac{-\pi}{\sqrt{2\varrho\mu_0}|(\mathbf{k}\cdot\mathbf{B})'|_{r_s} r_s^3} \int_0^{r_s} dr g \tag{138}$$

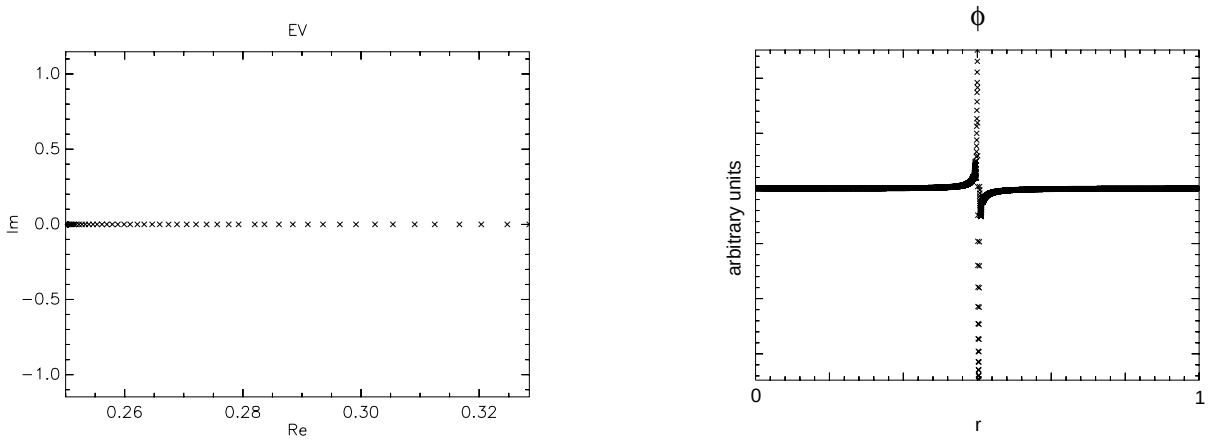

Figure 20: Alfvén Eigenvalue spectrum for an inhomogeneous cylindrical plasma

with

$$g = \frac{B_\theta^2 k^2 r^2}{\mu r}\Big[3(nq-1)^2 + 4(nq-1) + \frac{2\mu_0 r}{B_\theta^2}\frac{dp}{dr}\Big]$$

As a numerical test, 'Case F' from Gruber's book [33] p.53 is reproduced: for a q-profile $q(r) = (1 + c_2^2 r^2)/c_1$ with $c_1 = 2/7$, $c_2 = 10/7$, $m = 1$, $k = -0.2$, $B_z = 1$, $n(r) = 1$ together with the appropriate pressure profile

$$p(r) = \frac{c_1^2}{2c_2^2}\Big[\frac{1}{(1+c_2^2 r^2)^2} - \frac{1}{(1+c_2^2)^2}\Big]$$

one calculates a squared growth rate (normalised to the square of the Alfvén velocity) of $-5.7 \cdot 10^{-5}$ (Gruber: $-5.9 \cdot 10^{-5}$) as the most unstable mode. The remaining difference might be due to the different physical formulations: ideal MHD solves equations for a fluid element ξ whereas LIGKA solves for the electrostatic potential.

6.1.2 Straight Tokamak Geometry

By defining $k = -n/R_0$ and $B_\theta = rB_0/R_0 q(r)$ one can introduce a toroidal periodicity, but still keeping all poloidal harmonics decoupled. In this geometry, Qin's example ([1], p. 155) is reproduced: for the q- profile together with the appropriate pressure profile

$$q(r) = \frac{q_a r^2}{1-(1-r^2)^{q_a/q_0}}; \qquad -\mu_0 p'(r) = \frac{B_z^2 r[2q(r) - rq'(r)]}{R_0^2 q(r)^3}$$

and the parameters $q_0 = 0.416$, $q_a = 2.5$, $m = 1$, $B_0 = 4.605\ T$, $R_0 = 2.45\ m$, $a = 0.245\ m$, $n(r) = 4.65 \cdot 10^{19}/m^3$, the calculated growth rate, $4.122 \cdot 10^4/s$, is very close to the ideal MHD result for a straight tokamak according to formula (138): $4.552 \cdot 10^4/s$. It also agrees

reasonably with Qin's result $3.717 \cdot 10^4/s$. The eigenfunction and the corresponding q-profile are shown in figure 21. The minor deviation of LIGKA from KIN2DEM might be due to the different radial discretisation (cubic Hermite polynomials vs. cubic-B-splines).

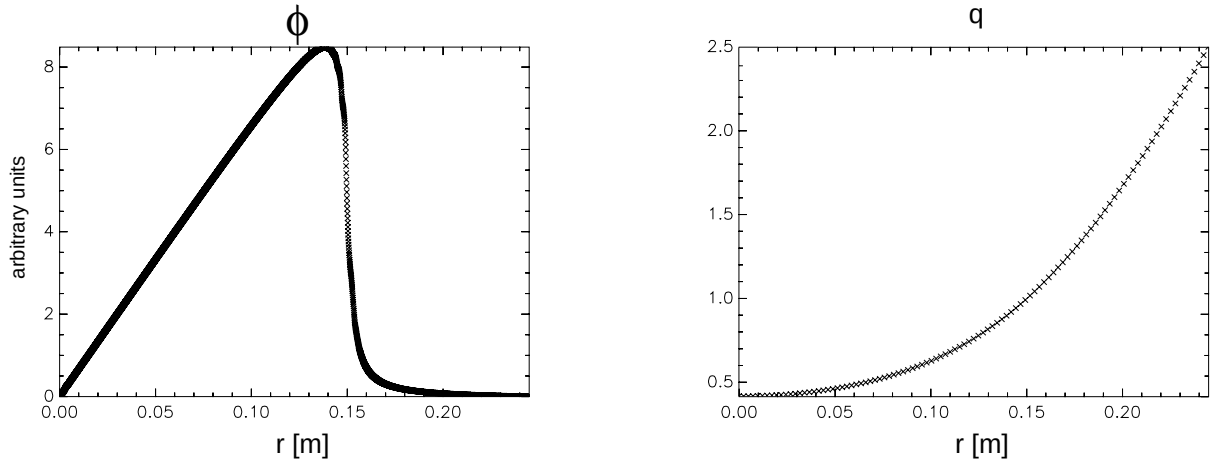

Figure 21: Internal kink mode: eigenfunction and q-profile for 100 radial grid points

6.1.3 Toroidal Geometry

A detailed δW analysis ([38],[1]) shows that in toroidal geometry, the $m = 2$ component (that in straight tokamak geometry is stable for $n = 1$) couples to the $m = 1$ component to $\mathcal{O}(\epsilon)$ and thus provides a stabilising influence on it.
To demonstrate this, a series of equilibria is chosen where q_0 is varied. The dependence of γ on q_0 can be explained as follows: if q_0 increases the location of the $q = 1$-surface (r_s) moves closer to the axis i.e. the plasma part inside r_s becomes more and more similar to a straight tokamak or in other words, the poloidal coupling decreases. Consequently the growth rate increases. On the other hand the mode becomes stable for $q_0 \to 1$ because this resonant surface moves out of the plasma. Combining these two effects, a γ versus q_0 diagram shows a maximum before q_0 approaches 1.
For an equilibrium with the parameters $B_0 = 4.605T$, $R_0 = 2.45m$, $a = 0.245m$, $n_0 = 4.65 \cdot 10^{19}/m^3$ and the profiles given in figure 22 a q_0-scan has been carried out with LIGKA and compared with KIN2DEM. The eigenfunctions, which agree very well with Qin's results [1], are shown in figure 23. Figure 24 shows a relatively good agreement between both codes for $q_0 < 0.95$. When the resonant surface comes close to the axis, the differences grow: since the stability of an internal kink mode in toroidal geometry is of order $\mathcal{O}(\epsilon^4)$ (which can be shown in a detailed δW analysis [1]), already minor deviations

of the profiles near the axis can lead to major changes in the growth rate. To resolve these differences, a more detailed benchmark would be necessary.

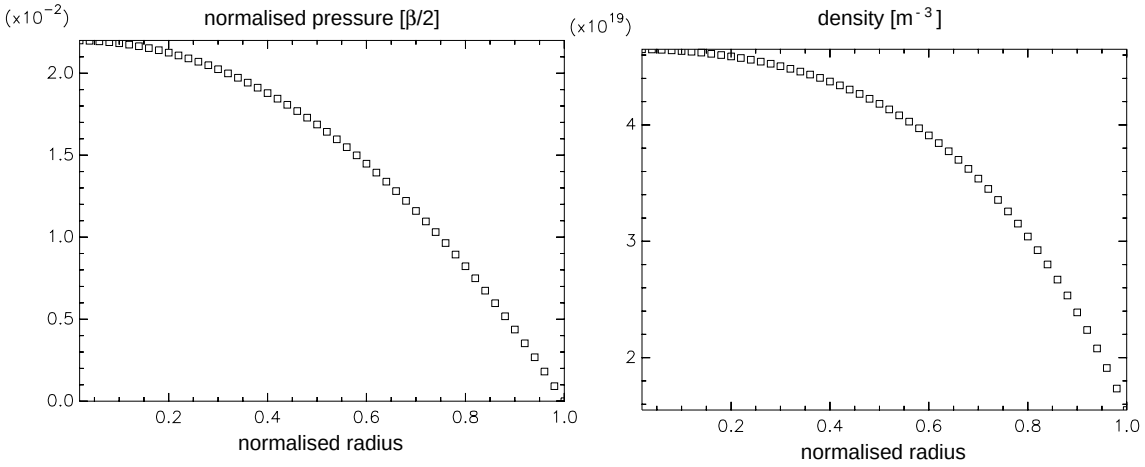

Figure 22: normalised pressure (left) and density profiles

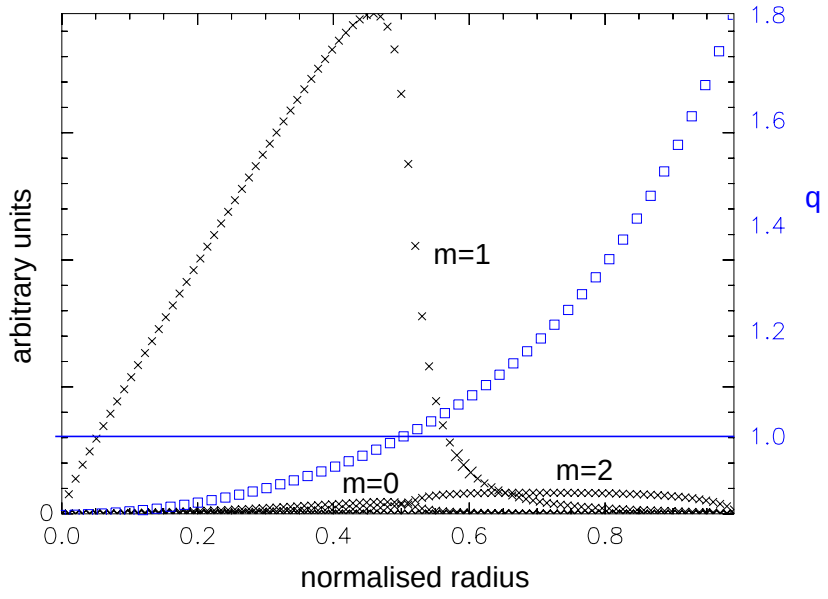

Figure 23: Equilibrium q-profile and eigenfunctions of the internal kink mode calculated with LIGKA

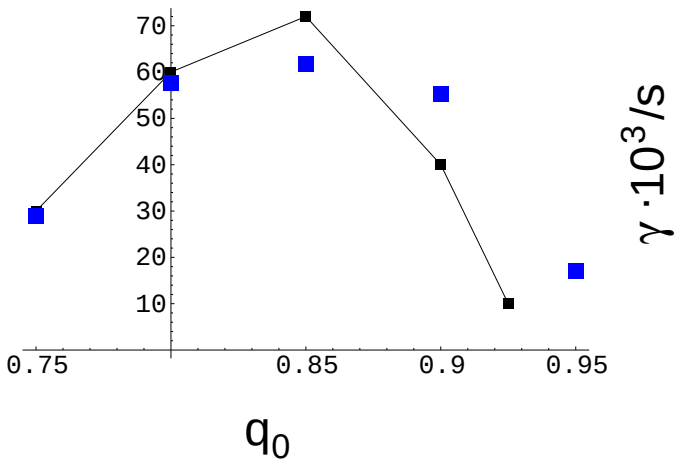

Figure 24: q_0-dependence of the growth rate of an internal kink mode: KIN2DEM results (black line) and LIGKA results (blue squares)

6.2 Orbit Integral Results

The next step is to ensure that the kinetic contributions to the matrix are set up correctly. It is also examined under which conditions the analytical formulae in the circular concentric geometry limit are applicable.

6.2.1 Bounce and Drift Frequency

For $\omega_{b,t}$ and ω_D the following expressions can be derived from equation (116):

$$\tau_b = \frac{4R_0 q(r_0)}{\sqrt{Y} v_{th}} \int_0^{\theta_0} \frac{d\theta}{b(r_0,\theta)\sqrt{1-\frac{\Lambda}{b(r_0,\theta)}}} = \frac{2\pi}{\omega_b} = \frac{1}{f_b} \tag{139}$$

$$\tau_t = \frac{2R_0 q(r_0)}{\sqrt{Y} v_{th}} \int_0^{\pi} \frac{d\theta}{b(r_0,\theta)\sqrt{1-\frac{\Lambda}{b(r_0,\theta)}}} = \frac{2\pi}{\omega_t} = \frac{1}{f_t} \tag{140}$$

with r_0 as averaged radial position of the particle and

$$\theta_0 = \arccos(\frac{\Lambda - 1}{\epsilon_0}), \quad b(r_0,\theta) = 1 + \epsilon_0 \cos(\theta), \quad \epsilon_0 = r_0/R_0. \tag{141}$$

Clearly, these expressions neglect radial drifts along the orbits. For comparison with numerical values, we choose a numerical equilibrium with circular (but shifted) flux surfaces (I) and another one with an ellipticity of 1.6 (II). Detailed information on these equilibria can be found in appendix (8.8.4).

In order to obtain smooth splines near and at the trapped-passing boundary, in the following figures $-f_b$ is plotted rather than f_b itself [42]. This trick works also for 2d splines

(Λ, energy), as demonstrated in figure 16.
Figures 25 and 26 show that the agreement for $f_{b,t}$ between the analytic formulae and the numerical solution is very good, even for highly energetic α -particles that have large drifts. To understand this agreement, we have to examine a particle's orbit and its velocity on this orbit (figure 27): the particle's higher velocity on the outer side of the banana orbit (the particle runs down a bigger 'magnetic hill' than on the inner orbit part) is compensated by the longer distance it has to cover, such that already the times on inner and outer orbit are relatively close to each other. Their mean value then must be very close to a 'middle' orbit without any radial drifts, as described by the analytical formula for $f_{b,t}$.
Also the elliptic-case-values match reasonably well, although one starts to see minor deviations. Clearly, these deviations would grow, if a non up-down symmetric case would be considered.

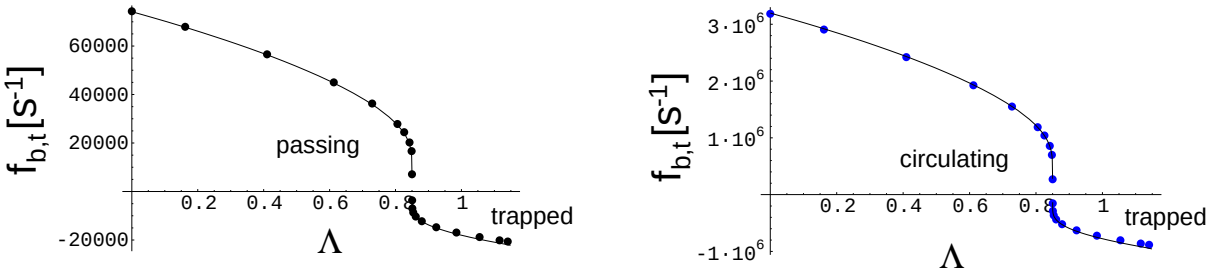

Figure 25: Circulating/bounce frequency for 28 keV ions (left,dots) and electrons (right,dots) for a numerical, but still circular equilibrium (I), compared to the analytical formulae (139,140, solid line)

For $\omega_D = \dot{\varphi} - q(r_0)\dot{\theta}$, we compare with the following analytical approximation ([18],[1]), again assuming circular, concentric, unshifted flux surfaces:

$$\omega_D = \frac{nq(r_0)E}{e_a B(r_0) R_0 r_0} G(\theta) \tag{142}$$

with

$$G(\theta)_{circ} = (1 + \frac{U^2}{v^2}\cos\theta + 2\frac{q'(r_0)r_0}{q(r_0)\epsilon_0}\frac{U(U-U_0)}{v^2}) \tag{143}$$

For trapped particles, setting $U_0 = 0$, leads to

$$G(\theta)_{trapped} = (2 - \frac{\Lambda}{b})\cos\theta + 2\frac{q' r_0}{q\epsilon_0}(1 - \frac{\Lambda}{b}), \tag{144}$$

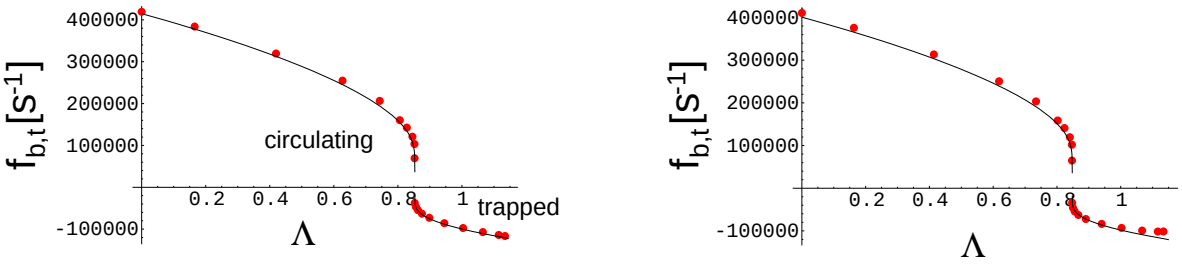

Figure 26: Circulating/bounce frequency for 3.5 MeV alpha particles for a numerical circular (I) equilibrium (left,dots) and an elliptical (II) one (right,dots), compared to the analytical formulae (139,140, solid line)

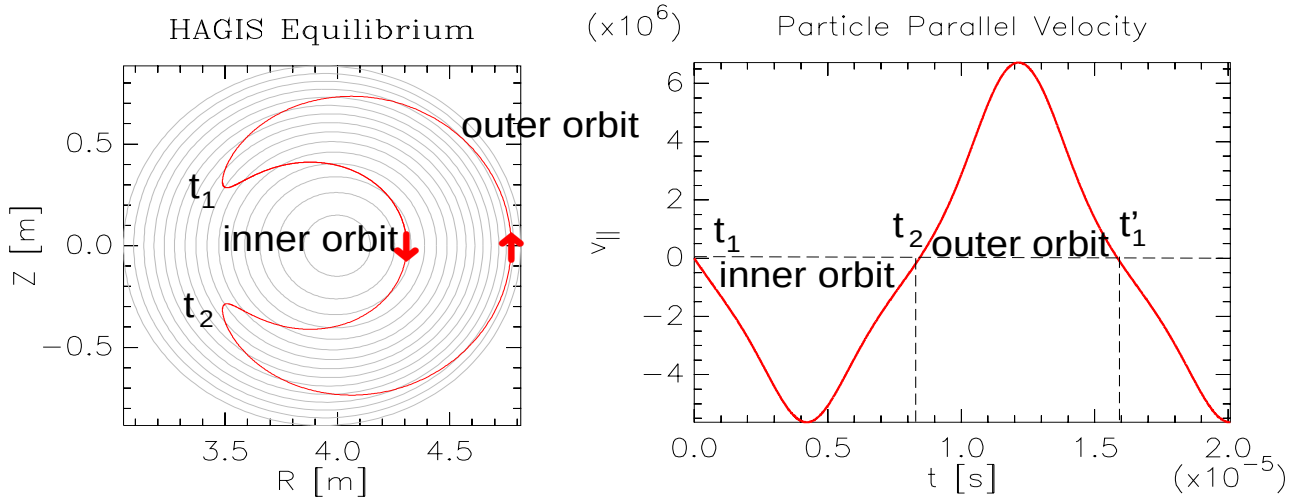

Figure 27: α-particle orbit (left) for equilibrium (I) with E=3.5 MeV and $\Lambda = 0.875$ and its parallel velocity (right): the times between the mirror points t_1 and t_2 resp.t_2 and t_1' are almost equal although the inner and outer orbit trajectory is completely different.

for circulating particles with $U_0 = R_0 q \omega_t$ one obtains:

$$G(\theta)_{circ} = G(\theta)_{trapped} - 2\frac{q' r_0}{q\epsilon_0} R_0 q \omega_t \frac{\sqrt{1 - \frac{\Lambda}{b}}}{v} \tag{145}$$

The comparison for the trapped case (figure 28) shows that even for electrons there are substantial deviations from the analytical formulae due to the Shafranov shift: although electrons undergo almost no radial drifts, i.e. they do not leave their flux surfaces, they feel, for increasing θ-values, a smaller magnetic field than the unshifted analytical equilibrium assumes. This results in an increasing offset for increasing θ. For α-particles, we see the same offset effect as for the electrons combined with a substantial difference of the

drifts on the inner and outer trajectory part.

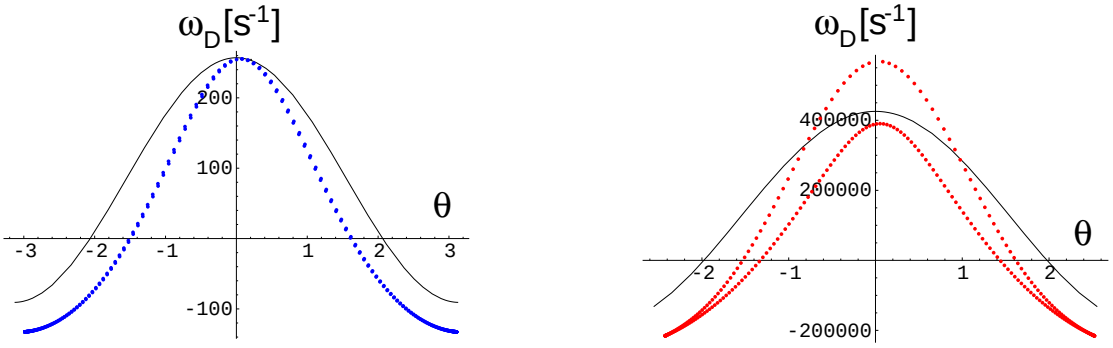

Figure 28: Left: ω_D versus poloidal angle θ for a E=1keV, $\Lambda = 0.85$ trapped electron (dots: numerical, equilibrium (I); solid: formula (144)). Right: α-particle with the same properties as in figure (27)

It is no surprise that there are also substantial deviations for the orbit- averaged drifts, even for low energy electrons. This is due to the fact that ω_D is a difference between the large quantities $\dot{\varphi}$ and $q(r_0)\dot{\theta}$. Consequently, already very small radial drifts away from the $q(r_0)$-field line result in deviations from the analytical formula. For α-particles near the trapped-passing boundary it can be up to a factor of two (figure 29). A 2d plot for ω_D calculated by HAGIS demonstrates its dependence from Λ and energy (figure 30).

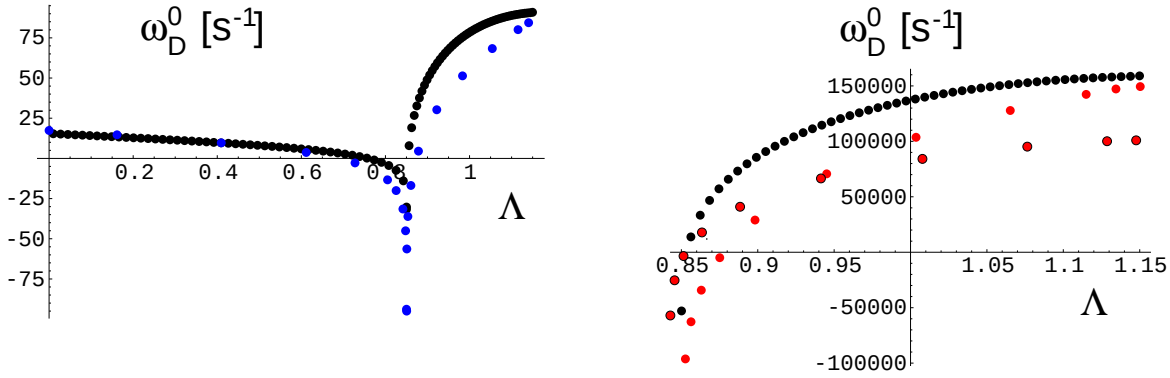

Figure 29: Left: ω_D^0 versus Λ for 1 keV electrons; blue dots: numerical, equilibrium (I); black dots: θ-averaged formula (144),(145). Right: trapped α-particles at 3.5MeV, black dots: analytical; red dots: equilibrium (I), black encircled red dots: elliptic equilibrium (II)

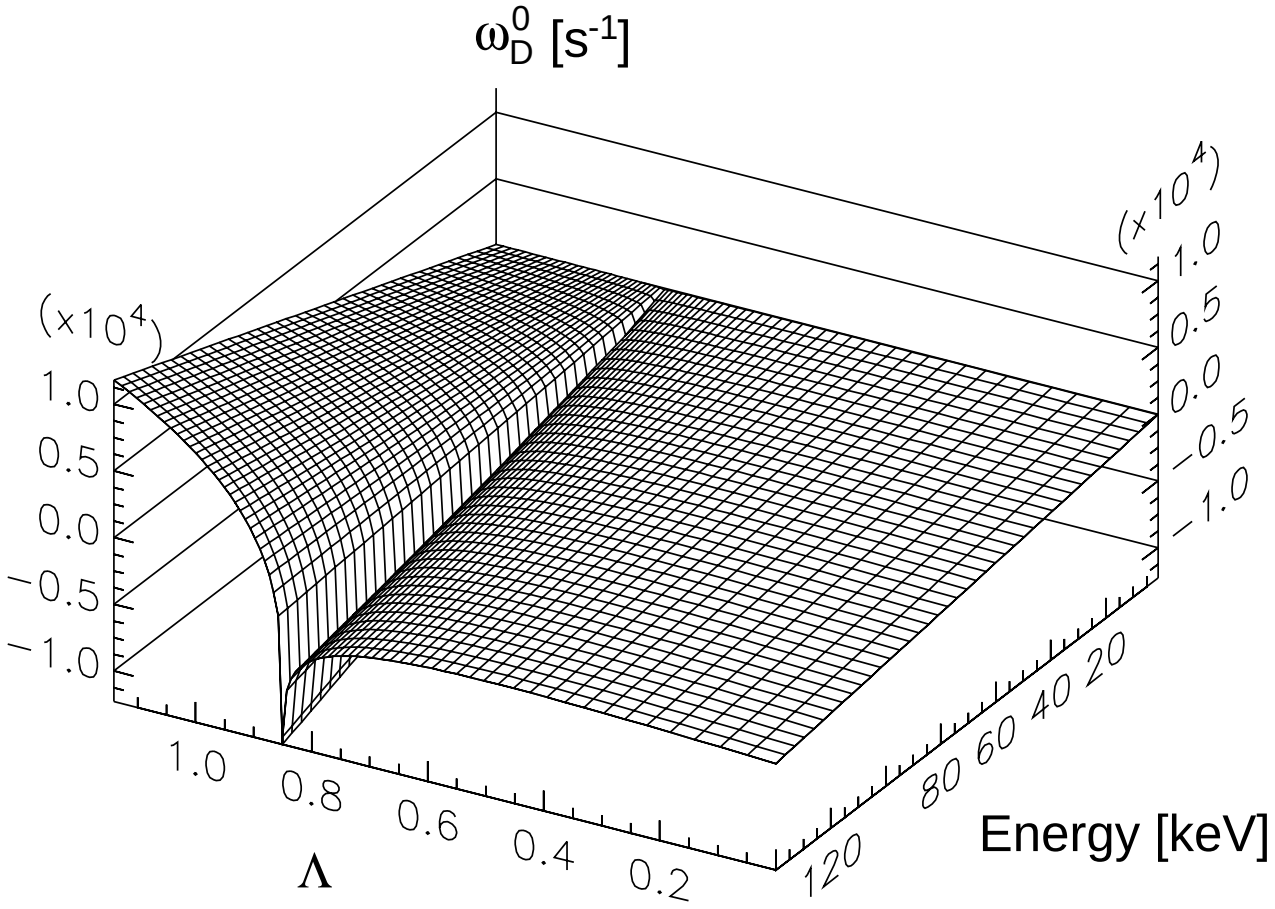

Figure 30: 2d plot for ω_D^0, hydrogen ions, equilibrium (I)

6.2.2 Propagator Coefficients

Now the propagator resp.its bounce-expansion-coefficients (see equations 124,123) are investigated. The analytical expressions are derived in [1] and [43] as:

$$\hat{a}_{k,m} = \int_0^{\theta_0} \frac{d\theta}{\sqrt{1-\Lambda/b(\theta)}} \left[\cos^2 \frac{k\pi}{2} \cos S_m\theta \cos k\omega_b\hat{t} + \sin^2 \frac{k\pi}{2} \sin S_m\theta \sin k\omega_b\hat{t} \right] \quad (146)$$

$$\hat{a}^G_{k,m} = \int_0^{\theta_0} \frac{d\theta}{\sqrt{1-\Lambda/b(\theta)}} G(\theta) \left[\cos^2 \frac{k\pi}{2} \cos S_m\theta \cos k\omega_b\hat{t} + \sin^2 \frac{k\pi}{2} \sin S_m\theta \sin k\omega_b\hat{t} \right] \quad (147)$$

$$K_{k,p,m} = \int_0^{\pi} \frac{d\theta}{\sqrt{1-\Lambda/b(\theta)}} \cos\left[S_p\theta - (k+\sigma S_m)\omega_t\hat{t} \right] \quad (148)$$

$$K^G_{k,p,m} = \int_0^{\pi} \frac{d\theta}{\sqrt{1-\Lambda/b(\theta)}} G(\theta) \cos\left[S_p\theta - (k+\sigma S_m)\omega_t\hat{t} \right] \quad (149)$$

First, we consider the trapped particle case for $\hat{a}_{km}$ and K_{kpm}. Comparison with the exact numerical results shows (figure 31), that for thermal hydrogen ions these formulae work quite well. The assumption that the coefficients are energy-independent is therefore justified. For energetic α-particles (figure 32) that simple approximation starts to become insufficient: even for an up-down symmetric equilibrium, the presence of W in the propagator starts to play a role. Deviations of 10% and more are the consequence. In that limit also equation (118)

$$a_{m,k} = \frac{K_{m,m,k}}{L_t} \tag{150}$$

starts to break down, since W enters K with an opposite sign.

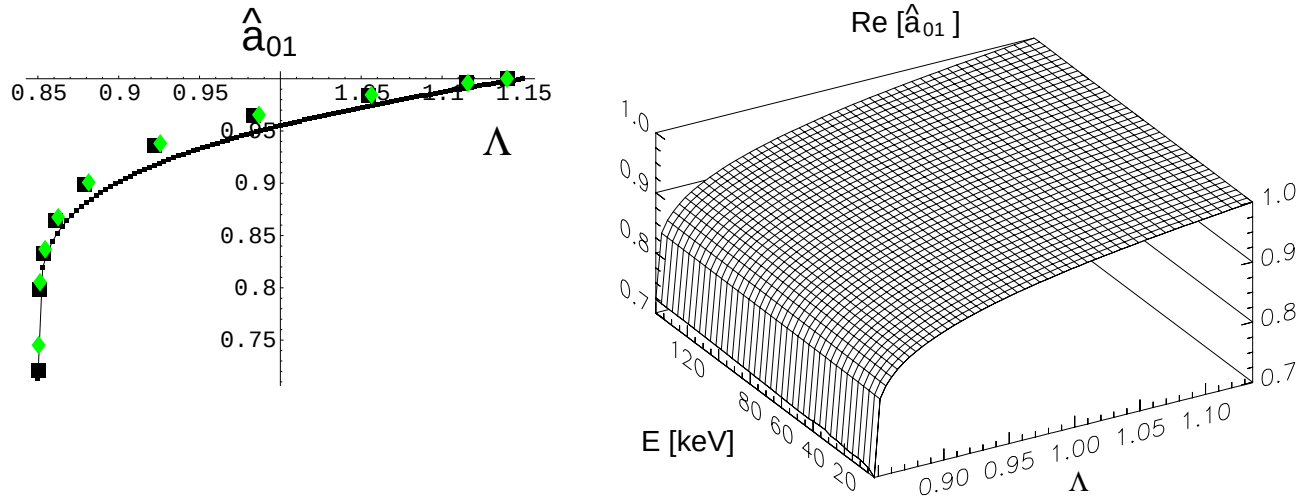

Figure 31: Left: the coefficient $\hat{a}_{km}$ for $k = 0,\ m = 1$; black line: analytical formula (124), black dots: 1keV ions, equilibrium (I); green dots: 140 keV ions, equilibrium (I) Right: 3D plot for $\hat{a}_{01}$ versus Λ and energy, hydrogen ions, equilibrium (I)

In figure 32 also the case of a non-up-down-symmetric equilibrium is considered: for an equilibrium with the same physical parameters as equilibrium (I) but with a JET-like shaped cross section, the discrepancy to the analytical expression becomes 20% and more. In that case, one would also expect that the imaginary part of the coefficients starts to play a role due to the sin-contribution in the exponential factor. However, numerical integration shows that the maximum values of $\mathrm{Im}[\hat{a}_{km}]$ and $\mathrm{Im}[\hat{K}_{kp}]$ are at least one order of magnitude smaller than their real parts for any m, p and k. Therefore they are not taken into account in this implementation.

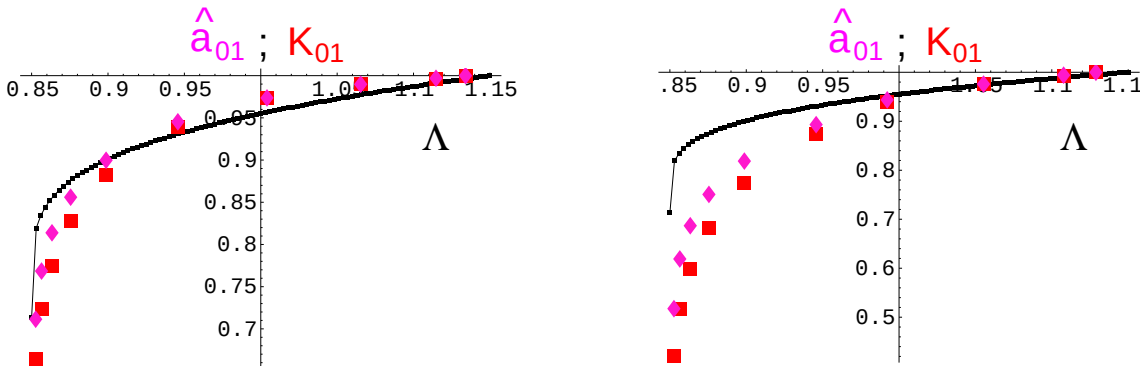

Figure 32: Left: the coefficients $\hat{a}_{km}$ and K_{kp} for $k = 0,\ m = 1$, 3.5 MeV α-particles ; black line: analytical formula (146), pink diamonds: $\hat{a}_{01}$; red dots: K_{01}, equilibrium (I); Right: the same quantities as on the left, but here for a non-up-down-symmetric equilibrium;

Now integrals including ω_D are examined. As we can expect from the discussion of ω_D above, Figure 33 shows substantial differences between numerical results and analytical approximation. These differences again arise mainly due to the Shafranov shift. The effect of W can also be observed, especially for the 3.5 MeV α-particles.

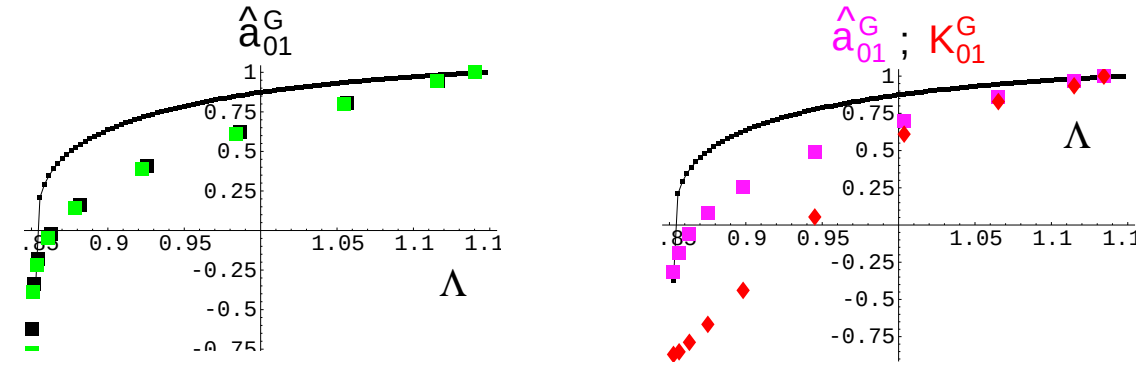

Figure 33: Left: $\hat{a}^G_{km}$ for 1 keV (black dots) and 140 keV (green dots), $k = 0,\ m = 1$, black line: formula (147) Right: the coefficients $\hat{a}^G_{km}$ (pink diamond) and K^G_{kp} (red dots) for $k = 0,\ m = 1$, 3.5 MeV α-particles, equilibrium (I)

The discussion above could now be repeated for the circulating-particle-case. But since there is no new physics in such a discussion and the radial drifts are at least two times

smaller than for trapped particles, a detailed discussion is not carried out here.

From this discussion the conclusion can be drawn that the analytical formulae for circular concentric geometry (that are used inter alia in KIN2DEM) are no longer applicable when realistically shaped equilibria are considered. The higher the energy of the particle is and the nearer one approaches the trapped-passing boundary the larger become the deviations between numerical calculation and analytical approximation. The Shafranov shift changes especially all those integrals (up to 50%) that involve ω_D^0. Elliptic and asymmetric equilibria reinforce this trend. Therefore, the use of the numerical orbit integration results (obtained with HAGIS) in LIGKA is an indispensable component for the accurate treatment of general 2d tokamak geometries.

6.3 Internal Kink Mode

As one possible application of LIGKA, in this section the kinetic modifications of the internal kink mode are examined. As discussed in section 6.1.3, the internal kink exhibits only relatively small MHD growth rates e.g. $\mathcal{O}(\epsilon^2)$ smaller than the external kink. However, the so called 'fishbone' and 'sawtooth' modes in today's tokamaks that both have a (m=1,n=1) kink structure, cause considerable problems due to their interaction with fast ions due to external heating. As possible future applications of LIGKA, these modes are discussed in the outlook.
Here, a similar example as investigated in section 6.1.3 is chosen: for the same profiles and parameters, but now based on a numerical HELENA equilibrium, the case $q_0 = 0.85$ is considered. The ideal MHD growth rate calculated by LIGKA $\gamma = 4.36 \cdot 10^4 s^{-1}$ is very close to the CASTOR result $\gamma = 4.40 \cdot 10^4 s^{-1}$. Now the kinetic influence of the background particles is studied:
For circulating particles the important factor within the kinetic integrals is:

$$\frac{(\omega - \hat{\omega}_*)\omega}{\omega^2 - (S_m^0 + k)^2 \omega_t^2} \tag{151}$$

The equilibrium's mean temperature is $\sim$ 30keV. This translates into an $\omega_t \sim 8 \cdot 10^5 s^{-1}$ for ions and $\omega_t \sim 3 \cdot 10^7 s^{-1}$ for electrons. Since the typical mode frequency of an internal kink with the parameters above is $\sim 1 \cdot 10^5 s^{-1}$, the denominator of equation (151) can become zero if $k \approx -S_m^0 = m - nq(r)$. This is only possible in very narrow regions near a resonant surface. Therefore, circulating particles cannot modify the ideal MHD picture significantly.

For trapped particles this changes: the resonance denominator of the expression

$$\frac{\omega - \hat{\omega}_*}{\omega - \omega_D^0 - k\omega_b}, \tag{152}$$

can become close to zero for two different reasons: firstly, for $k = 1$ the bounce frequency $\omega_b \sim 2.5 \cdot 10^5 s^{-1}$ for ions can coincide with the mode frequency. Secondly, for $k = 0$ the magnetic drift $\omega_D^0 \sim 8 \cdot 10^4 s^{-1}$ for ions can cause a resonant contribution from expression (152). The trapped electrons' frequencies are still too high to fulfil the first resonance condition, but the $k = 0$ resonance can be matched since $\omega_{D,ions}^0 \sim \omega_{D,el}^0 \sim \omega$.
Also the diamagnetic drift represented by $\hat{\omega}_*$ plays a role. For ions (where $\hat{\omega}_* > 0$), it can reduce the nominator significantly (or even make it zero), resulting in a stabilising influence on the mode's growth rate.

This theoretical discussion is verified by numerical results: as a first step, only circulating contributions are switched on. The resulting growth rate, $\gamma = 4.38 \cdot 10^4 s^{-1}, Re(\omega) = 0.13 \cdot 10^4 s^{-1}$, deviates only slightly from the MHD case ($\gamma = 4.40 \cdot 10^4 s^{-1}, Re(\omega) \sim 10 s^{-1}$), and also the eigenfunctions stay almost the same (see figure 34). The real part of ω raises (for the ideal MHD case it should be exactly zero; the small, non-zero result of LIGKA is purely numerical, as in other ideal MHD codes, due to discretisation errors) but stays at a low level compared to the growth rate.

When trapped particles are taken into account, but their diamagnetic drift $\hat{\omega}_*$ is set to zero, the growth rate increases to $\gamma = 5.65 \cdot 10^4 s^{-1}$, and a significant raise in the real frequency ($Re(\omega) = 8.20 \cdot 10^4 s^{-1}$) is found. When the diamagnetic drift terms are switched on, γ goes down to $5.11 \cdot 10^4 s^{-1}$, but the real frequency stays approximately on its previous level $Re(\omega) = 8.16 \cdot 10^4 s^{-1}$. Now the dominant eigenfunctions (figure 35) change their structure: the electromagnetic potential ψ becomes larger and broader than the electrostatic potential ϕ. This broadening can be attributed to kinetic effects that smooth out the resonant surface. A similar behaviour was also found by Qin [1].
However, the eigenfunctions show that a grid refinement in the radial coordinate at the $q = 1$ surface is desirable to resolve the fine structured physics at this thin layer. An improvement of LIGKA in that respect is planned for the future.

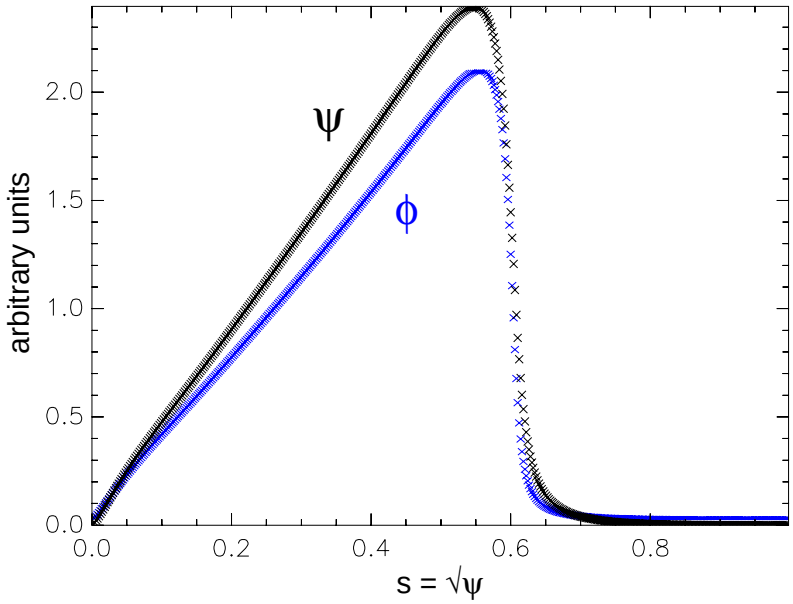

Figure 34: Electrostatic (blue) and electromagnetic(black) potential of the $m = 1$ component of an unstable kink mode for $q_0 = 0.85$ and only circulating particles.

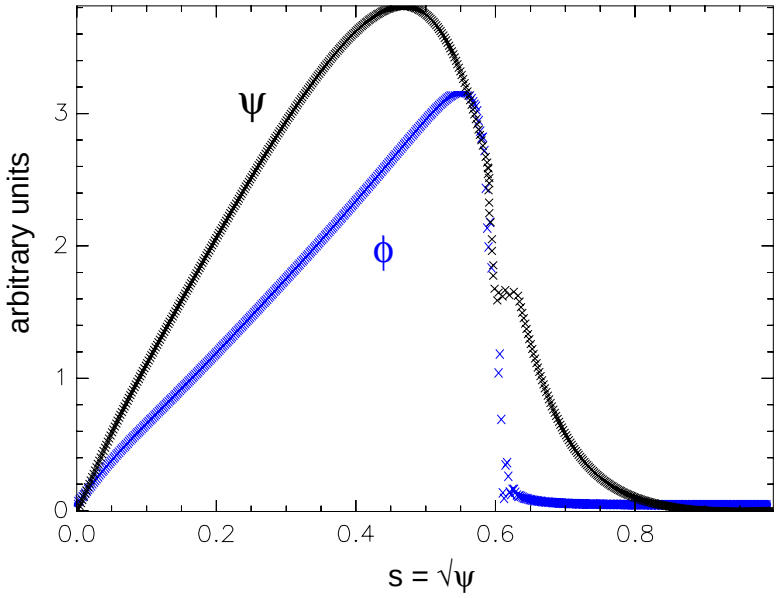

Figure 35: Electrostatic (blue) and electromagnetic(black) potential of the $m = 1$ component of an unstable kink mode for $q_0 = 0.85$ with trapped particles and $\hat{\omega}_*$ switched on

6.4 Toroidal Alfvén Eigenmodes

As another application case, the Toroidal Alfvén Eigenmode (TAE) is investigated.
This mode has caused great interest because of its possible danger for the stability of a burning Tokamak plasma. The first comprehensive description of TAE's can be found in [54], where it was shown analytically and numerically how toroidal geometry breaks up the continuous Alfvén spectra, generates gaps and permits global modes within these gaps. In the pure MHD picture these global modes are stable and therefore not dangerous for plasma stability.

To understand why TAE modes cannot exist in slab or cylindrical plasmas, an effect called continuum damping has to be investigated: a shear Alfvén wave package, travelling in an inhomogeneous plasma always hits a surface located at $r = r_0$ where the Alfvén resonance condition $\omega = k_\parallel v_A(r)$ is fulfilled. Here, in the vicinity of r_0, the shear Alfvén waves become dispersive, since $2\pi/k_\perp$ becomes small (consequence of the dispersion relation (137)) and thus comparable to the ion gyro radius: in that limit, the ions do not follow the field lines any longer, since the perturbing field changes their orbit significantly. In contrast, the electrons due to their smaller gyro-radius stay on the field lines producing charge separation. This effects breaks down the ideal MHD model and the continuous spectrum is replaced by a discrete spectrum with regular eigenfunctions, called KAW (kinetic Alfvén waves) [69][70]. Near r_0, the incident shear wave strongly couples to the KAW, resulting in a modified dispersion relation where $\partial\omega/\partial k_\perp \neq 0$. Consequently, each slice of the wave packet is scattered at a different r_0 in a different direction. This leads to an effective damping of the propagating wave.
In the presence of gaps, where there are no resonant surfaces, damping is missing. Therefore a wave excited by some driving mechanism can grow within the gap and can become unstable. One possible driving mechanism are energetic particles whose bounce resp. passing frequency coincides with a gap. The free energy of the particles can excite a TAE and drive it unstable. In return, a TAE also transfers back energy to the particles causing a change in the fast ion distribution function leading to a high particle transport or to particle losses.

To explain its MHD-features (for the first time described in [54]) we start with a spectrum of the shear Alfvén mode in tokamak geometry for different poloidal mode numbers. Since the solution of the dispersion relation in that case is approximately given by

$$k_\parallel = \frac{1}{R_0}(n - \frac{m}{q(r)}) \tag{153}$$

it is easy to see that branches for different values of m can intersect, dependent on the specific form of $q(r)$: if all coupling terms are turned off, one obtains a spectrum as shown in figure 36. If now coupling terms are turned on, the degeneracy of the branches at the

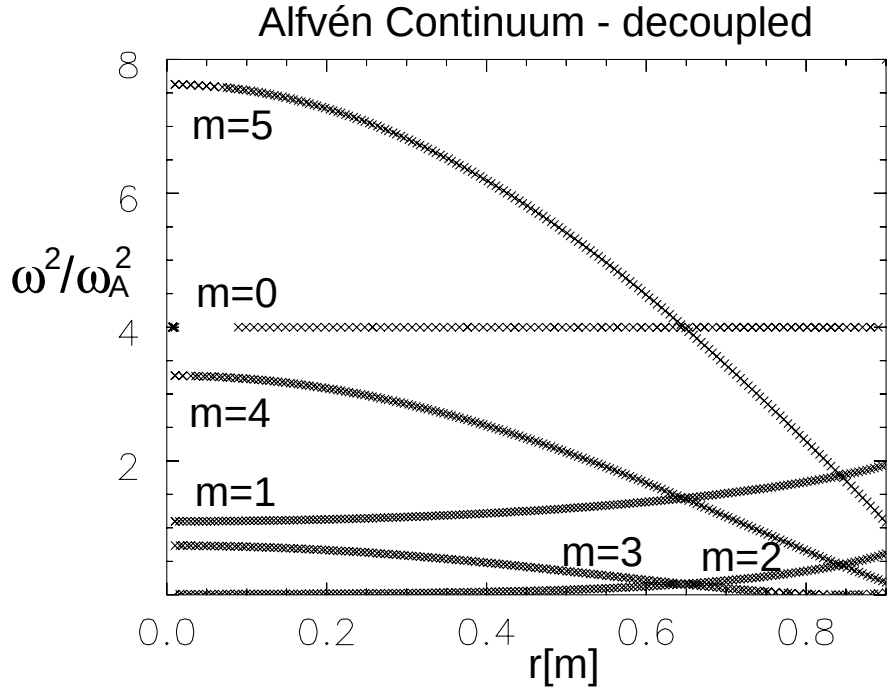

Figure 36: Decoupled Alfvén spectrum: due to the q- dependence of $k_\parallel$, curves for different m number can intersect

intersection points is removed. Physically, this phenomenon can be understood in analogy to the band structure of the electron spectrum in the presence of a periodic lattice of ions in a crystal. Bragg reflections with the ions cause standing electron waves with two main phases with respect to the lattice: one phase whose corresponding wave function (resp. its square) is maximal between the ions and one that is maximal at the ions. Since the total energy for an electron being localised near an ion is lower than in between the ions, two energy bands exist with a typical gap size of a few eV for a lattice with $\sim 5\mathring{A}$ distance between the ions.

In a tokamak, the periodicity of the magnetic field in the poloidal coordinate induces the coupling. The two 'bands' correspond to a localisation of the wave either in the 'good' or 'bad' curvature region ('even' and 'odd' mode, see figure 38). The radial location of the gaps can be determined by setting

$$k_{\parallel m} + k_{\parallel m+1} = 0 \tag{154}$$

which results in:

$$q(r_0) = \frac{m + 1/2}{n} \tag{155}$$

The width of the gap is approximately given by [1]:

$$\Delta = \frac{4n^2 r_0/R_0}{(r_0^2/R_0^2 - 1)(2m+1)^2} \sim \mathcal{O}(\epsilon) \tag{156}$$

It can be shown [54] that for higher order coupling the gaps are of order $\mathcal{O}(\epsilon^2)$.
All these features are obtained with LIGKA in the MHD limit: for an analytical circular equilibrium, we firstly reproduced the decoupled spectrum with crossing branches for different m numbers (see figure 36). Furthermore, switching on the coupling terms produces gaps at the predicted r_0 and with the right gap sizes (see figure 37).

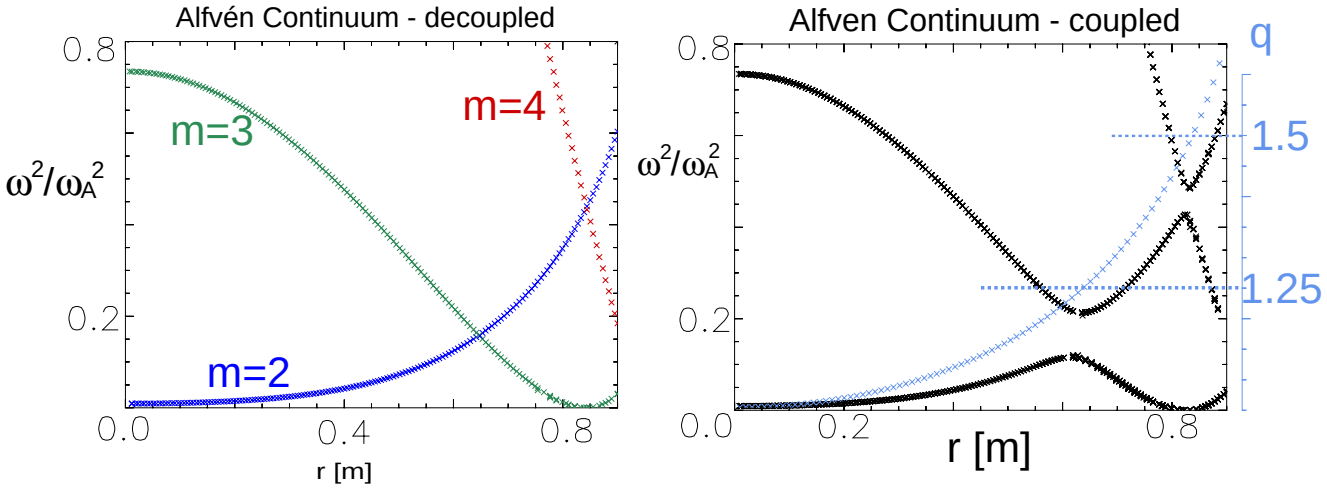

Figure 37: Poloidal mode coupling between $m = 2$ and $m = 3$ resp. $m = 4$ modes: the radial position at the gap r_0 agrees with formula (155) and the gap has a size of ≈ 0.1 (2-3 coupling) as predicted with formula (156)

A benchmark with CASTOR for numerical equilibria was also done. For a series of equilibria - shape of equilibrium (I) (appendix 8.8.4) with $q_0 = 1.05$, $a = 0.9$m, $B_0 = 5$T, $n(\psi) = n_0 = 5 \cdot 10^{19}\text{m}^{-3}$ - where R_0 (i.e. the aspect ratio) was varied between 3m and 5m, the mode frequencies of the even and odd mode are compared: figure 39 shows perfect agreement between the mode frequencies calculated with CASTOR [48] and LIGKA in the MHD limit. Also the mode structures, shown in figure 40 for the case $R_0 = 4$m are very similar to each other. The difference for the $m = 3$ component might be due to the

fundamental difference of the models in CASTOR and LIGKA. However, KIN2DEM [1] shows the same mode ratio as LIGKA.

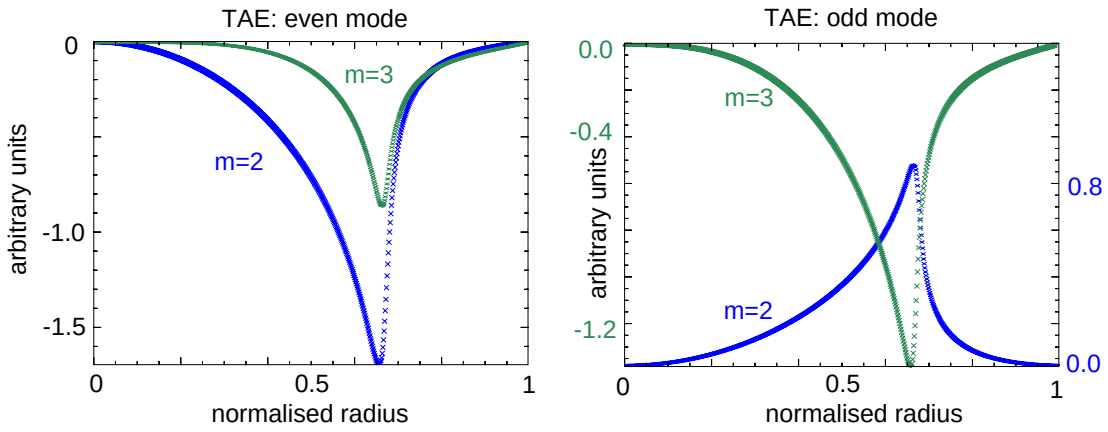

Figure 38: Eigenfunctions of a TAE mode calculated by LIGKA; even(left) and odd (right) mode

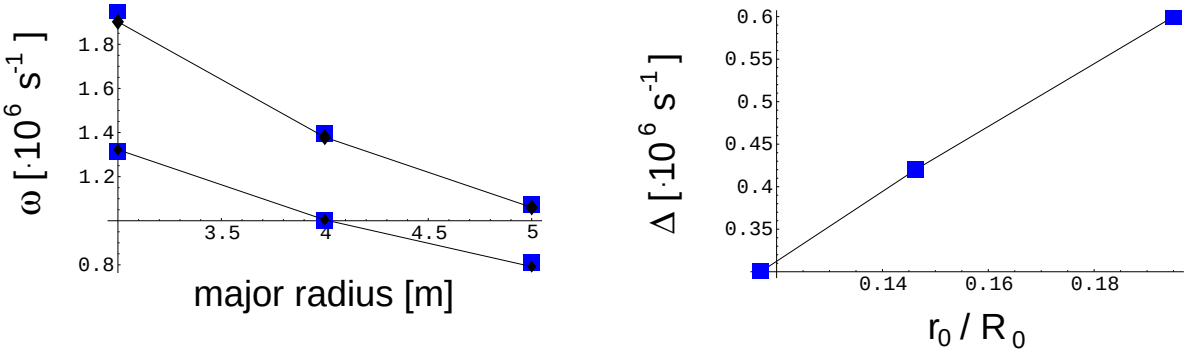

Figure 39: Left picture: Mode frequency comparison between CASTOR (black diamonds) and LIGKA (blue squares) for the even (lower line) and odd (upper line) TAE gap mode ($m = 2/3$). For three equilibria with different R_0 and a fixed minor radius ($a = 0.9$) the gap size (right picture) scales linearly with r_0/R_0 as predicted by formula 156.

Now TAE modes in the elliptic equilibrium (II) are examined. Ellipticity changes the gap ordering described above. The reason for this is the presence of higher order harmonics in the equilibrium quantities: in the circular case the magnitudes of the n-th order coupling terms behave like $\mathcal{O}(\epsilon)^n$ (asymptotic decoupling). In the elliptic case, this ordering is not valid any more. The example in figure 41 shows that a strong coupling between the $m = 2$

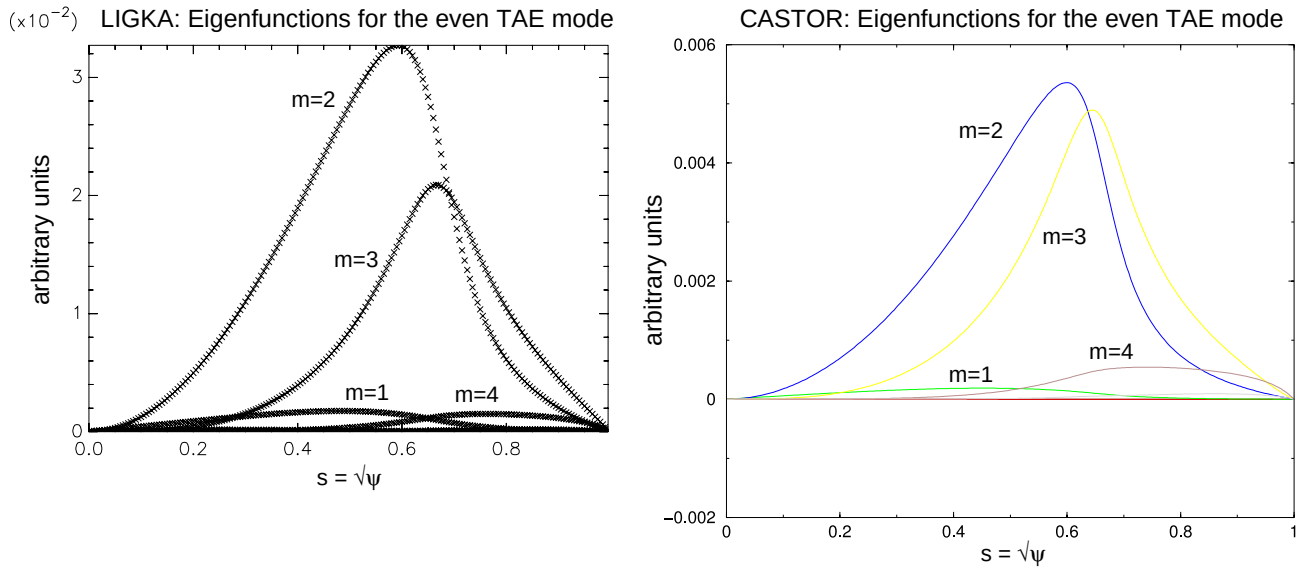

Figure 40: Eigenfunctions of the TAE gap mode, LIGKA vs. CASTOR

and $m = 4$ harmonics takes place resulting in an even more extended gap than the 2/3 gap. (Of course, this is also due to a bigger r_0/R_0, since the intersection point lies at a larger r_0.)

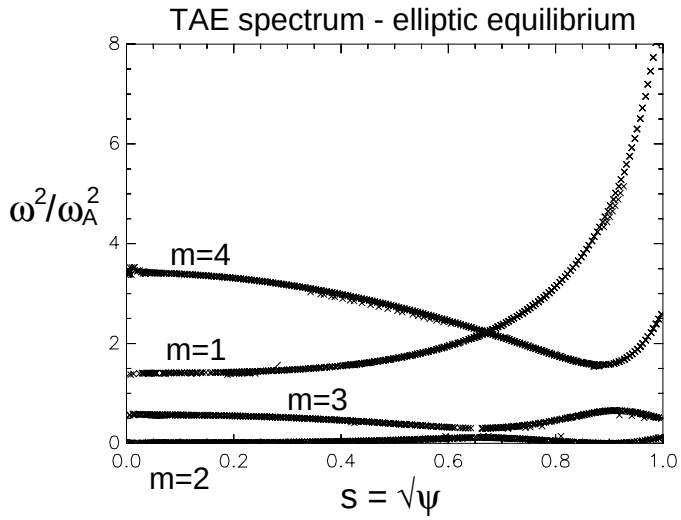

Figure 41: For an elliptic equilibrium, there is effective coupling also for non-neighbouring modes: here between the $m = 2$ and $m = 4$ branch.

Now kinetic modifications of the TAE mode are investigated. In order to do so a population of superthermal Maxwellian hydrogen ions is added to the system. The parameters for this third species are chosen to be:

$$p_{hot} = p(0)e^{-\psi/0.09} \tag{157}$$

with a constant temperature profile T_h. Following Qin's choice [1] for the temperature of the hot ions at the magnetic axis, $v_{th/hot} = \sqrt{2T_{hot/0}/m}$ is varied over the interval

$$0.5 < v_{th/hot}/v_A < 1.5, \tag{158}$$

and the poloidal $\beta_{hot/0} = 2\mu_0 p_{hot/0}/B_{\theta/a}$ at the magnetic axis is chosen as 1. The background temperature is set to:

$$T_i = T_e = \frac{1}{2}(1-\psi)^2 \text{keV} \tag{159}$$

Again equilibrium (I) (appendix 8.8.4) is chosen with $q_0 = 1.05$, $a = 0.9$m, $B_0 = 5$T, $n(\psi) = n_0 = 5 \cdot 10^{19}\text{m}^{-3}$ and $R_0 = 4$m.

Before discussing the numerical results, an overview of driving and damping effects for TAE modes is given. The most important term for driving and damping is the expression

$$\frac{\omega - \hat{\omega}_*}{\omega - \omega_D^0 - k\omega_b}, \tag{160}$$

derived in chapter 4.4. The term containing $\hat{\omega}_*$, that was defined as

$$\hat{\omega}_* = -\frac{\mathbf{b} \times \nabla F_0}{ieB\frac{\partial F_0}{\partial E}} \cdot \nabla \tag{161}$$

represents the free energy available to the whole system due to the spatial gradients of the distribution function. Since in our example the choice of p_{hot} and T_{hot} define a relatively peaked n_{hot} and $F_{0/hot}$, one expects a strong destabilisation of the TAE mode. This is also due to the fact that the gap-mode frequency ($1.0 \cdot 10^6\ s^{-1}$, see figure 39) is in the range of the bounce frequency of the fast ions which is also $\sim 1 \cdot 10^6\ s^{-1}$. Thus resonances between fast particles and the gap mode can occur for the $k = 1$ harmonic which is mathematically described by a small (or even vanishing) denominator in formula (160). This process is called inverse Landau damping.

The term proportional to ω describes the 'usual' Landau damping and is therefore stabilising.

There is another damping effect, called 'radiative' damping [71], originating from FLR-effects. This phenomenon is caused by the small coupling between TAE modes and KAW

within the gap. The excited KAWs carry away energy from the gap region and therefore stabilise the TAE mode.
Of course, there is also damping due to the background: especially the trapped electrons ($T_e = 0.5keV$) can interact with the mode: for $k = 0$ the trapped electrons' magnetic drift frequency ω_D^0 is around $1 \cdot 10^6$ causing resonance due to expression (160). Since ω_b ($2 \cdot 10^6$) and ω_t ($4 \cdot 10^6$) are too high compared to the mode frequency, $k = \pm 1$ resonances are excluded. For background ions, only higher harmonics in the bounce frequency can cause damping. However, in our example, the passing-ion frequency is too small ($1 \cdot 10^5$) to play a significant role.
As a last point, finite banana orbit width effects (Δ_b) are investigated. It was shown in [72] and [73] that for increasing Δ_b, the growth rate saturates and decreases substantially when Δ_b becomes larger than the typical radial mode width r_m/m. In our example, $r_m/m \approx 0.25a$ and Δ_b/a for 1 MeV hydrogen ions is $0.4a$. Therefore, when finite orbit widths are taken into account, stabilisation can be expected.

Now the numerical results shown in figure 42 are discussed: the growth rate increases with the fast particle velocity and the real part of the frequency is shifted. The results obtained

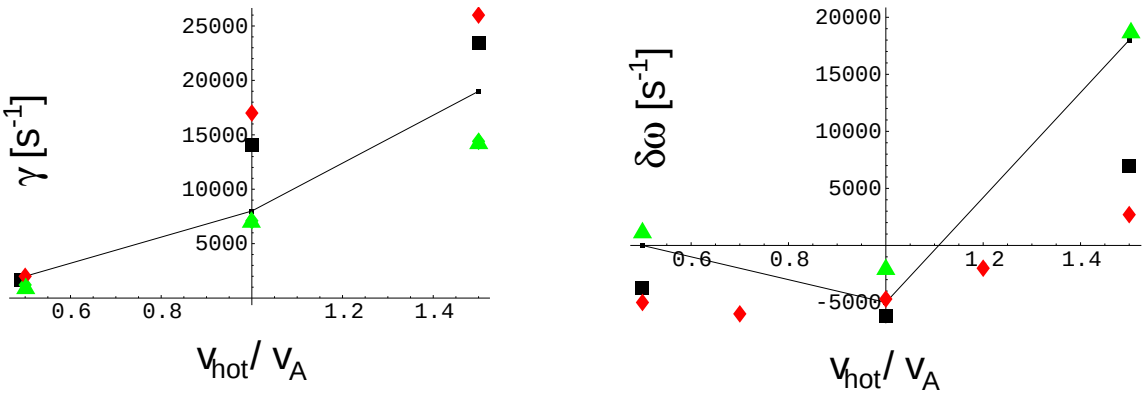

Figure 42: Growth rate (left) and frequency shift (right) of the (m=2,3) TAE mode: KIN2DEM (black line) and CAS3D (red diamonds) vs. LIGKA with (green triangles) and without (black squares) finite orbit width effects

with LIGKA agree reasonably well with other codes which are capable of dealing with fast particle effects in different approximations: the red diamonds in figure 42 represent CAS3D3K results [50]. CAS3D3K is a perturbative kinetic MHD code based on CAS3D [52] which is a linear, ideal, 3-dimensional MHD code, here applied in the 2d tokamak

geometry limit. The fast particle treatment of CAS3D3K is based on a drift kinetic description with zero banana orbit width. When the banana width is also neglected in LIGKA (black squares), an acceptable agreement of both codes is found. The remaining discrepancy can be attributed to the fact that FLR-effects are missing in CAS3D3K. This is in agreement with the discussion above. When the finite orbit widths are switched on in LIGKA (green triangles), the growth rate decreases considerably, especially for higher $v_{th/hot}$. It is even smaller than predicted by KIN2DEM (solid line), which uses a Taylor expansion in the banana width. This also agrees with the fact that for large banana widths, the Taylor expansion becomes inaccurate and underestimates the stabilising influence.

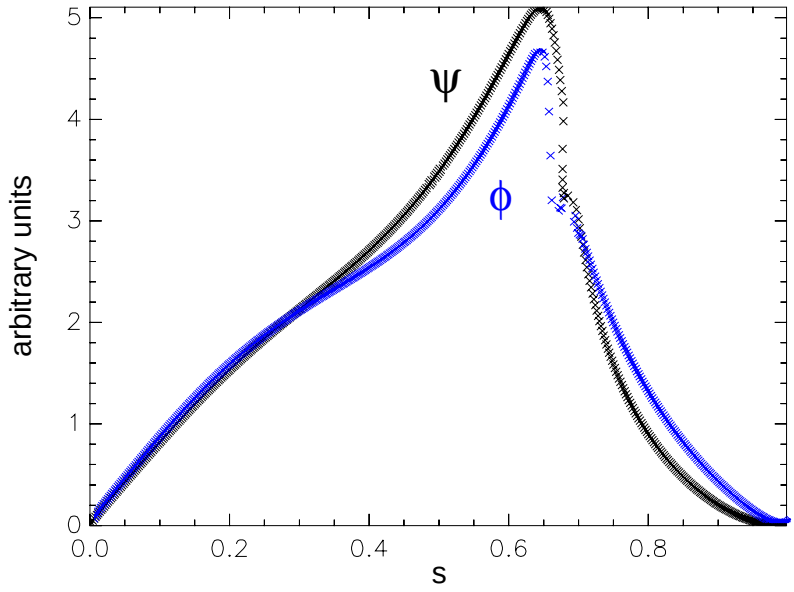

Figure 43: Electrostatic (blue) and electromagnetic (black) potential of the $m = 2$ component of an instable TAE mode ($v_{th/hot} = 0.5 v_a$)

The eigenfunctions for the $m = 2$-component are shown in figure 43: the electrostatic (black) and electromagnetic (blue) potential are now different, which is mainly the effect of the quasi-neutrality equation. The mode is more localised at the resonant layer r_0 than the pure MHD mode (figure 40) which can be attributed to the damping due to large banana orbit widths. The small step in the eigenfunctions might be due to the coupling to the KAWs. Further detailed investigations of this coupling between TAEs and KAWs, (i.e. the radiation damping) have to be carried out in the future.

7 Conclusions and Outlook

In this dissertation a powerful tool for investigating the influence of superthermal particles on the linear MHD stability of fusion plasmas has been developed. It was shown that it is able to reproduce various ideal MHD results and that it can treat problems where large scale MHD modes are modified by kinetic effects. The developed code LIGKA (Linear Gyrokinetic Shear Alfvén Physics) is based on a gyrokinetic MHD model developed by H. Qin [1]. Compared to this original model and the code KIN2DEM [1], several significant improvements both in theory and in the numerical implementation have been performed. With these improvements, summed up below in more detail, LIGKA is a more comprehensive and accurate code, as far as large scale kinetic MHD problems are concerned, than other implementations, namely CASTOR-K [56] (which treats the particle orbits exactly, but uses a hybrid, perturbative MHD model without finite Larmor radius effects of the background plasma) or PENN [66] (which is based on a gyrokinetic dielectric tensor formulation but with some restricitons for large banana orbits).
On the theory side, H. Qin's original model was extended in three areas: in order to take into account all finite Larmor radius contributions (which is important for an accurate prediction of damping rates), the gyro-terms were also kept within the kinetic integrals of the gyrokinetic moment equation; expressions for non-Maxwellian distribution functions (slowing down) were derived; the Taylor expansion for the banana orbit width was replaced by a more accurate expression.
On the numerical side, several new issues compared to other codes were implemented. The most important improvements are:

- The system of equations is coded for general 2d tokamak geometry that allows realistic tokamak equilibria instead of a simple unshifted circular model as in KIN2DEM. For that a MATHEMATICA based analytical expansion for the differential operators was used. An interface for the numerical equilibrium code HELENA was implemented to allow realistically shaped equilibria and the inclusion of the Shafranov shift.

- To take into account the realistic geometry also for the unperturbed particle orbits, the drift kinetic code HAGIS is used to evaluate all the quantities needed by LIGKA. For an accurate resolution near the trapped/passing boundary a TPB-finding tool was developed.

- In a linear model, the discretisation in the radial direction and the orbit integration can be exchanged. Providing the necessary information with HAGIS, large banana

widths for trapped ions can be taken into account more accurately than previous implementations.

In the MHD limit, LIGKA was successfully benchmarked against analytical formulae and other MHD codes: the basic features of shear Alfvén waves and the internal kink mode were reproduced both in cylindrical and toroidal tokamak geometry.
A detailed analysis of particle orbits and their contributions to the kinetic integrals via the propagator coefficients was carried out. It was shown that even when the flux surfaces are circular, for highly energetic particles the analytical formulae (that are e.g. used in KIN2DEM) become insufficient, especially when drifts in the presence of shifted flux surfaces are involved. Elliptic and non-up-down-symmetric poloidal cross sections definitely require numerical treatment. There are also substantial changes - especially near the trapped/passing boundary - when non-standard orbits (e.g. potato orbits) are considered.
As an application, the kinetic modifications of the internal kink mode were examined. It was found that circulating particles do not change the ideal MHD result significantly because no resonances between mode frequency and periodic particle motion are present. Trapped particles destabilise the mode whereas switching on the diamagnetic drift terms has a stabilising influence.
Finally, TAE modes were investigated with LIGKA. All MHD features of these mode were recovered: the break up of the continuum, the location of the gap, the gap size and the eigenfunctions are in perfect agreement with analytic theory and other MHD codes. Then the driving and damping effects due to energetic particles and the background plasma were discussed. It was shown, in agreement with other numerical results, that the TAEs can be destabilised by a sufficiently hot superthermal ion population. The inclusion of a finite banana orbit width was found to be stabilising, as predicted by earlier investigations. Nevertheless, none of the previous calculations was based on such a comprehensive implementation as realised in LIGKA. Therefore, the stabilising effect of large orbit widths was found to be underestimated so far.

Outlook

Hand in hand with further numerical improvement, e.g. for the resonance integrals or the eigenvalue finder (parallelisation), in the future numerous physical questions can be addressed:
As indicated in the TAE-section, the coupling of TAEs to the KAWs should be examined in further detail. This coupling, i.e. the radiation damping, has been claimed to have a

strong stabilising effect: based on PENN calculations [66], all TAE modes in conventional tokamak scenarios (monotonic current profile) with separatrix equilibria in ITER should be stable [75]. Since these predictions are the only full gyrokinetic results so far, a systematic benchmark with the PENN code for TAE stability is planned. This is especially interesting, because PENN uses a dielectric tensor formulation with finite Larmor radius effects up to second order and a simple approximation for the banana orbits. Therefore also more insight in the different theoretical models and their range of validity can be won.

Another issue is a detailed investigation of kinetic effects on the (1,1) kink mode. One possible application is the so-called 'fishbone' mode in today's tokamas. It has been found that fast ions, originating e.g. from the injection of high energy neutral beams, can destabilise the plasma by interacting with the internal kink mode resulting in an energy and confinement loss. Detected by soft-X-rays or magnetic coils, rapid bursts with a typical time interval of $\sim$ 10ms form the typical 'fishbone' pattern. The mechanism responsible for that mode was found to be a resonance between the kink mode and the toroidal precession frequency of the banana tips [68]. The mode transfers its energy to the particles and thus its frequency ($\sim$ 50kHz) decreases. Now lower energy particles are in resonance, that before could not interact with the mode. Once all resonant particles are redistributed (or even thrown out of the plasma), the mode 'switches back' to its original frequency resonating again with newly deposited fast particles and the process restarts.
Besides fishbones, another (1,1) instability activity, called 'sawtooth instability', is prominent in tokamak plasmas. Sawteeth are magnetic reconnection events which flatten the temperature profile inside the $q = 1$ surface and prevent the current profile from strong central peaking. Fast particles have been found to stabilise these sawteeth due to the ω_*-mechanism. This effect can make sawteeth quite rare but more dramatic events.

From these examples it becomes obvious that depending on the particular conditions, that fast ions can be either stabilising or destabilising. In order to understand this process in more detail, also the non-linear interaction between MHD modes and fast particles including kineticly modified eigenfunctions is of great interest. So far, only the pure MHD eigenfuctions were used to carry out these non-linear calculations.
In order to use the capability of LIGKA for this problem, the following interplay of codes is planned (see figure 44): after the mode has significantly changed the fast particles' distribution function (calculated with HAGIS), a correction of the eigenfunctions is obtained by LIGKA. Feeding this result back into HAGIS, again the non-linear particle-wave-interaction evolves the distribution function. From this iterative procedure, a more

comprehensive understanding of the non-termal ions' stabilising or destabilising influence on the (1,1) kink mode can be expected.

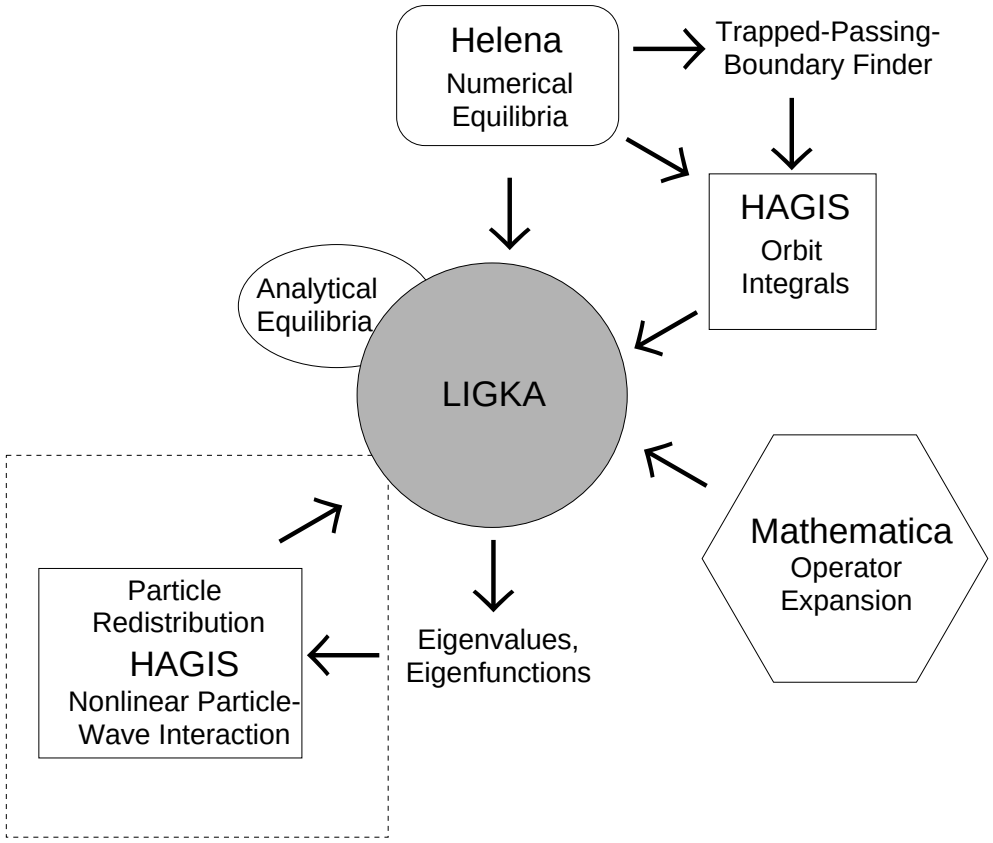

Figure 44: Iterative runs of LIGKA together with the non-linear particle-wave interaction code HAGIS are planned to examine e.g. the time dependent fishbone cycle

8 APPENDIX

8.1 Klimontovich-Equations

Following [21] and [26], we start with the equation of motion for a particle i of species α in an electromagnetic field:

$$\frac{d\mathbf{r}_{\alpha,i}}{dt} = \mathbf{v}_{\alpha,i}$$

$$\frac{d\mathbf{v}_{\alpha,i}}{dt} = \frac{eZ_\alpha}{m_\alpha}\Big[\mathbf{E}^m(\mathbf{r},t) + \frac{\mathbf{v}_{\alpha,i}}{c} \times \mathbf{B}^m(\mathbf{r},t)\Big]_{\mathbf{r}=\mathbf{r}_{\alpha,i}} = K_\alpha^m(\mathbf{r}_i,\mathbf{v}_i,t)$$

Here $\mathbf{E}^m$ and $\mathbf{B}^m$ are the microscopic fields governed by Maxwell equations. Due to their linearity, the fields can be written as a superposition of fields of the single particles:

$$\mathbf{E}^m(\mathbf{r},t) = \mathbf{E}^{ext}(\mathbf{r},t) + \sum_{\alpha,i} \mathbf{E^t}_{\alpha,i}(\mathbf{r},t|\mathbf{r}_{\alpha,i}(t)) \tag{162}$$

$$\mathbf{B}^m(\mathbf{r},t) = \mathbf{B}^{ext}(\mathbf{r},t) + \sum_{\alpha,i} \mathbf{B^t}_{\alpha,i}(\mathbf{r},t|\mathbf{r}_{\alpha,i}(t)) \tag{163}$$

$\mathbf{E}^{ext}$ and $\mathbf{B}^{ext}$ are externally applied fields; $\mathbf{E}^t_{\alpha,i}$ and $\mathbf{B}^t_{\alpha,i}$ are fields generated at position $\mathbf{r}(t)$ by particle i of species α at position $\mathbf{r}_{\alpha,i}(t)$.
Now the single particle distribution function is introduced:

$$f_\alpha^{exact}(\mathbf{r},\mathbf{v},t) = \frac{1}{n_\alpha}\sum_{i=1}^{N_\alpha}\delta(\mathbf{r}-\mathbf{r}_{\alpha,i})\delta(\mathbf{v}-\mathbf{v}_{\alpha,i})$$

It is assumed that we have N_α particles in the volume V; consequently the mean density is $n_\alpha = N_\alpha/V$ and thus $n_\alpha \int_V d\mathbf{r}d\mathbf{v} f_\alpha^{exact}$ is the number of particles of species α in the volume V.
Self consistency requirements lead to the definitions of charge density and current:

$$\varrho^m(\mathbf{r},t) = \sum_\alpha eZ_\alpha \int f_\alpha^{exact} d\mathbf{v} \tag{164}$$

$$\mathbf{j}^m(\mathbf{r},t) = \sum_\alpha eZ_\alpha \int \mathbf{v} f_\alpha^{exact} d\mathbf{v} \tag{165}$$

Differentiating f_α^{exact} with respect to t leads to:

$$\frac{\partial}{\partial t} f_\alpha^{exact} = \sum_{i=1}^{N_\alpha}\Big[\frac{\partial f_\alpha^{exact}}{\partial \mathbf{r}_i}\cdot\mathbf{v}_i + \frac{\partial f_\alpha^{exact}}{\partial \mathbf{v}_i}\cdot K_\alpha^m(\mathbf{r}_i,\mathbf{v}_i,t)\Big] \tag{166}$$

$$\tag{167}$$

We obtain terms of the following type:

$$\frac{\partial}{\partial \mathbf{r_1}}[\delta(\mathbf{r}-\mathbf{r_1})\delta(\mathbf{v}-\mathbf{v}_1)+\delta(\mathbf{r}-\mathbf{r_2})\delta(\mathbf{v}-\mathbf{v}_2)+...]+$$
$$\frac{\partial}{\partial \mathbf{r_2}}[\delta(\mathbf{r}-\mathbf{r_1})\delta(\mathbf{v}-\mathbf{v}_1)+\delta(\mathbf{r}-\mathbf{r_2})\delta(\mathbf{v}-\mathbf{v}_2)+...]+...=$$
$$\frac{\partial}{\partial \mathbf{r_1}}[\delta(\mathbf{r}-\mathbf{r_1})\delta(\mathbf{v}-\mathbf{v}_1)]+\frac{\partial}{\partial \mathbf{r_2}}[\delta(\mathbf{r}-\mathbf{r_2})\delta(\mathbf{v}-\mathbf{v}_2)]+...=$$
$$-\frac{\partial}{\partial \mathbf{r}}\sum_i^{N_\alpha}[\delta(\mathbf{r}-\mathbf{r}_i)\delta(\mathbf{v}-\mathbf{v}_i)]$$

Thus:

$$\sum_{i=1}^{N_\alpha}\frac{\partial f_\alpha^{exact}}{\partial \mathbf{r}_i}=-\frac{\partial f_\alpha^{exact}}{\partial \mathbf{r}},\qquad \sum_{i=1}^{N_\alpha}\frac{\partial f_\alpha^{exact}}{\partial \mathbf{v}_i}=-\frac{\partial f_\alpha^{exact}}{\partial \mathbf{v}} \tag{168}$$

And finally:

$$\frac{\partial}{\partial t}f_\alpha^{exact}=\Big[-\frac{\partial f_\alpha^{exact}}{\partial \mathbf{r}}\cdot\mathbf{v}-\frac{\partial f_\alpha^{exact}}{\partial \mathbf{v}}\cdot K_\alpha^m(\mathbf{r},\mathbf{v},t)\Big]$$

This is Klimontovich's equation. It still contains the same information as the equations of motion.

8.2 Liouville Equation and BBGKY-Hierarchy

In order to smooth the distribution function, one uses the concept of 'ensemble-averaging': one considers not only one distribution function for one plasma, but an infinite number of continously distributed plasmas.
The initial conditions $X(t=0)=X_0=X_{10},X_{20},...,X_{N0}$ with $X_{i0}=(\mathbf{r}_0,\mathbf{v}_0)$ are assumed to be randomly distributed. The probability, that the system is in the $\sum_\alpha 6N$- dimensional volume element dX_0, is defined by $F_N(X_0)\Pi_\alpha dX_0$. With advancing time $dX_0(t)$ is mapped to $dX(t)$. But it can be shown that the size of $dX(t)$ is an Poincare's integral invariant.Consequently, the probability, that the system is in the $\sum_\alpha 6N$- dimensional volume element dX_0, becomes $F_N(X,t)\Pi_\alpha dX$.
By the virtue of the constant dX_0, for $F_N(X,t)$ the Liouville equation holds:

$$\frac{\partial F_N}{\partial t}+\sum_{\alpha,i}\left(\mathbf{v}_{\alpha,i}\frac{\partial}{\partial \mathbf{r}_{\alpha,i}}+\frac{Z_\alpha e}{m_\alpha}\Big[\mathbf{E}^m(\mathbf{r}_{\alpha,i},t)+\frac{\mathbf{v}_{\alpha,i}}{c}\times\mathbf{B}^m(\mathbf{r}_{\alpha,i},t)\Big]\frac{\partial}{\partial \mathbf{v}_{\alpha,i}}\right)F_N=0$$

Liouville's equation still contains the equation of motion of every single particle system - way too much information than needed. For description of processes in plasmas one usually only needs the distribution functions of one and of two particles:

$f_1(X_1,t)dX_1/V$ with

$$f_1(X_1,t) = V\int dX_2...dX_N F_N(X,t)$$

gives the probability, that particle number one an be found in the volume element dX_1 around the position X_1 - independent of the position of all the other particles. Generally one defines:

$$f_s(X_1,...,X_s,t) = V^s\int dX_{s+1}...dX_N F_N(X,t)$$

Taking into account different particle species:

$$f_{\alpha,s}(X_{\alpha,1},...,X_{\alpha,s},t) = V^s\int F_N(X,t)dX_{\alpha,s+1}...dX_{\alpha,N}\Pi_{\beta\neq\alpha,j}dX_{\beta,j}$$

In order to obtain an expression for $f_{\alpha,1}$ one has to integrate Liouville's equation over $dX_2...dX_N$. In doing so, the following intermediate results are used:

$$V\int dX_2...dX_N\sum_{i=1}^{N}\mathbf{v}_i\frac{\partial f_N}{\partial\mathbf{r}_i} = \mathbf{v}_1\frac{\partial f_1}{\partial\mathbf{r}_1}$$

Here was taken into account that f_N tends towards 0 on the boundary of the enclosed volume. Furthermore:

$$\begin{aligned}
V\int\sum_{i=1}^{N}\mathbf{K}_i^m\frac{\partial F_N}{\partial\mathbf{v}_i}dX_2,...,dX_N &= V\int\mathbf{K}_1^m\frac{\partial F_N}{\partial\mathbf{v}_1}dX_2,...,dX_N \\
&\quad +V\int\sum_{i=2}^{N}\mathbf{K}_i^m\frac{\partial F_N}{\partial\mathbf{v}_i}dX_2,...,dX_N \\
&= \mathbf{K}_1^m\frac{\partial f_1}{\partial\mathbf{v}_1} + (N-1)V\int\mathbf{K}_2^m\frac{\partial F_N}{\partial\mathbf{v}_2}dX_2,...,dX_N \\
&= \mathbf{K}_1^m\frac{\partial f_1}{\partial\mathbf{v}_1} + \frac{(N-1)V}{V^2}\int\mathbf{K}_2^m\frac{\partial f_2}{\partial\mathbf{v}_2}dX_2
\end{aligned}$$

with

$$\mathbf{K}_i^m = \frac{Z_\alpha e}{m_\alpha}\Big[\mathbf{E}^m(\mathbf{r}_i,t) + \frac{\mathbf{v}_i}{c}\times\mathbf{B}^m(\mathbf{r}_i,t)\Big]$$

If we take into account more than one particle species α and generalise to s-particle distribution function we obtain the BBGKY-Hierarchy. It is called 'hierarchy', because in the equation for s there is also a term of the order $s+1$ [21]. Here, we just give the expression for f_1:

$$\Big[\frac{\partial}{\partial t} + \mathbf{v}_1\cdot\frac{\partial}{\partial\mathbf{r}_1} + (\mathbf{K}^{ext}+\mathbf{K}_1^m)\cdot\frac{\partial}{\partial\mathbf{v}_1}\Big]f_1 = \frac{N}{V}\int dX_2\mathbf{K}_2^m\frac{\partial f_2}{\partial\mathbf{v}_2}$$

One can show that a term of order $s+1$ is $\epsilon = (n_e\lambda_D^3)^{-1}$ times smaller than a term of order s. Since ϵ is usually very small in a plasma, one can state that correlation effects of particles over a distance langer than the debye length are negligible compared to correlations within a debye sphere.

8.3 Vlasov Equation

Due to the smallness of ϵ one can expand $f_{\alpha,s}$ in a product of single particle distribution functions plus a term f order ϵ that describes correlations. In 0-th order one derives after some manipulation Vlasov's equation:

$$\frac{df_\alpha}{dt} = \frac{\partial f_\alpha}{\partial t} + \mathbf{v}\frac{\partial f_\alpha}{\partial \mathbf{r}} + \frac{Z_\alpha e}{m_\alpha}\Big[\mathbf{E}(\mathbf{r},t) + \frac{\mathbf{v}}{c}\times\mathbf{B}(\mathbf{r},t)\Big]\frac{\partial f_\alpha}{\partial \mathbf{v}} = 0$$

where Maxwell's equations were used:

$$\nabla\times\mathbf{B} - \frac{1}{c}\frac{\partial \mathbf{E}}{\partial t} = \frac{4\pi}{c}\mathbf{j} \tag{169}$$

$$\nabla\times\mathbf{E} - \frac{1}{c}\frac{\partial \mathbf{b}}{\partial t} = 0 \tag{170}$$

$$\nabla\cdot\mathbf{B} = 0 \tag{171}$$

$$\nabla\cdot\mathbf{E} = 4\pi\varrho \tag{172}$$

with

$$\varrho^m(\mathbf{r},t) = \sum_\alpha eZ_\alpha n_\alpha \int f_{\alpha,1}(\mathbf{r},\mathbf{v},t)d\mathbf{v} \tag{173}$$

$$\mathbf{j}^m(\mathbf{r},t) = \sum_\alpha eZ_\alpha n_\alpha \int \mathbf{v} f_{\alpha,1}(\mathbf{r},\mathbf{v},t)d\mathbf{v} \tag{174}$$

$$\mathbf{E}(\mathbf{r},t) = \mathbf{E}^{ext}(\mathbf{r},t) + \sum_{\alpha,i}\int \mathbf{E^t}_{\alpha,i}(\mathbf{r},t|\mathbf{r}_{\alpha,i}(t))f_{\alpha,i}(\mathbf{r}_{\alpha,i},\mathbf{v}_{\alpha,i},t)d\mathbf{r}_{\alpha,i}d\mathbf{v}_{\alpha,i} \tag{175}$$

$$\mathbf{B}(\mathbf{r},t) = \mathbf{B}^{ext}(\mathbf{r},t) + \sum_{\alpha,i}\int \mathbf{B^t}_{\alpha,i}(\mathbf{r},t|\mathbf{r}_{\alpha,i}(t))f_{\alpha,i}(\mathbf{r}_{\alpha,i},\mathbf{v}_{\alpha,i},t)d\mathbf{r}_{\alpha,i}d\mathbf{v}_{\alpha,i} \tag{176}$$

Due to the fact that the entropy density of f_α is constant, Vlasov's equation cannot describe collision or dissipation effects. Nevertheless it can be shown ([21]) that the linearised version provides an appropriate formulation for waves with small amplitudes in plasmas.

If correlation terms of 1. order (i.e. collisions between particles) are taken into account, one can derive the Fokker-Planck equation.

8.4 Guiding Centre Transformation

There are several approaches to carry out the transformation to guiding centre coordinates. The most formal one would be the Lie-transform-technique ([11],[9]), which allows a rigorous proceeding up to all orders. Since for a straightforward guiding centre transformation the Lie method would be too laborious, we follow here a different, more physical approach [8],[20]. The same results but derived in a different way can also be found in [13](S.36-40).

At first we define:

$$\mathbf{v}_{a0} = \mathbf{v}_{a0\perp} + v_{a0\parallel}\mathbf{b}; \quad \mathbf{v}_{a0\perp} = -v_{a0\perp}(\sin\theta_a \mathbf{e}_1 + \cos\theta_a \mathbf{e}_2); \quad \mu_{a0} = \frac{m_a v_{a0\perp}^2}{2B_0}$$

The particle's position is also decomposed into an averaged and and into oszillating part:

$$\mathbf{x}_a = \mathbf{X}_a + \epsilon\boldsymbol{\varrho}_{a0} - \mathcal{O}(\epsilon^2) = \mathbf{X}_a + \epsilon\frac{\mathbf{b}\times\mathbf{v}_{a0}}{\Omega_a} - \mathcal{O}(\epsilon^2); \qquad \Omega_a = \frac{e_a B_0}{m_a c} \tag{177}$$

For the other coordinates we have:

$$U_a = v_{a0\parallel} + \mathcal{O}(\epsilon); \qquad \mu_a = \mu_{a0} + \mathcal{O}(\epsilon); \qquad \xi_a = \theta_a + \mathcal{O}(\epsilon) \tag{178}$$

Now we insert these results in the Lagrangian:

$$\begin{aligned} L_{a0} = &\left(m_a(\mathbf{v}_{a0\perp} + v_{a0\parallel}\mathbf{b}) + \frac{e_a}{c}[\mathbf{A}_0(\mathbf{X}_a) + \boldsymbol{\varrho}_{a0}\cdot\nabla\mathbf{A}_0(\mathbf{X}_a)]\right) \\ &\cdot(\dot{\mathbf{X}}_a + \frac{d}{dt}\boldsymbol{\varrho}_{a0}) - \frac{1}{2}m_a|\mathbf{v}_{a0\perp} + v_{a0\parallel}\mathbf{b}|^2 \end{aligned} \tag{179}$$

Line (179) is now sorted order by order:
the term $\mathbf{A}_0(\mathbf{X}_a)\cdot\dot{\mathbf{X}}_\mathbf{a}$ is the only one of order $\mathcal{O}(\epsilon)^{-1}$. The following is of order $\mathcal{O}(\epsilon)^0$:

$$m_a(\mathbf{v}_{a0\perp} + v_{a0\parallel}\mathbf{b})\cdot\dot{\mathbf{X}}_a + \frac{e_a}{c}\boldsymbol{\varrho}_{a0}\cdot\nabla\mathbf{A}_0(\mathbf{X}_a)\cdot\mathbf{X}_a + \frac{d}{dt}\boldsymbol{\varrho}_{a0}\cdot\frac{e_a}{c}\mathbf{A}_0 \tag{180}$$

Now we use a general property of Lagrangians: the equations of motions derived from a Lagrangian are invariant under a transformation of the the form $L \to L + dS/dt$. Here, S an arbitrary scalar (gauge transformation, see [11]). If we choose S as:

$$S_0 = -\frac{e_a}{c}\boldsymbol{\varrho}_{a0}\cdot\mathbf{A}_0, \tag{181}$$

all gyrophase dependent terms of this order vanish. With

$$\frac{dS}{dt} = -\frac{e_a}{c}\left(\frac{d}{dt}\boldsymbol{\varrho}_{a0}\right)\cdot\mathbf{A}_0 - \frac{e_a}{c}\boldsymbol{\varrho}_{a0}\cdot\left(\dot{\mathbf{X}}_a\cdot\nabla\mathbf{A}_0\right) \tag{182}$$

and

$$\Omega_a \mathbf{b} \times \boldsymbol{\varrho}_{a0} = \mathbf{b} \times (\mathbf{b} \times \mathbf{v}_{a0\perp}) = -\mathbf{v}_{a0\perp} \tag{183}$$

equations (180) and (182) result in:

$$\begin{aligned}
&\frac{e_a}{c}\Big[\boldsymbol{\varrho}_{a0} \cdot (\nabla \mathbf{A}_0 \cdot \dot{\mathbf{X}}_a - \dot{\mathbf{X}}_a \cdot \nabla \mathbf{A}_0)\Big] + m_a(\Omega_a \boldsymbol{\varrho}_{a0} \times \mathbf{b}) \cdot \dot{\mathbf{X}}_a + m_a v_{a0\|} \mathbf{b} \cdot \dot{\mathbf{X}}_a \\
&\quad = \frac{e_a}{c} \boldsymbol{\varrho}_{a0} \cdot (\dot{\mathbf{X}}_a \times \mathbf{B}_0) - \frac{e_a B_0}{m_a c} m_a \mathbf{b} \times \boldsymbol{\varrho}_{a0} \cdot \dot{\mathbf{X}}_a + m_a v_{a0\|} \mathbf{b} \cdot \dot{\mathbf{X}}_a \\
&\quad = m_a v_{a0\|} \mathbf{b} \cdot \dot{\mathbf{X}}_a
\end{aligned}$$

Now we consider $\mathcal{O}(\epsilon)$ of (179):

$$\frac{e_a}{c} \boldsymbol{\varrho}_{a0} \nabla \mathbf{A}_0 \cdot \dot{\boldsymbol{\varrho}}_{a0} + m_a \mathbf{v}_{a0\perp} \cdot \dot{\boldsymbol{\varrho}}_{a0} \tag{184}$$

Choosing

$$S_1 = -\boldsymbol{\varrho}_{a0} \cdot \nabla \mathbf{A} \cdot \boldsymbol{\varrho}_{a0} \tag{185}$$

only the term

$$\frac{1}{2} \frac{e_a}{c} (\boldsymbol{\varrho}_{a0} \times \mathbf{B}_0) \cdot \dot{\boldsymbol{\varrho}}_{a0} \tag{186}$$

survives. We use

$$\boldsymbol{\varrho}_{a0} \times \mathbf{b} = \frac{\mathbf{b} \times \mathbf{v}_{a0\perp}}{\Omega_a} \times \mathbf{b} = \frac{\mathbf{v}_{a0\perp}}{\Omega_a} \tag{187}$$

and

$$\dot{\boldsymbol{\varrho}}_{a0} = \frac{d}{dt}\Big(\frac{\mathbf{b} \times \mathbf{v}_{a0\perp}}{\Omega_a}\Big) = \frac{\mathbf{v}_{a0\perp}}{\Omega_a} \dot{\xi}_a \tag{188}$$

to derive finally:

$$\frac{m_a c}{e_a} \mu_{a0} \dot{\xi}_a \tag{189}$$

We substitute U_a for $v_{a0\|}$ and μ_a for μ_{a0} (178) to obtain for the Lagrangian:

$$L_a = \Big[\frac{e_a}{c} \mathbf{A}_0(\mathbf{X}_a) + m_a U_a \mathbf{b}(\mathbf{X}_a)\Big] \cdot \dot{\mathbf{X}}_a + \frac{m_a c}{e_a} \mu_a \dot{\xi}_a - \frac{1}{2} m_a U_a^2 - \mu_a B_0(\mathbf{X}_a) \tag{190}$$

This Lagrangian is now completely written in guiding-centre-coordinates and furthermore independent from ξ. That means that $\partial L / \partial \dot{\xi} \sim \mu_a$ is a constant of the motion.
Here, the first order transformation in finished. For the next oder just the result is presented:

$$L_a = \epsilon^{-1} \frac{e_a}{c} \mathbf{A}_a^*(\mathbf{X}_a, U_a, \mu_a) \cdot \dot{\mathbf{X}}_a + \epsilon \frac{m_a c}{e_a} \mu_a \dot{\xi}_a - H_{a0}(\mathbf{X}_a, U_a, \mu_a) \tag{191}$$

with

$$\mathbf{A}_a^*(\mathbf{X}_a, U_a, \mu_a) = \mathbf{A}_0(\mathbf{X}_a) + \epsilon \frac{m_a c}{e_a} U_a \mathbf{b}(\mathbf{X}_a) - \epsilon^2 \frac{m_a c^2}{e_a^2} \mu_a \mathbf{W}(\mathbf{X}_a) \tag{192}$$

and

$$H_{a0}(\mathbf{X}_a, U_a, \mu_a) = \frac{1}{2} m_a U_a^2 + \mu_a B_0(\mathbf{X}_a) \tag{193}$$

and

$$\mathbf{W}(\mathbf{X}_a) = [\nabla \mathbf{e}_1(\mathbf{X}_a)] \cdot \mathbf{e}_2(\mathbf{X}_a) + \frac{1}{2} \mathbf{b}(\mathbf{X}_a) \mathbf{b}(\mathbf{X}_a) \cdot [\nabla \times \mathbf{b}(\mathbf{X}_a)] \tag{194}$$

Now also the Poisson brackets are calculated: In order to do so, we make use of the following rule ([10], [14] und [2]):

$$\begin{aligned} \Big\{ F, G \Big\} &= \frac{e}{mc} \Big(\frac{\partial F}{\partial \xi} \frac{\partial G}{\partial \mu} - \frac{\partial G}{\partial \xi} \frac{\partial F}{\partial \mu} \Big) \\ &- \frac{e\mathbf{b}}{eB_\parallel^*} \Big[\Big(\nabla F + \mathbf{W} \frac{\partial F}{\partial \xi} \Big) \times \Big(\nabla G + \mathbf{W} \frac{\partial G}{\partial \xi} \Big) \Big] \\ &+ \frac{\mathbf{B}^*}{mB_\parallel^*} \Big[\Big(\nabla F + \mathbf{W} \frac{\partial F}{\partial \xi} \Big) \frac{\partial G}{\partial U} - \Big(\nabla G + \mathbf{W} \frac{\partial G}{\partial \xi} \Big) \frac{\partial F}{\partial U} \Big] \end{aligned}$$

Applying this relation results in:

$$\Big\{ \mathbf{X}_a, \mathbf{X}_a \Big\} = \epsilon \frac{c}{e_a B_{a\parallel}^*} \mathbf{b} \times \mathbf{I}; \qquad \Big\{ \mathbf{X}_a, U_a \Big\} = \frac{\mathbf{B}_a^*}{m_a B_{a\parallel}^*}; \tag{195}$$

$$\Big\{ \mathbf{X}_a, \xi_a \Big\} = \epsilon \frac{c}{e_a B_{a\parallel}^*} \mathbf{b} \times \mathbf{W}; \qquad \Big\{ U_a, \xi_a \Big\} = -\frac{\mathbf{B}_a^* \cdot \mathbf{W}}{m_a B_{a\parallel}^*}; \tag{196}$$

$$\Big\{ \xi_a, \mu_a \Big\} = \epsilon^{-1} \frac{e_a}{m_a c} \tag{197}$$

Here $\mathbf{I}$ represents the unit tensor, $\mathbf{B}_a^* \equiv \nabla \times \mathbf{A}_a^*$ and $B_{a\parallel}^* \equiv \mathbf{B}_a^* \cdot \mathbf{b}$.
For completeness the Poisson brackets for another set of equations in given here, following reference [15]: with

$$\mathbf{Z} = (\mathbf{X}, H_0, \mu, \xi) \tag{198}$$

and the definition

$$\mathbf{V}_d \equiv \frac{cmU}{eB} \nabla \times U\mathbf{b} \tag{199}$$

the bracktes for two arbitrary functions read:

$$\begin{aligned} \{F, G\} &= \frac{mc}{eB} \Big[\frac{\partial F}{\partial \xi} \Big(\frac{\partial G}{\partial H_0} + \frac{1}{B} \frac{\partial G}{\partial \mu} \Big) - \frac{\partial G}{\partial \xi} \Big(\frac{\partial F}{\partial H_0} + \frac{1}{B} \frac{\partial F}{\partial \mu} \Big) \Big] \\ &+ (U\mathbf{b} + \mathbf{V}_d) \cdot \Big(\nabla F \frac{\partial G}{\partial H_0} - \frac{\partial F}{\partial H_0} \nabla G \Big) - \frac{c\mathbf{b}}{eB} \cdot (\nabla F \times \nabla G) \end{aligned} \tag{200}$$

8.5 Lie Transforms

Here a short introduction to the Lie transform following [11] is given. Let $\mathbf{Q}$ be a vector field on M with coordinates Z^i. It is represented by:

$$\frac{dZ^i}{dt} = Q^i(Z) = \sum_{k=0}^{\infty} \epsilon^k Q_k^i(Z) \tag{201}$$

Let the system have a solution in 0.order in the sense that the solution of Q can be approximated by Q_0. The basic idea of the perturbation theory is now, to find a coordinate transform that results in simplified equations (compared to the original ones).
Let Z be a point in M that is mapped to $\bar{Z}$ by $T : M \to M$: $TZ = \bar{Z}$.
A vector field $\mathbf{Q}$ is mapped by the tangential mapping T_*:

$$\bar{\mathbf{Q}} = T_* \mathbf{Q}; \quad \text{resp.} \quad \bar{Q}^i(\bar{Z}) = \frac{\partial \bar{Z}^i}{\partial Z^j} Q^j(Z) \tag{202}$$

When scalars are transformed, they are considered as 0-forms in M which are pulled back to $\mathcal{R}$ by the transformation T^* . T^* works in the opposite direction than T. That is why the inverse of T^* has to be used:

$$\bar{s} = T^{*-1} s \tag{203}$$

Especially interesting scalars are the coordinate functions $Z^i = I^i(Z)$ with Z^i being the coordinate of Z. Therefore, $\bar{Z} = TZ$ changes into:

$$\bar{Z}^i = I^i(\bar{Z}) = I^i(TZ) = T^* I^i(Z) \tag{204}$$

The class of transformations that can be represented by an exponential function of a vector field, is called Lie-transformations:

$$T^\epsilon = \exp(\epsilon \mathbf{G}) \tag{205}$$

$\mathbf{G}$ is called the generating function of the transformation. The tangential mapping T_*^ϵ can also be represented by an exponential function:

$$T_*^\epsilon = \exp(-\epsilon L_G) \tag{206}$$

with

$$(L_{\mathbf{G}} \mathbf{X})^i = G^j X^i_{,j} - X^j G^i_{,j} \tag{207}$$

$(L_{\mathbf{G}} \mathbf{X})^i$ is called Lie-derivative. A 1-form transforms like a scalar:

$$\bar{\gamma} = T^{*-1} \gamma + dS$$

To go to higher order, a series of transformations (for each order separately) is applied:

$$T_n^{*-1} = ...T_3^{*-1}T_2^{*-1}T_1^{*-1} = \\ ... \cdot \exp(\epsilon^3 L_3) \cdot \exp(\epsilon^2 L_2) \cdot \exp(\epsilon L_1) = 1 + \epsilon L_1 + \epsilon^2(L_1^2 - L_2) + ... \quad (208)$$

Now also γ and S are expanded in ϵ, i.e. $\gamma = \sum \epsilon^n \gamma_n, \bar{\gamma} = \sum \epsilon^n \bar{\gamma}_n$ and $S = \sum \epsilon^n S_n$. Ordered by powers of ϵ this is:

$$\bar{\gamma}_0 = \gamma_0 + dS_0 \quad (209)$$

$$\bar{\gamma}_1 = \gamma_1 - L_1\gamma_0 + dS_1 \quad (210)$$

$$\bar{\gamma}_2 = \gamma_2 - L_1\gamma_1 + \frac{1}{2}(L_1^2 - 2L_2)\gamma_0 + dS_2 \quad (211)$$

Furthermore, it can be shown that the Lie-derivatives for the γs can be written in the following form (details in [11], p.746):

$$(L_n\gamma)_i = G_n^j\left(\frac{\partial\gamma_i}{\partial z^j} - \frac{\partial\gamma_j}{\partial z^i}\right) \quad (212)$$

8.6 Gyrocentre Transformation

The ξ_a-dependence has to be removed from H_{a1} and H_{a2}, order by order.
Following references [14],[20], we use the correlated one-form, starting in guiding centre coordinates:

$$\gamma_{a0} = \hat{\gamma}_{a0} - H_{a0}dt = \frac{e_a}{c}\mathbf{A}_a^* \cdot d\mathbf{X}_a + \epsilon\frac{m_a c}{e_a}\bar{\mu}_a d\xi_a - H_{a0}dt \tag{213}$$

with $\hat{\gamma}_{a0}$ being the symplectic part of γ. The perturbed part is (33):

$$\gamma_{a1} = \hat{\gamma}_{a1} - H_{a1}dt = 0 - e_a\Big(\phi_1(\bar{\mathbf{X}}_a + \boldsymbol{\varrho}_a, t) - \frac{1}{c}\mathbf{A}_1(\bar{\mathbf{X}}_a + \boldsymbol{\varrho}_a, t)\cdot\mathbf{v}_{a0}(\mathbf{Z}_a)\Big)dt \tag{214}$$

Here the transform

$$\mathbf{x}_a = \bar{\mathbf{X}}_a + \bar{\boldsymbol{\varrho}}_{a0} + \mathcal{O}(\epsilon) \tag{215}$$

with

$$\bar{\boldsymbol{\varrho}}_{a0} = \boldsymbol{\varrho}_{a0}(\bar{\mathbf{Z}}_a) = \mathbf{b}(\bar{\mathbf{X}}_a)\times\mathbf{v}_{a0}(\bar{\mathbf{Z}}_a)/\Omega_a(\bar{\mathbf{X}}_a), \quad \Omega_a(\bar{\mathbf{X}}_a) = \frac{e_a B(\bar{\mathbf{X}}_a)}{m_a c} \tag{216}$$

is employed, to write the fields in the new coordinates. Clearly, it maps back the gyrocentre positions to the physical position, since we have to evaluate the fields at the real position of the particle. A detailed mathematical treatment of this pull-back-transformation can be found in Qin's works ([1]-[4]). The justification for line (215) is given later with equation (44). We start with the transformation for the first order using equation (210):

$$\bar{\gamma}_1 = \bar{\hat{\gamma}}_1 - \bar{H}_{a1}dt = \hat{\gamma_1} - H_{a1}dt - L_1(\hat{\gamma}_0 - H_{a0}dt) + dS_1 \tag{217}$$

The symplectic part, also $\bar{\hat{\gamma}}$ has to be unperturbed and consequently $\bar{\hat{\gamma}_1} = 0$. With the choice of $\mathbf{v}_{a0}$, also $\hat{\gamma_1}$ already vanishes (equation 214):

$$0 \stackrel{!}{=} 0 - L_1\hat{\gamma}_0 + dS_1 \tag{218}$$

This is used to determine the generating functions G (see eq. (212)):

$$(L_1\gamma_0)_{\mathbf{X}_a} = \Big[G^{X_{aj}}\Big(\frac{\partial\mathbf{A}_i^*}{\partial X_{aj}} - \frac{\partial\mathbf{A}_j^*}{\partial X_{ai}}\Big) + G^{U_a}\frac{m_a c}{e_a}\mathbf{b}(\mathbf{X}_a)\Big] \tag{219}$$

$$(L_1\gamma_0)_{U_a} = -G^{\mathbf{X}_a}m_a\mathbf{b} \tag{220}$$

$$(L_1\gamma_0)_{\mu_a} = -G^{\xi}\frac{m_a c}{e_a}; \quad G^{\mathbf{X}_a}\frac{m_a c}{e_a}\mathbf{W}(\mathbf{X}_a) \sim \mathcal{O}(\epsilon^2) \tag{221}$$

$$(L_1\gamma_0)_{\xi_a} = G^{\mu_a}\frac{m_a c}{e_a} \tag{222}$$

$$(L_1\gamma_0)_t = -G^{\mathbf{X}_a}\frac{\partial H_{a0}}{\partial\mathbf{X}_a} - G^{\mu}B_0 - G^{U_a}m_a U_a \tag{223}$$

Taking into account

$$dS_1 = \nabla S_1 \cdot \mathbf{X}_a + \frac{\partial S_1}{\partial U_a} dU_a + \frac{\partial S_1}{\partial \mu_a} d\mu_a + \frac{\partial S_1}{\partial \xi_a} d\xi_a + \frac{\partial S_1}{\partial t} dt \tag{224}$$

and choosing

$$G^t = 0 \tag{225}$$

i.e., leaving the time variable unchanged, one calculates for G:

$$G^{\mu_a} = \frac{e_a}{m_a c} \frac{\partial S_1}{\partial \xi_a} \tag{226}$$

$$G^{\xi_a} = -\frac{e_a}{m_a c} \frac{\partial S_1}{\partial \mu_a} \tag{227}$$

$$G^{U_a} = -\frac{e_a}{m_a c} \nabla S_1 \cdot \mathbf{b}^* \tag{228}$$

$$G^{\mathbf{x}_a} = = -\frac{c}{e_a B_\parallel^*} \mathbf{b} \times \nabla S_1 - \frac{\mathbf{B}^*}{m_a B_\parallel^*} \frac{\partial S_1}{\partial U_a} \tag{229}$$

So equation (217) reduces to:

$$\bar{H}_{a1} = H_{a1} - G^{\mathbf{x}_a} \frac{\partial H_{a0}}{\partial \mathbf{X}_a} - G^{\mu} B_0 - G^{U_a} m_a U_a - \frac{\partial S_1}{\partial t} \tag{230}$$

Now there is still one degree of freedom: since $\bar{H}_{a1}$ has to be independent of the gyrophase, one chooses for it the ξ_a-averaged H_{a1}-value:

$$\bar{H}_{a1} = \langle e_a \phi_1(\bar{\mathbf{X}}_a + \bar{\boldsymbol{\varrho}}_{a0}, t) - \frac{e_a}{c} \mathbf{v}_{ao} \cdot \mathbf{A}_1(\bar{\mathbf{X}}_a + \bar{\boldsymbol{\varrho}}_{a0}, t) \rangle \tag{231}$$

$\langle ... \rangle$ means the gyrophase average operation $1/2\pi \int_0^{2\pi} ... d\xi$.

Inserting the relations for the G's, we obtain the following expression for the gauge function S_1:

$$\begin{aligned} &\epsilon_B^{-1} \Omega_a \frac{\partial S_1}{\partial \xi_a} + \frac{\partial S_1}{\partial t} + \\ &\quad \epsilon_B \left(\frac{\bar{U}_a}{m_a} \mathbf{b}^* \cdot \frac{\partial S_1}{\partial \bar{\mathbf{X}}_a} - [\frac{c}{e B_\parallel^*} \mathbf{b} \times \frac{\partial S_1}{\partial \bar{\mathbf{X}}_a} + \frac{\mathbf{B}^*}{m_a B_\parallel^*} \frac{\partial S_1}{\partial U_a}] \cdot \frac{\partial H_{a0}}{\partial \bar{\mathbf{X}}_a} \right) \\ &\quad = e_a \tilde{\phi}_1(\bar{\mathbf{X}}_a + \boldsymbol{\varrho}_0, t) - \frac{e_a}{c} \bar{\mathbf{v}}_{a0} \widetilde{\cdot \mathbf{A}_1}(\bar{\mathbf{X}}_a + \boldsymbol{\varrho}_0, t) = \tilde{\psi}_a(\bar{\mathbf{Z}}_a, t) \end{aligned} \tag{232}$$

with

$$\begin{aligned} \tilde{\phi}_1(\bar{\mathbf{X}}_a + \epsilon_B \bar{\boldsymbol{\varrho}}_a, t) &= \phi_1(\bar{\mathbf{X}}_a + \epsilon_B \bar{\boldsymbol{\varrho}}_a, t) - \langle \phi_1(\bar{\mathbf{X}}_a + \epsilon_B \bar{\boldsymbol{\varrho}}_a, t) \rangle \\ \bar{\mathbf{v}}_{a0} \widetilde{\cdot \mathbf{A}_1}(\bar{\mathbf{X}}_a + \epsilon_B \bar{\boldsymbol{\varrho}}_a, t) &= \bar{\mathbf{v}}_{a0} \cdot \mathbf{A}_1(\bar{\mathbf{X}}_a + \epsilon_B \bar{\boldsymbol{\varrho}}_a, t) - \langle \bar{\mathbf{v}}_{a0} \cdot \mathbf{A}_1(\bar{\mathbf{X}}_a + \epsilon_B \bar{\boldsymbol{\varrho}}_a, t) \rangle \\ \tilde{\psi}_a(\bar{\mathbf{Z}}_a, t) &= e_a \tilde{\phi}_1(\bar{\mathbf{X}}_a + \epsilon_B \bar{\boldsymbol{\varrho}}_a, t) - \frac{e_a}{c} \bar{\mathbf{v}}_{a0} \widetilde{\cdot \mathbf{A}_1}(\bar{\mathbf{X}}_a + \epsilon_B \bar{\boldsymbol{\varrho}}_a, t) \end{aligned}$$

The expression for S_1 can be used to write the coordinate transform more explicit:

$$\bar{\mathbf{X}}_a = \mathbf{X}_a + \Delta\{S_1(\mathbf{X}_a), \mathbf{X}_a\} + \mathcal{O}(\Delta)^2 \tag{233}$$

Here the gyrocentre transformation for the first order is finished. Since in later chapters we only use the linearised equations, the second order transformation is not carried out in further detail here (for second order treatment see[5] and [14]).

8.7 Useful Formulae

$$\mathbf{v}\times\nabla\times\mathbf{A}=\epsilon_{ijk}v_j\epsilon_{klm}\delta_l A_m=(\delta_{il}\delta_{jm}-\delta_{im}\delta_{jl})v_j\delta_l A_m$$
$$=(\delta_i A_j-\delta_j A_i)v_j=(\nabla\mathbf{A})\mathbf{v}-(\nabla\mathbf{A})^T\mathbf{v}=(\nabla\mathbf{A})\mathbf{v}-\mathbf{v}(\nabla\mathbf{A})$$

Following relations are useful for performing the velocity space integrals. For a Maxwellian F_0:

$$\begin{aligned}F_0 &= \frac{n_0(r)}{(2\pi T(r)/m)^{3/2}}e^{-mv^2/2T(r)}=\frac{n_0(r)}{\pi^{3/2}v_{th}^3}e^{-v^2/v_{th}^2}\\ &= \frac{n_0(r)}{\pi^{3/2}v_{th}^3}e^{-(U^2+v_\perp^2)/v_{th}}=\frac{n_0(r)}{\pi^{3/2}v_{th}^3}e^{-U^2/v_{th}^2}e^{-\mu B/T(r)}\end{aligned}$$

$$\nabla F_0=F_0\frac{\nabla n}{n}\Big[1+\eta(\frac{E}{T}-\frac{3}{2})\Big]$$

$$\hat{F}_0=\frac{n_0(r)}{\pi^{3/2}v_{th}^3}e^{-U^2/v_{th}^2}$$

$$\nabla\hat{F}_0=\hat{F}_0\frac{\nabla n}{n}\Big[1+\eta(\frac{mU^2}{2T}-\frac{3}{2})\Big]$$

$$\int|\nabla\hat{F}_0|2\pi dU=\frac{|\nabla n|m}{T}[1-\eta]$$

$$\frac{\partial F_0}{\partial E}=-\frac{F_0}{T}$$

$$d^3\mathbf{v}=2\pi v_\perp dv_\perp dU=2\pi\frac{B}{m}d\mu dU$$

$$\int F_0 d^3\mathbf{v}=n_0(r)$$

$$\int\mu F_0 d^3\mathbf{v}=n_0(r)T(r)/B$$

$$\int mU^2F_0d^3\mathbf{v}=n_0(r)T(r)$$

$$\int\mu B\frac{\partial F_0}{\partial E}d^3\mathbf{v}=-n_0(r)$$

$$\int mU^2\frac{\partial F_0}{\partial E}d^3\mathbf{v}=-n_0(r)$$

Integrals involving Bessel functions:

$$\begin{aligned}\chi &\equiv \frac{v_{th}^2k_\perp^2}{2\Omega^2}\\ \int_0^\infty J_0(\frac{v_\perp k_\perp}{\Omega})^2e^{-v_\perp^2/v_th^2}v_\perp dv_\perp &= \frac{v_{th}^2e^{-\chi}I_0(\chi)}{2}\\ \int_0^\infty J_0(\frac{v_\perp k_\perp}{\Omega})^2e^{-v_\perp^2/v_th^2}v_\perp^3 dv_\perp &= \frac{v_{th}^4e^{-\chi}[(1-\chi)I_0(\chi)+\chi I_1(\chi)]}{2}\end{aligned}$$

$$\int \mu B J_0(k_\perp v_\perp/\Omega)^2 \frac{\partial F_0}{\partial E} d^3\mathbf{v} = \int \mu B J_0\Big(\frac{k_\perp}{\Omega}\sqrt{2\mu B/m}\Big)^2 \frac{\partial F_0}{\partial E} d^3\mathbf{v} = -n_0(r)\Big\{e^{-\chi}\Big[\chi I_1(\chi)+(1-\chi)I_0(\chi)\Big]\Big\}$$

$$\int mU^2 J_0(k_\perp v_\perp/\Omega)^2 \frac{\partial F_0}{\partial E} d^3\mathbf{v} = -n_0(r)e^{-\chi}I_0(\chi)$$

$$\int J_0(k_\perp v_\perp/\Omega)^2 \frac{\partial F_0}{\partial E} d^3\mathbf{v} = -n_0(r)e^{-\chi}I_0(\chi)/T(r)$$

$$\int mU^2 J_0(k_\perp v_\perp/\Omega)^2 F_0 d^3\mathbf{v} = n_0(r)T(r)e^{-\chi}I_0(\chi)$$

$$\int \mu B J_0(k_\perp v_\perp/\Omega)^2 F_0 d^3\mathbf{v} = n_0(r)T(r)\Big\{e^{-\chi}\Big[\chi I_1(\chi) + (1-\chi)I_0(\chi)\Big]\Big\}$$

Expansion of Bessel functions:

$$J_0(x) = 1 - \frac{x^2}{4} + \frac{x^4}{64} \tag{234}$$

$$1 - J_0(x)^2 = \frac{x^2}{2} - \frac{3x^4}{32} \tag{235}$$

8.8 Equilibrium

We skip the proof of the existence of magnetic flux surfaces, shaped in toroidal form ([49]) and start instead directly with the equations describing an MHD equilibrium of an isotropic plasma :

$$\mathbf{j} \times \mathbf{B} = \nabla p \tag{236}$$

$$\nabla \times \mathbf{B} = \mu_0 \mathbf{j} \tag{237}$$

$$\nabla \cdot \mathbf{B} = 0 \tag{238}$$

It immediately follows from $\mathbf{B} \cdot \nabla p = 0$ and $\mathbf{j} \cdot \nabla p = 0$ that there is no pressure gradient along the field lines and that the current lines lie on magnetic surfaces. These nested surfaces are counted by some label χ that is usually chosen to be proportional to the poloidal flux:

$$\Psi_P = \frac{1}{2\pi} \int_V d^3x \mathbf{B} \cdot \nabla\theta \equiv 2\pi\chi \tag{239}$$

Similarly, the toroidal flux is defined as

$$\Psi_T = \frac{1}{2\pi} \int_V d^3x \mathbf{B} \cdot \nabla\zeta \tag{240}$$

Now we can define the safety factor q:

$$q \equiv \frac{d\Psi_T}{d\Psi_P} = \frac{\mathbf{B} \cdot \nabla\zeta}{\mathbf{B} \cdot \nabla\theta} = \frac{d\zeta}{d\theta} \tag{241}$$

8.8.1 General 2D Flux Coordinate Representation

It can be shown that a general magnetic field can be written in terms of these fluxes as:

$$\mathbf{B} = \frac{1}{2\pi}\Big(\nabla\zeta \times \nabla\Psi_P + \Psi_T \times \nabla\theta\Big) = \nabla\chi \times \nabla(q\theta - \zeta) \tag{242}$$

Coordinates that allow $\mathbf{B}$ to be represented in this form, are called flux coordinates. Obviously, there is still a degree of freedom: any transform $(\chi, \theta, \zeta) \rightarrow (\chi', \theta', \zeta')$ that preserves the field line label $q\theta - \zeta = q\theta' - \zeta'$ results again in a set of flux coordinates. As special cases Hamada coordinates (Jacobian is chosen to be a flux label) and Boozer coordinates (straight field and current lines) are commonly used. In this work, we choose symmetry coordinates: the toroidal angle is simply defined as

$$\zeta = -\varphi \tag{243}$$

and the poloidal angle is chosen in a way that makes the field lines straight. In this coordinate system, both χ and θ are orthogonal to ζ, but χ and θ being non-orthogonal, resulting in the following metric tensor (covariant components):

$$g_{ij} = \begin{pmatrix} g_{11} & g_{12} & 0 \\ g_{21} & g_{22} & 0 \\ 0 & 0 & g_{33} \end{pmatrix}; \qquad J = Det(g_{ij}) = \sqrt{g} = \sqrt{(g_{11}g_{22} - g_{12}^2)g_{33}} \tag{244}$$

If the radius vector $\mathbf{r} = \mathbf{r}(x^1, x^2, x^3)$ is given by the curvilinear coordinates x^i then it follows that $d\mathbf{r} = dx^i \partial\mathbf{r}/\partial x^i$, and the line element $dl^2 \equiv (d\mathbf{r})^2$ can be written as:

$$dl^2 = g_{ik} dx^i dx^k \qquad \text{with} \qquad g_{ik} = \frac{\partial \mathbf{r}}{\partial x^i} \cdot \frac{\partial \mathbf{r}}{\partial x^k} \tag{245}$$

In symmetry coordinates one obtains:

$$dl^2 = g_{11} d\chi^2 + g_{22} d\theta^2 + g_{33} d\zeta^2 + 2g_{12} d\chi d\theta \tag{246}$$

Clearly, it follows from the toroidal arc length element $dl_\zeta = R d\zeta$ and the partial orthogonality that $g_{33} = R^2$.

Following [48], we do not choose χ directly as radial coordinate, but instead we take s defined by $s = \sqrt{\chi/\chi_1}$ and consequently $\nabla\chi = 2s\chi_1 \nabla s$ with $2\pi\chi_1$ representing the total poloidal flux. In these coordinates the radial component of Ampère's law (237) reads:

$$\mu_0 j^s = \frac{1}{J}\left(\frac{\partial B_\zeta}{\partial \theta} - \frac{\partial B_\theta}{\partial \zeta}\right) \tag{247}$$

Since j^s (consequence of the force balance) and $\partial B_\theta/\partial\zeta$ (toroidal symmetry) vanish, also $\partial B_\zeta/\partial\theta$ has to be zero and thus the covariant component $B_\zeta \equiv I(s)$ depends only on s. This leads to a 'mixed' form of $\mathbf{B}$ (both co- and contra-variant components appear):

$$\mathbf{B} = I(s)\nabla\zeta + \nabla\zeta \times \nabla\chi \tag{248}$$

Writing $\mathbf{B}$ in co- and contravariant components:

$$\begin{pmatrix} B_\chi \\ B_\theta \\ B_\zeta \end{pmatrix} = \begin{pmatrix} 2s\chi_1 g_{12}/J \\ 2s\chi_1 g_{22}/J \\ I(s) \end{pmatrix}; \qquad \begin{pmatrix} B^\chi \\ B^\theta \\ B^\zeta \end{pmatrix} = \begin{pmatrix} 0 \\ 2s\chi_1/J \\ I(s)/R^2 \end{pmatrix} \tag{249}$$

and comparing with line (242) - also written in components - provides a useful formula for the Jacobian:

$$\begin{pmatrix} B_\chi \\ B_\theta \\ B_\zeta \end{pmatrix} = \begin{pmatrix} 2s\chi_1 g_{12}/J \\ 2s\chi_1 g_{22}/J \\ 2s\chi_1 q(s) R^2/J \end{pmatrix}; \qquad \begin{pmatrix} B^\chi \\ B^\theta \\ B^\zeta \end{pmatrix} = \begin{pmatrix} 0 \\ 2s\chi_1/J \\ 2s\chi_1 q(s)/J \end{pmatrix} \tag{250}$$

$$\Rightarrow J = 2s\chi_1 q(s) R^2 / I(s) \tag{251}$$

Using representation (248) for $\mathbf{B}$ the current density is written as

$$\mathbf{j} = -\Delta^* \chi \nabla\zeta + \nabla I \times \nabla\zeta \tag{252}$$

with

$$\Delta^* = R^2 \nabla \cdot \frac{1}{R^2} \nabla. \tag{253}$$

We put this expression for $\mathbf{j}$ in the force balance equation to obtain the Grad-Shafranov-Schlüter equation:

$$\Delta^* \chi = -I \frac{dI}{d\chi} - \mu_0 R^2 \frac{dp}{d\chi} \tag{254}$$

If we specify the profiles I and p resp. II' and p' and the shape of the plasma boundary then we can solve for $\chi(R, Z)$. Using this result, the metric coefficients for the straight-field-line coordinate system s, θ, ζ can be determined.

8.8.2 Straight Circular Tokamak Geometry

This configuration is actually a cylindrical configuration, where the major radius R_0 is introduced by the toroidal wave vector $k_\zeta = n/R_0$. Thus there is no toroidal curvature and in case of circular flux surfaces the metric tensor reads:

$$g_{ij} = \begin{pmatrix} a^2 & 0 & 0 \\ 0 & a^2\varrho^2 & 0 \\ 0 & 0 & R_0^2 \end{pmatrix}; \tag{255}$$

Here, a stands for the radius of the plasma column and ϱ is employed as normalised radial variable. The magnetic field components in this geometry are:

$$\begin{pmatrix} B_\varrho \\ B_\theta \\ B_\zeta \end{pmatrix} = \begin{pmatrix} 0 \\ \varrho\chi'(\varrho)/R_0 \\ I(\varrho) \end{pmatrix}; \quad \begin{pmatrix} B^\varrho \\ B^\theta \\ B^\zeta \end{pmatrix} = \begin{pmatrix} 0 \\ \chi'(\varrho)/\varrho a^2 R_0 \\ I(\varrho)/R_0^2 \end{pmatrix} \tag{256}$$

This is again consistent with the definition of the poloidal flux (239)

$$\Psi_P = \frac{1}{2\pi} \int_V d^3x B^\theta = \frac{1}{2\pi} \int_0^\varrho d\varrho' \int_0^{2\pi} d\theta \int_0^{2\pi} d\zeta J dB^\theta = 2\pi\chi(\varrho) \tag{257}$$

The relation between $I(\varrho)$ and the constant and uniform magnetic field in ζ direction B_0 can be obtained when the covariant ζ-component of $\mathbf{B}$ is related to the physical ζ-component $\hat{B}_\zeta$:

$$B_0 = \hat{B}_\zeta = \sqrt{g_{33}} B^\zeta = \frac{I}{R_0} \tag{258}$$

The toroidal flux becomes

$$\Psi_T = \frac{1}{2\pi}\int_V d^3x B^\zeta = \pi a^2 \varrho^2 B_0 \tag{259}$$

and with the usual definition of $q = \Psi_T'/\Psi_P'$ one obtains the relation between q and $\hat{B}_\theta$:

$$q(\varrho) = \frac{a^2 \varrho B_0}{\chi'(\varrho)}; \qquad \Rightarrow \qquad \hat{B}_\theta = \frac{a\varrho B_0}{q(\varrho)R_0} \tag{260}$$

From this equation we can see clearly that in this geometry the coordinates (ϱ, θ, ζ) are flux coordinates. Finally, the Grad-Shafranov's equation reduces to

$$\mu_0 \frac{dp}{d\varrho} = \frac{a^2 B_0^2}{R_0^2 q^3}\varrho\Big[-2q + \varrho\frac{dq}{d\varrho}\Big] \tag{261}$$

Consequently, defining either a pressure or a q-profile completely determines a cylindrical equilibrium.

8.8.3 Concentric Circular Tokamak Geometry

The concentric circular Tokamak geometry is given by the definition of the magnetic field:

$$\mathbf{B} = \frac{B_0}{1+\epsilon\cos\theta}\Big(\hat{\mathbf{e}}_\zeta + \frac{a\varrho}{q(\varrho)R_0}\hat{\mathbf{e}}_\theta\Big), \qquad \epsilon \equiv \frac{a\varrho}{R_0} \tag{262}$$

With the metric tensor

$$g_{ij} = \begin{pmatrix} a^2 & 0 & 0 \\ 0 & a^2\varrho^2 & 0 \\ 0 & 0 & R_0^2(1+\epsilon\cos\theta)^2 \end{pmatrix}; \tag{263}$$

the magnetic field components are:

$$\begin{pmatrix} B_\varrho \\ B_\theta \\ B_\zeta \end{pmatrix} = \begin{pmatrix} 0 \\ \frac{a^2\varrho^2 B_0}{q(\varrho)R_0(1+\epsilon\cos\theta)} \\ B_0 R_0 \end{pmatrix}; \qquad \begin{pmatrix} B^\varrho \\ B^\theta \\ B^\zeta \end{pmatrix} = \begin{pmatrix} 0 \\ \frac{B_0}{q(\varrho)R_0(1+\epsilon\cos\theta)} \\ \frac{B_0 R_0}{R_0^2(1+\epsilon\cos\theta)^2} \end{pmatrix} \tag{264}$$

One immediately realises that in this case the coordinates (ϱ, θ, ζ) are flux coordinates only up to dominant order:

$$\frac{B^\zeta}{B^\theta} = \frac{\Psi_T'}{\Psi_P'} = \frac{q(\varrho)}{1+\epsilon\cos\theta} = q(\varrho)(1 - \epsilon\cos\theta + \epsilon^2\cos^2\theta - ...) \tag{265}$$

Consequently, also a flux coordinate representation like in equation (242) is only possible, if we introduce a θ-dependent 'toroidal flux', what, of course, disagrees with physical interpretation, but nevertheless allows a 'flux-like' representation of this configuration:

$$\Psi'_P = \frac{2\pi a^2 B_0 \varrho}{q(\varrho)} \qquad \Rightarrow \qquad \Psi'_T = \frac{2\pi a^2 B_0 \varrho}{1 + \epsilon \cos\theta} \tag{266}$$

Another problematic point was introduced by the assumption of unshifted concentric flux surfaces, what conflicts with Grad-Shafranov-Schlüter's equation: toroidal curvature shifts the centres of the flux surfaces outwards, caused firstly by the pressure, that tries to expand ('inflate') the torus and secondly by the hoop force originating from the toroidal plasma current. Consequently, the GSS equation again is only valid in the lowest order:

$$\mu_0 \frac{dp}{d\varrho} = \frac{a^2 B_0^2}{R_0^2 q^3} \varrho \Big[- q(1 + \frac{1}{1 + \epsilon \cos\theta}) + \varrho \frac{dq}{d\varrho} \Big] \tag{267}$$

8.8.4 Numerical Equilibria Information

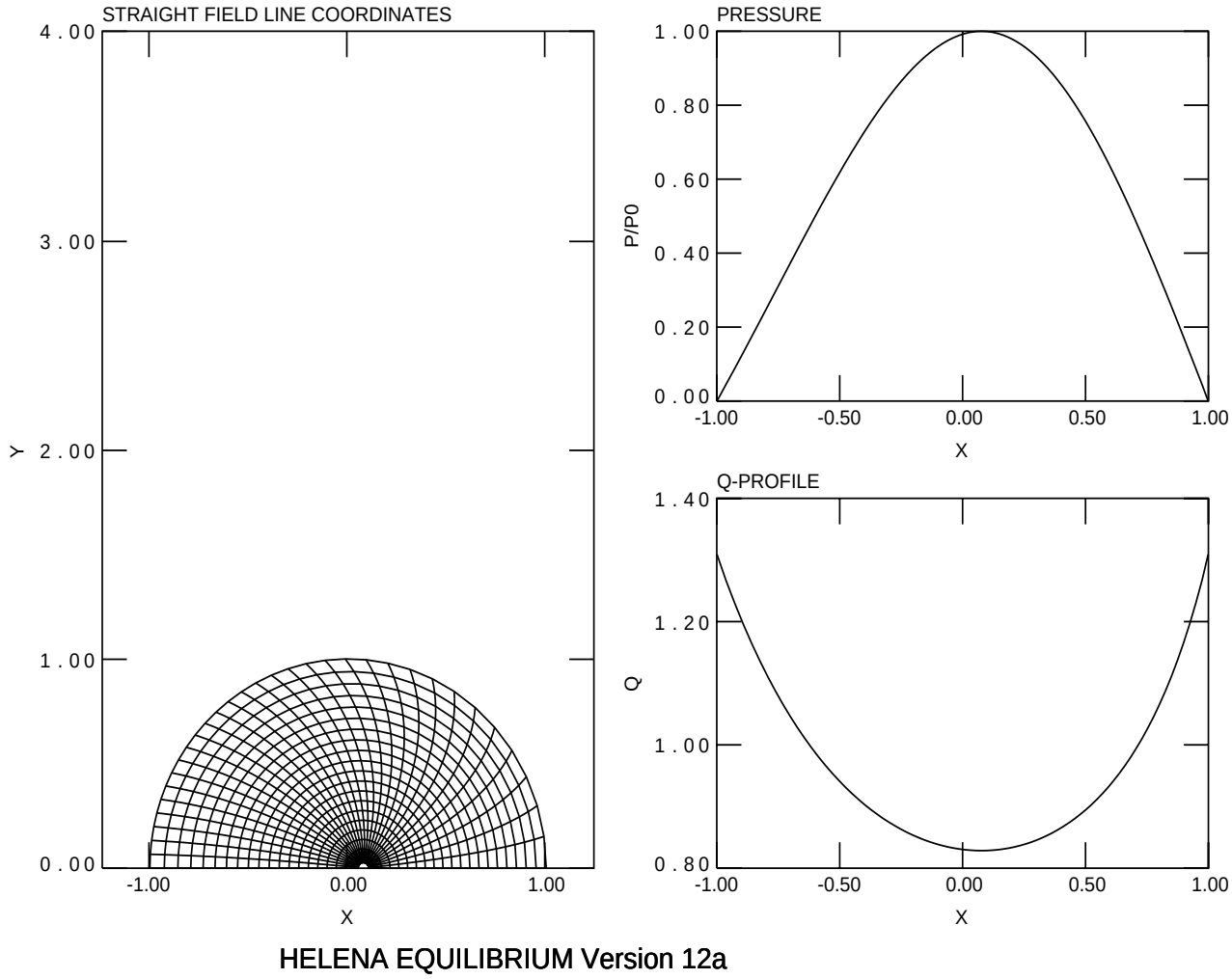

Figure 45: HELENA plot, equilibrium (I)

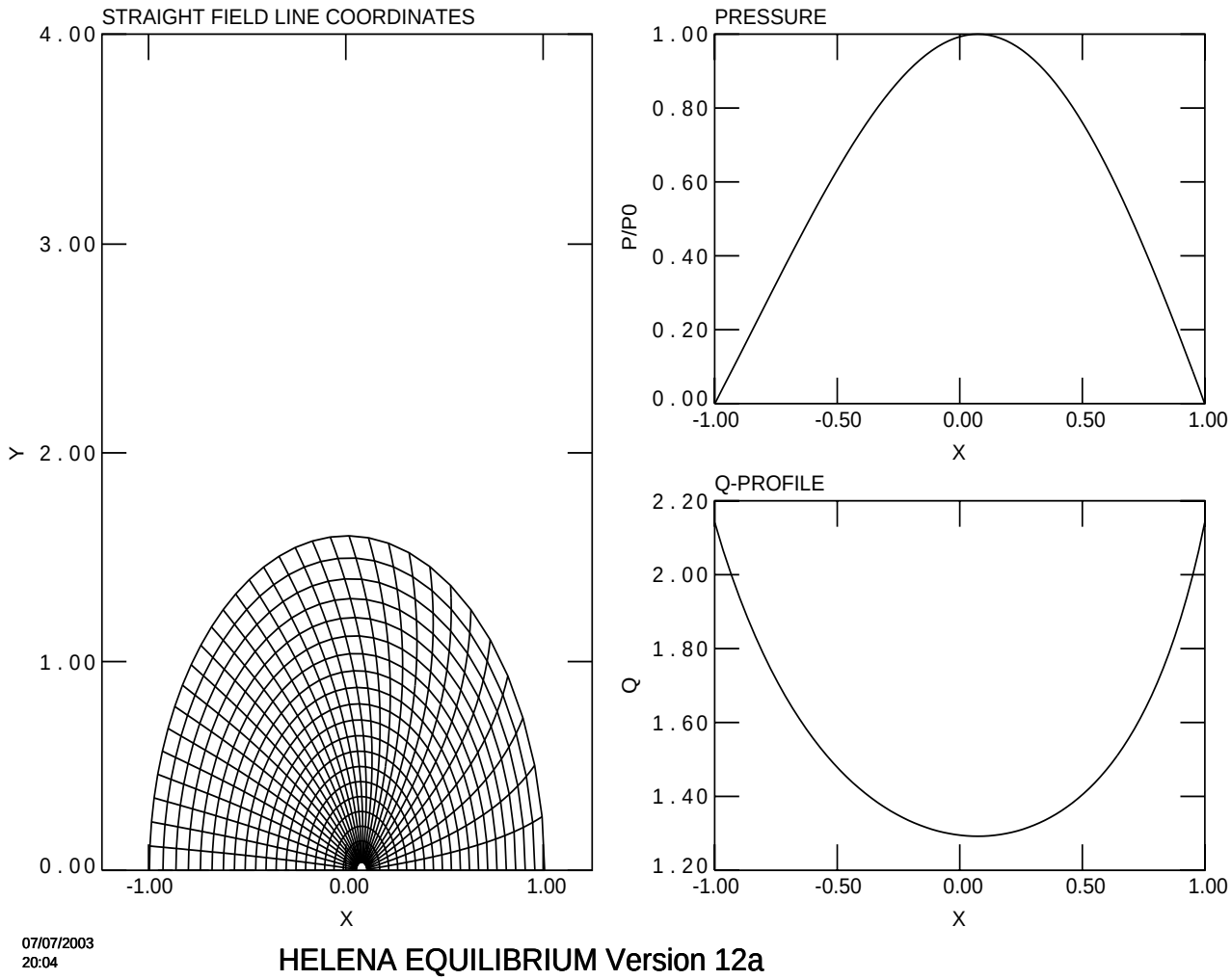

Figure 46: HELENA plot, equilibrium (II)

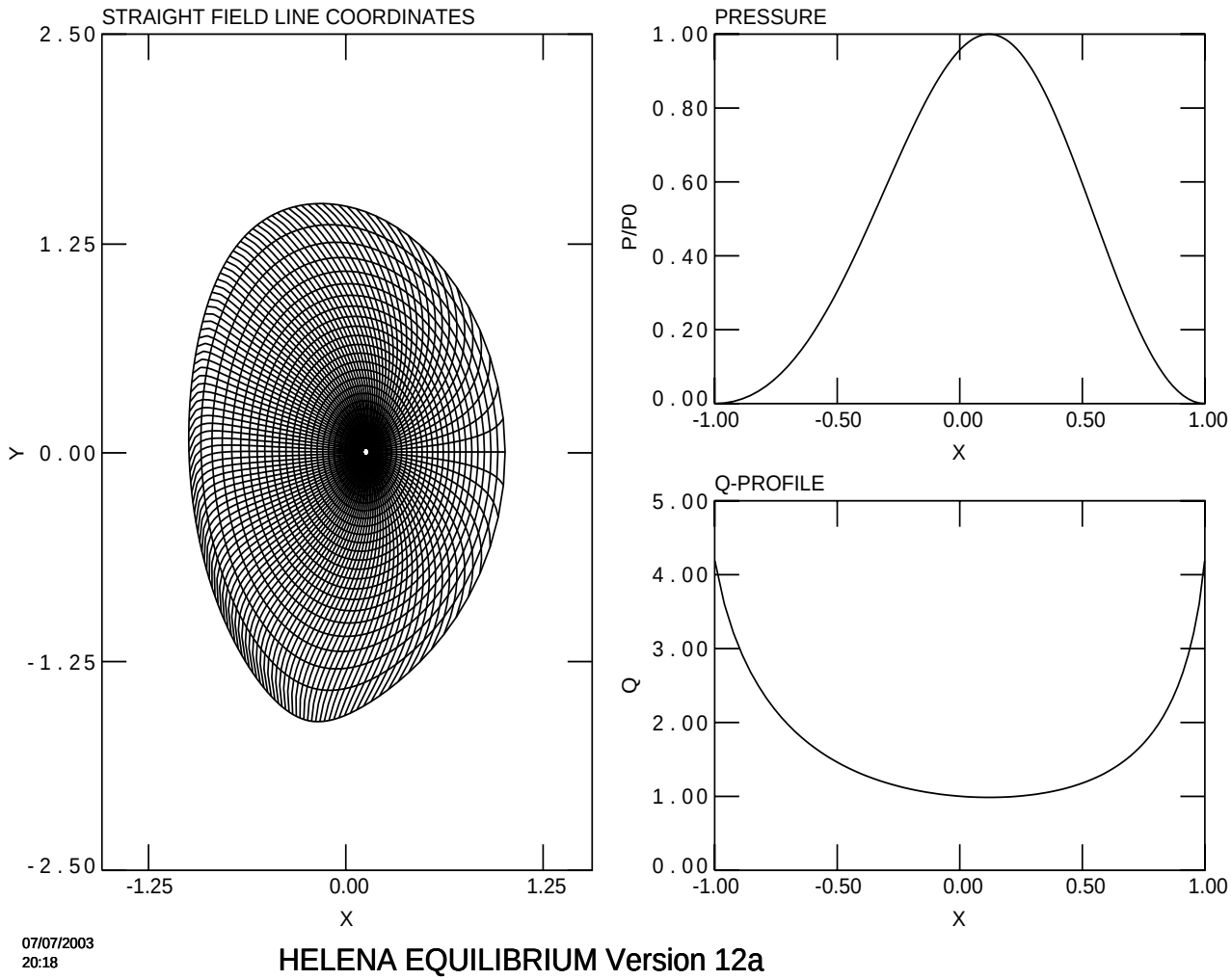

Figure 47: HELENA plot, equilibrium (III)

References

[1] H. Qin, PhD Thesis, Princeton University (1998)

[2] H. Qin,W.M. Tang, G.Rewoldt, Phys. Plasmas **5**, 1035 (1998)

[3] H. Qin,W.M. Tang, G.Rewoldt, Phys. Plasmas **6**, 2544 (1999)

[4] H. Qin,W.M. Tang, W.W.Lee, Phys. Plasmas **7**, 4433 (2000)

[5] H. Sugama, Phys. Plasmas **7**, 466 (2000)

[6] H. Sugama, W. Horton, Phys. Plasmas **5**, 2560 (1998)

[7] Landau, Lifschitz, Klassische Feldtheorie, Akademie-Verlag Berlin, p.49 (1967)

[8] R.G. Littlejohn, J. Plasma Physics **29**, 111 (1983)

[9] R.G. Littlejohn, Phys. Fluids **24**, 1730 (1981)

[10] J.R. Cary, R.G. Littlejohn, Annals of Physics **151**, 1 (1983)

[11] R.G. Littlejohn, J. Math. Phys. **23**, 742 (1982)

[12] J.D.Jackson, Classical Electrodynamics, 2nd Edition, sec.6.5

[13] T.G.Northrop, The Adiabatic Motion of Charged Particles, New York (1963)

[14] A. Brizard, J. Plasma Physics **41**, 541 (1989)

[15] A. Brizard, Phys. Plasmas **1**, 2480 (1994)

[16] A. Brizard, Phys. Plasmas **2**, 459 (1995)

[17] A. Brizard, Phys. Plasmas **7**, 4816 (2000)

[18] B.Coppi,G.Rewoldt, Advances in Plasma Physics, Vol.6, pp. 523 Wiley, NY (1976)

[19] T.S. Hahm, W.W.Lee, A. Brizard, Phys. Fluids **31**, 1940 (1988)

[20] B.Scott, The Gyrokinetic Equation, unpublished notes

[21] M.Brambilla: Kinetic Waves, Oxford (1999)

[22] M.Brambilla, unpublished notes

[23] M. Brambilla, Plasma Phys. Contr. Fus.**31**, 723 (1989)

[24] M. Brambilla, Plasma Phys. Contr. Fus.**41**, 1 (1999)

[25] M. Brambilla, Plasma Phys. Contr. Fus.**43**, 483 (2001)

[26] D.C. Montgomery, Theory of the Unmagnetized Plasma, New York (1957)

[27] P.H. Rutherford, E.A.Frieman, Phys. Fluids **11**, 569 (1968)

[28] T.M. Antonsen, Jr. and B. Lane, Phys. Fluids **23**, 1205 (1980)

[29] J.W. Connor, R.J Hastie, J.B. Taylor, Phys. Rev. Lett.**40**, 396 (1978)

[30] A. Kendl, Promotionsschrift, TU München, (2000)

[31] G. Arfken, Mathematical Methods for Physicists, p.580 Oxford (1985)

[32] E.A. Frieman, L. Chen, Phys. Fluids **25**, 502 (1982)

[33] R. Gruber, J. Rappaz: Finite Elemente Methods in Linear Ideal MHD, Springer Verlag (1985)

[34] J.P. Freidberg, Ideal Magnetohydrodynamics, New York (1982)

[35] G. Bateman: MHD Instabilities, MIT Press, Cambridge MA, (1978)

[36] J.D. Lawson, Proc. Roy. Soc. B **70**, 6 (1958)

[37] M.N. Rosenbluth et al., Phys. Fluids **16**, 1894 (1973)

[38] M. Bussac et al., Phys.Re. Letter **35**, 1638 (1975)

[39] J.D. Gaffey, J. Plasma Phys. **16**, 149 (1976)

[40] S. D. Pinches, Ph.D. Thesis, The University of Nottingham, (1996)

[41] S. D. Pinches et al., CPC **111**, 131 (1998)

[42] S.D. Pinches, private communication

[43] R. Marchand, PhD Thesis, Princeton University (1979)

[44] R. Marchand, W.M. Tang, G. Rewoldt, Phys Fluids **23**, 1164(1980)

[45] G.Y. Fu, J.W. VanDam, Phys Fluids B **1**, 2404 (1989)

[46] G.Strang, G.J. Fix, An Analysis of the Finite Element Method, Englewood Cliffs,N.J. (1973)

[47] H.R. Schwarz, Methode der finiten Elemente, Stuttgart (1984)

[48] G. Huijsmans, External Resistive Modes in Tokamaks, Utrecht (1991)

[49] J.B. Taylor, Bundle divertors and topology, Culham Report #CLM-R 132 (1974)

[50] A. Koenies, IAEA TCM Meeting, Goeteborg (2001)

[51] A. Koenies, private communication

[52] C. Nuehrenberg, Phys. Plasmas **6**, 137 (1998)
C. Nuehrenberg, Plasma Phys. Control. Fusion **41**, 1055 (1999)

[53] C.Z. Cheng, L. Chen, M.S. Chance, Annals of Physics **161**, 21 (1985)

[54] C.Z. Cheng, M.S. Chance, Phys. Fluids **29**, 11 (1986)

[55] C.Z. Cheng, M.S. Chance, J. Comp. Phys **71**, 124 (1987)

[56] D. Borba, W. Kerner, J. Comp. Phys **153**, 101 (1999)

[57] N.N. Gorelenkov, C.Z. Cheng, W.M. Tang, Phys. Plamas **5**, 3389 (1998)

[58] G. Rewoldt, W.M. Tang, and M.S. Chance, Phys. Fluids **25**, 480 (1982)
G. Rewoldt, W.M. Tang, and R.J. Hastie, Phys. Fluids **30**, 807 (1987)

[59] R.D. Hazeltine, J.D. Meiss, Plasma Confinement, Redwood City, (1992)

[60] F. Porcelli et al. Phys. Plasmas **1**, 470 (1994)

[61] S. Brunner , J. Vavlavik, Phys Fluids B **5**, 1605 (1993)

[62] I.M. Longman, MTAC **12**, 205 (1958)

[63] W.M. Tang, G.Rewoldt, Phys. Fluids B **5**, 2451 (1993)

[64] M.Artun, W.M. Tang, Phys. Fluids B **4**, 1102 (1992)

[65] M.Artun, W.M. Tang, Phys. Plasmas **1**, 2683 (1994)

[66] A. Jaun et al., CPC **92**, 153 (1995)

[67] K. McGuire et al. Phys. Rev. Lett **50**, 891 (1983)

[68] L. Chen, R.B. White, M.N. Rosenbluth, Phys. Rev. Lett **52**, 1122 (1984)

[69] S.M. Mahajan, Phys. Fluids **27**, 2238 (1983)

[70] Y. M. Li, S.M. Mahajan, D.W. Ross, Phys. Fluids **30**, 1466 (1985)

[71] R.R. Mett, S.M. Mahajan, Phys. Fluids B **4**, 2885 (1992)

[72] H.L. Berk, B.N. Breizman, H. Ye , Phys. Letters **162A**, 475 (1992)

[73] B.N. Breizman, S.E. Sharapov , Plasma Phys Control. Fusion **37**, 1057 (1996)

[74] A.Pochelon et. al., Proc. 28th EPS Conf. on Control. Fusion and Plasma Physics, ECA vol. 25 p. 5.009 (2001)

[75] A. Jaun et al., Nucl. Fusion **39**, 2095 (1999)

Acknowledgements

First I want to thank my direct supervisor Prof. Sibylle Günter in many respects: in choosing this challenging topic, she gave me not only the opportunity to get involved with many different theoretical models of plasma physics (which I enjoyed a lot) but also the possibility to address problems with high relevancy to today's and future experiments. On that way I appreciated the freedom she gave me to find my own preferences and priorities. I want to thank her for many physics discussions, proofreading all my texts, helping me to debug my code and motivating me in difficult situations. She also established contact to other scientists relevant for my work and gave me the great chance to visit PPPL in Princeton.

I want to thank Prof. Wilhelm for the academic supervision of my dissertation at the TU München and the time and interest he spent on my work.

I express my thanks to S.D. Pinches for introducing me to HAGIS, many useful and invaluable hints and tricks to solve my daily problems with physics and computers and for proofreading parts of my dissertation.

Many thanks to D. P. Coster for solving many of my numerous computer problems, explaining physical issues and proofreading parts of my dissertation.

'Thank you' to A. Könies for his interest and for valuable suggestions and remarks.

I also thank M. Brambilla , B. Scott and F. Jenko for introducing me into 'their' specific branch of plasma theory: their enthusiasm for physics and science was always a motivation for me.

Furthermore I want to thank C. Angioni, A.Bergmann, K. Borrass, Prof. M. Kaufmann, A. Kendl, R. Kleiber, Prof. K. Lackner, Y. Nishimura, A. Peeters and E. Strumberger and everybody else from the TOK group for their help and for valuable advice.

Last but not least I express my thanks to my host at PPPL Princeton, H. Qin, who introduced me into his work and thus gave me a profound basis for my dissertation. I also want to thank G. Rewoldt, W. Tang, S. Brunner, W.W. Lee, J. Lewandowski and T.S. Hahm for useful discussions.